Stony Brook University

Defect Characterization in 4H Silicon Carbide Bulk Crystals and Epilayers

A Dissertation Presented

by

Fangzhen Wu

to

The Graduate School

in Partial Fulfillment of the

Requirements

for the Degree of

Doctor of Philosophy

in

Materials Science and Engineering

Stony Brook University

December 2014

Stony Brook University

The Graduate School

Fangzhen Wu

We, the dissertation committee for the above candidate for the

Doctor of Philosophy degree, hereby recommend

acceptance of this dissertation.

Michael Dudley – Dissertation Advisor
Professor, Department of Materials Science and Engineering

Balaji Raghothamachar - Chairperson of Defense
Research Assistant Professor, Department of Materials Science and Engineering

T. A. Venkatesh
Associate Professor, Department of Materials Science and Engineering

Dong Su
Ph.D., Staff Scientist, Center for Functional Nanomaterials
Brookhaven National Laboratory

This dissertation is accepted by the Graduate School

Charles Taber
Dean of the Graduate School

Abstract of the Dissertation

Defects Characterization in 4H Silicon Carbide Bulk Crystals and Epilayers

by

Fangzhen Wu

Doctor of Philosophy

in

Materials Science and Engineering

Stony Brook University

2014

4H silicon carbide (4H-SiC) has been accepted as an optimal semiconductor that can substitute for silicon for fabricating advanced power devices for high temperature, high power, and high frequency applications, owing to its outstanding properties such as wide bandgap, high breakdown electric field, high saturation drift velocity and high thermal conductivity. Developments in advanced growth techniques for both 4H-SiC bulk crystals and epilayers have led to an era of large wafer sizes and relatively low defect densities, and these achievements are partly attributed to extensive and careful studies of different kinds of defects in this material. In turn, high crystal quality provides a unique opportunity to better understand defects behavior and also discover any new types of defects.

The central focus of this dissertation is to study the nature of various defects in 4H-SiC, determine their origins, and explain their formation mechanisms and the goal is to enlighten potential strategies to eventually eliminate these defects. Synchrotron x-ray topography, high

resolution transmission electron microscopy, chemical etching and computer simulations have been intensively used in the studies.

The outcomes can be divided into four parts: (I) Threading c+a dislocations have been recognized from those traditionally considered as threading screw dislocations, and their nucleation, propagation and mutual interactions have been studied; (II)The defect evolution process from threading dislocations with c-component of Burgers vector to stacking faults has been studied. Deflection of threading c+a dislocations was observed to be able to create stacking faults comprising mixtures of Shockley component and Frank component. Moreover, open-core threading screw dislocations, or micropipes, were found to be the source of stacking faults with a peculiar configuration of six-pointed star shape; (III) 2D nucleation mechanisms were provided to explain the formation of stacking faults with 6H structure in the substrate and the formation of so-called V-shaped defects in the epilayer; (IV) A new method has been developed to determine the faults vectors associated with stacking faults in 4H-SiC from their stacking sequences and meanwhile to provide possible pathways to transform the perfect stacking sequence to the faulted one. This technique is also expected to be applicable to all structures comprising corner shared tetrahedra, such as 2H, 3C, 6H, and 15R.

to my fianc é

Ting Chen

Table of Contents

List of Figures

List of Tables

List of Abbreviations

PVT	Physical vapor transport
CVD	Chemical vapor deposition
TSD	Threading screw dislocation
TED	Threading edge dislocation
TMD	Threading mixed dislocation
BPD	Basal plan dislocation
SF	Stacking fault
DSF	Double Shockley fault
TEM	Transmission electron microscopy
HRTEM	High resolution transmission electron microscopy
SWBXT	Synchrotron white beam x-ray topography
SMBXT	Synchrotron monochromatic beam x-ray topography
SEM	Scanning electron microscopy
AFM	Atomic force microscopy

Acknowledgments

I would like to express my sincere respect and gratitude to my academic advisor Prof. Michael Dudley, who provided me with this exciting opportunity to work in the field of crystal growth and characterization. His broad knowledge and creativity always inspires me during my academic life at Stony Brook University. I am deeply grateful to him for believing in my potential and abilities and also for his patience and guidance in all the studies of this dissertation.

I would like to thank Prof. Balaji Raghothamachar, Prof. T. A. Venkatesh, and Dr. Dong Su for consenting to be on my defense committee and providing valuable suggestions. Besides, they also supported my work in many other different ways. Prof. Balaji Raghothamachar was always available to assist me in x-ray topography experiments and provide me with helpful suggestions. Prof. T. A. Venkatesh introduced me to the field of stress analysis and held several related discussions with me. Dr. Dong Su taught me a great amount of knowledge about TEM and shared lots of practical skills with me.

I am grateful to all my peers in Prof. Michael Dudley's group, Dr. Yu Zhang, Dr. Shayan Byrappa, Dr. Vishwanath Sarkar, Dr. Huanhuan Wang, Yu Yang, Jianqiu Guo, Ouloide Y. Goue, Tianyi Zhou, Shun Sun, Hao Wang, Zheyu Li, Zihao Ding, Ruifen Chen, Mengnan Zhou, Xuejing Wang, and Fei Wang, for their help in both my research and personal life. Special thanks to Dr. Huanhuan Wang for our close collaboration and effective communication.

Last but not least, I am indebted to my loving parents, Xiguan Wu and Xiufeng Chen, for their unconditional love and support throughout my education.

The research in Chapters 3-7 and 9-12 was supported by Dow Corning and the research in Chapter 8 was supported by II-VI Incorporated. Topography experiments were carried out at the Stony Brook Synchrotron Topography Facility, Beamline X-19C, at the National Synchrotron Light Source, Brookhaven National Laboratory (DOE Office of Basic Energy Sciences Contract no. DE-AC02-98CH10886) and Beamline 1-BM at the Advanced Photon Source, Argonne National Laboratory. HRTEM studies were carried out at the Center for Functional Nanomaterials, Brookhaven National Laboratory (DOE Office of Basic Energy Sciences Contract no. DE-AC02-98CH10886).

Publications

1. F. Wu, H. Wang, Y. Yang, J. Guo, B. Raghothamachar, M. Dudley, S. G. Mueller, G. Chung, E. K. Sanchez, D. Hansen, M. J. Loboda, L. Zhang, D. Su, K. Kisslinger, and E. Stach, "Stacking fault formation via 2D nucleation in PVT grown 4H-SiC", Mater. Sci. Forum (in press)

2. F. Wu, H. Wang, B. Raghothamachar, M. Dudley, G. Chung, J. Zhang, B. Thomas, E. K. Sanchez, S. G. Mueller, D. Hansen, M. J. Loboda, L. Zhang, D. Su, K. Kisslinger, and E. Stach, "Characterization of V Shaped Defects in 4H-SiC Homoepitaxial Layers", J. Electron. Mater. (in press)

3. F. Wu, H. Wang, B. Raghothamachar, M. Dudley, S.G. Mueller, G. Chung, E.K. Sanchez, D. Hansen, M.J. Loboda, L. Zhang, D. Su, K. Kisslinger and E. Stach, "A Method to Determine Fault Vectors in 4H-SiC from Stacking Sequences Observed on High Resolution Transmission Electron Microscopy Images", Journal of Applied Physics, vol. 116, 104905 (2014)

4. H. Wang, F. Wu, M. Dudley, B. Raghothamachar, G. Chung, J. Zhang, B. Thomas, E.K. Sanchez, S.G. Mueller, D. Hansen, and M.J. Loboda, "Measurement of Critical Thickness for the Formation of Interfacial Dislocations and Half Loop Arrays in 4H-SiC Epilayer via X-Ray Topography", Materials Science Forum, vols. 778-780, pp. 328-331, (2014)

5. H. Wang, F. Wu, S. Byrapa, Y. Yang, B. Raghothamachar, M. Dudley, G. Chung, J. Zhang, B. Thomas, E.K. Sanchez, S.G. Mueller, D.M. Hansen, M.J. Loboda, "Study of V and Y shape Frank-type Stacking Faults Formation in 4H-SiC epilayer", Materials Science Forum, vol. 778, pp. 332-337 (2014)

6. T. Zhou, B. Raghothamachar, F. Wu, R. Dalmau, B. Moody, S. Craft, R. Schlesser, M. Dudley, Z. Sitar, "Characterization of Threading Dislocations in PVT-Grown AlN Substrates via x-Ray Topography and Ray Tracing Simulation", Journal of Electronic Materials, vol. 43, pp. 838-842 (2014)

7. H. Wang, F. Wu, S. Byrappa, B. Raghothamachar, M. Dudley, P. Wu, I. Zwieback, A. Souzis, G. Ruland, and T. Anderson, "Synchrotron Topography Studies of the Operation of Double-Ended Frank-Read Partial Dislocation Sources in 4H-SiC", Journal of Crystal Growth, vol. 401, pp. 423–430 (2014)

8. F. Wu, H. Wang, B. Raghothamachar, M. Dudley, S.G. Mueller, G. Chung, E.K. Sanchez, D. Hansen and M.J. Loboda, "Direct Observation of Stacking Fault Nucleation from Deflected Threading Dislocations with Burgers Vector c+a in PVT Grown 4H-SiC", MRS Proceedings, 1693, mrss14-1693-dd01-04 (2014)

9. J. Zhang, D.M. Hansen, V.M. Torres, B. Thomas, G. Chung, H. Makoto, I. Manning, J. Quast, C. Whiteley, E.K. Sanchez, S. Mueller, M.J. Loboda, H. Wang, F. Wu, M. Dudley, "Defect Reduction Paths in SiC Epitaxy", MRS Proceedings, vol. 1693, mrss14-1693-dd01-05 (2014)

10. M. Dudley, B. Raghothamachar, H. Wang, F. Wu, S. Byrappa, G. Chung, E.K. Sanchez, S. Mueller, D. Hansen, M. Loboda, "Synchrotron X-Ray Topography Studies of the Evolution of the Defect Microstructure in Physical Vapor Transport Grown 4H-SiC Single Crystals", ECS Transactions, vol. 58, pp. 315-324 (2013)

11. F. Wu, H. Wang, S. Byrappa, B. Raghothamachar, M. Dudley, P. Wu, X. Xu, I. Zwieback, "Characterization and Formation Mechanism of Six-pointed Star type Stacking Faults in 4H-SiC", Journal of Electronic Materials, vol. 42, Issue 5, pp 787-793 (2013)

12. H. Wang, S. Sun, M. Dudley, S. Byrappa, F. Wu, B. Raghothamachar, G. Chung, E.K Sanchez, S.G Mueller, D. Hansen, M.J. Loboda, "Quantitative Comparison Between Dislocation Densities in Offcut 4H-SiC Wafers Measured Using Synchrotron X-ray Topography and Molten KOH Etching", Journal of Electronic Materials, vol. 42, pp.794-798 (2013)

13. F. Wu, M. Dudley, H. Wang, S. Byrappa, S. Sun, B. Raghothamachar, E.K. Sanchez, G. Chung, D. Hansen, S.G. Mueller, M.J. Loboda, "The Nucleation and Propagation of Threading Dislocations with C-Component of Burgers Vector in PVT-Grown 4H-SiC", Materials Science Forum, vols. 740-742, pp. 217-220, (2013)

14. T. Zhou, B. Raghothamachar, F. Wu, M. Dudley, "Grazing Incidence X-ray Topographic Studies of Threading Dislocations in Hydrothermal Grown ZnO Single Crystal Substrates", MRS Proceedings, vol. 1494, pp.121-126 (2013)

15. Müller St.G., Sanchez E.K., Hansen D.M., Drachev R.D., Chung G., Thomas B., Zhang J., Loboda M.J., Dudley M., Wang H., Wu F., Byrappa S., Raghothamachar B., and Choi G., "Volume production of high quality SiC substrates and epitaxial layers: Defect trends and device applications", Journal of Crystal Growth, 352, 39-42, (2012)

16. Wu F., Wang H., Byrappa S., Raghothamachar B., Dudley M., Sanchez E.K., Hansen D., Drachev R., Mueller S.G. and Loboda M.J., "Synchrotron X-ray Topography Studies of the Propagation and Post-Growth Mutual Interaction of Threading Growth Dislocations with c-component of Burgers Vector in PVT-Grown 4H-SiC", Materials Science Forum, 717-720, 343-346, (2012)

17. Byrappa S., Wu F., Wang H., Raghothamachar B., Choi G., Sun S., Dudley M., Sanchez E. K., Hansen D., Drachev R., Mueller S.G. and Loboda M.J., "Deflection of Threading Dislocations with Burgers vector c/c+a observed in 4H-SiC PVT –Grown Substrates with Associated Stacking faults", Materials Science Forum, 717-720, 347-350, (2012)

18. Wang H., Byrappa S., Wu F., Raghothamachar B., Dudley M., Sanchez E.K., Hansen D., Drachev R., Mueller S.G. and Loboda M.J., "Basal Plane Dislocation Multiplication via the Hopping Frank-Read Source Mechanism and Observations of Prismatic Glide in 4H-SiC", Materials Science Forum, 717-720, 327-330, (2012)

19. Wang H., Wu F., Byrappa S., Sun S., Raghothamachar B., Dudley M., Sanchez E.K., Hansen D., Drachev R., Mueller S.G., and Loboda M.J., "Basal Plane Dislocation

Multiplication via the Hopping Frank-Read Source Mechanism in 4H-SiC", Applied Physics Letters, 100, 172105 (2012)

20. Wu F., Byrappa S., Wang H., Chen Y., Raghothamachar B., Dudley M., Sanchez E.K., Chung G., Hansen D., Mueller S.G. and Loboda M.J., "Simulation of Grazing-Incidence Synchrotron X-ray Topographic Images of Threading c+a Dislocations in 4H-SiC", MRS Proceedings**, Vol.** 1433, mrss12-1433-h03-06 (2012)

21. Wang H., Wu F., Byrappa S., Shun S., Raghothamachar B., Dudley M., Sanchez E.K., Chung G., Hansen D., Mueller S.G. and Loboda M.J., "Combined Application of Section and Projection Topography to Defect Analysis in PVT-Grown 4H-SiC", MRS Proceedings, Vol. 1433, mrss12-1433-h02-04 (2012)

22. Dudley M., Wang H., Wu F., Byrappa S., Shun S., Raghothamachar B., Sanchez E.K., Chung G., Hansen D., Mueller S.G. and Loboda M.J., "Synchrotron Topography Studies of Growth and Deformation-Induced Dislocations in 4H-SiC", MRS Proceedings, Vol. 1433, mrss12-1433-h03-03 (2012)

23. Dudley M., Wu F., Wang H., Byrappa S., Raghothamachar B., Choi G., Sun S., Sanchez E.K., Hansen D., Drachev R., Mueller S.G., and Loboda M.J., "Stacking Faults Created by the Combined Deflection of Threading Dislocations of Burgers Vector c and c+a During the Physical Vapor Transport Growth of 4H–SiC", Applied Physics Letters, 98, 232110 (2011)

24. Dudley M., Wang H., Wu F., , Byrappa S., Raghothamachar B., Choi G., Sanchez E.K., Hansen D., Drachev R., Mueller S.G., and Loboda M.J., "Formation Mechanism of Stacking Faults in PVT 4H-SiC Created by Deflection of Threading Dislocations with Burgers Vector c+a", Materials Science Forum, 679-680, 269-272, (2011)

25. Dudley M., Byrappa S., Wang H., Wu F., Zhang Y., Raghothamachar B., Choi G., Sanchez E., Hansen D., Drachev R., Loboda M., "Analysis of Dislocation Behavior in Low Dislocation Density, PVT-Grown, Four-Inch Silicon Carbide Single Crystals", MRS Proceedings, vol. 1246, 1246-B02-02 (2010)

1. Introduction of SiC as a Semiconductor Material

1.1 Crystal Structure

Silicon carbide (SiC) is a compound semiconductor composed of 50% silicon (Si) and 50% carbon (C). Both elements Si and C are from group 14 (old group IV) in the periodic table and have four valence electrons in the outermost electron shell. Si and C atoms are bonded with covalent bonds and each atom is attached to four such bonds, forming corner shared tetrahedra as shown in Figure 1.1. SiC is famous for polytypism, where its various close-packed crystal structures differ in one dimension only. In the hexagonal crystal system, these structures are identically close-packed in (0001) plane (also known as basal plane) but different in stacking sequence in [0001] direction (also known as c-axis direction). There are three possible stacking positions as illustrated in Figure 1.2. Atoms on the first layer are closed packed and the occupied position is denoted as A, and atoms on the next layer on top can occupy either position B or C to form stable tetrahedral structures. In the similar way, layers of atoms can be stacked up along c-axis direction at the stacking positions which must be different from that of the layer right below. According to the differences in stacking sequence within the height of one unit cell, polytypes are distinguished. SiC has been found to have more than 200 polytypes.

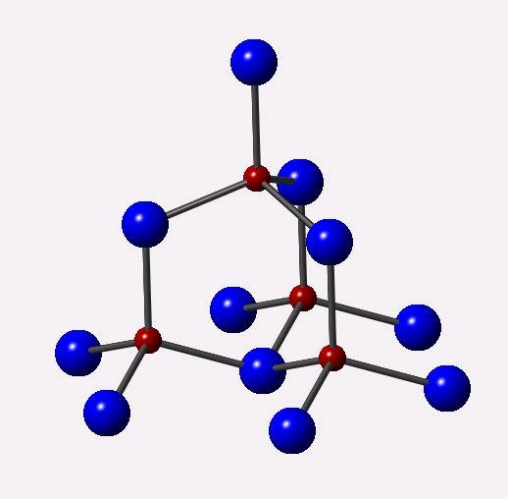

Figure 1.1 Ball and stick model of the structure comprising corner shared SiC tetrahedra. Blue balls represent Si atoms and red balls represent C atoms

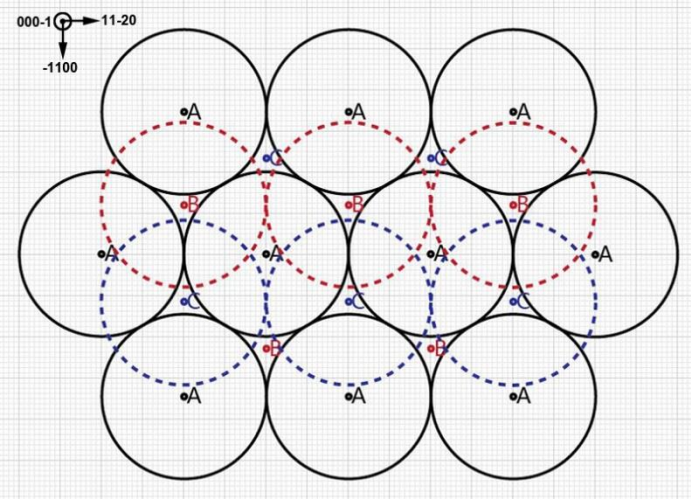

Figure 1.2 Three possible stacking positions in close packed structures, labeled as A, B and C respectively. On top of A layer, the atoms can take the stacking positions of either B or C

In Ramsdell's notation, polytypes can be designated by specifying the total number of layers in the hexagonal unit cell followed by the letter C, H, or R to indicate an over-all lattice type as being cubic, hexagonal, or rhombohedral respectively. The structures of three popular SiC polytypes, e.g. 3C, 4H, and 6H, are schematically shown in Figure 1.3 and have repeating stacking sequence of ABC, ABA'C', and ABCB'A'C' respectively, where a prime sign denotes a twinned tetrahedron. The difference between a twinned tetrahedron and an untwinned (regular) tetrahedron can be easily noticed after projecting them onto {11-20} plane, and their triangular projections are mirror images of one another, as illustrated in Figure 1.3. In Zhdanov's notation, the structures comprising corner-shared tetrahedra can be designated by a code composed of the

numbers of the continuous same type tetrahedra along c-axis direction within the height of a unit cell. For example, 3C, 4H, 6H and 15R structures can also be designated as ∞, (22), (33) and $(32)_3$ respectively. The lattice parameters of these structures in hexagonal crystal system are summarized in Table 1. It can be discovered that the lattice parameter *a* is about the same and *c* is proportional to the numbers of layers in the hexagonal unit cell.

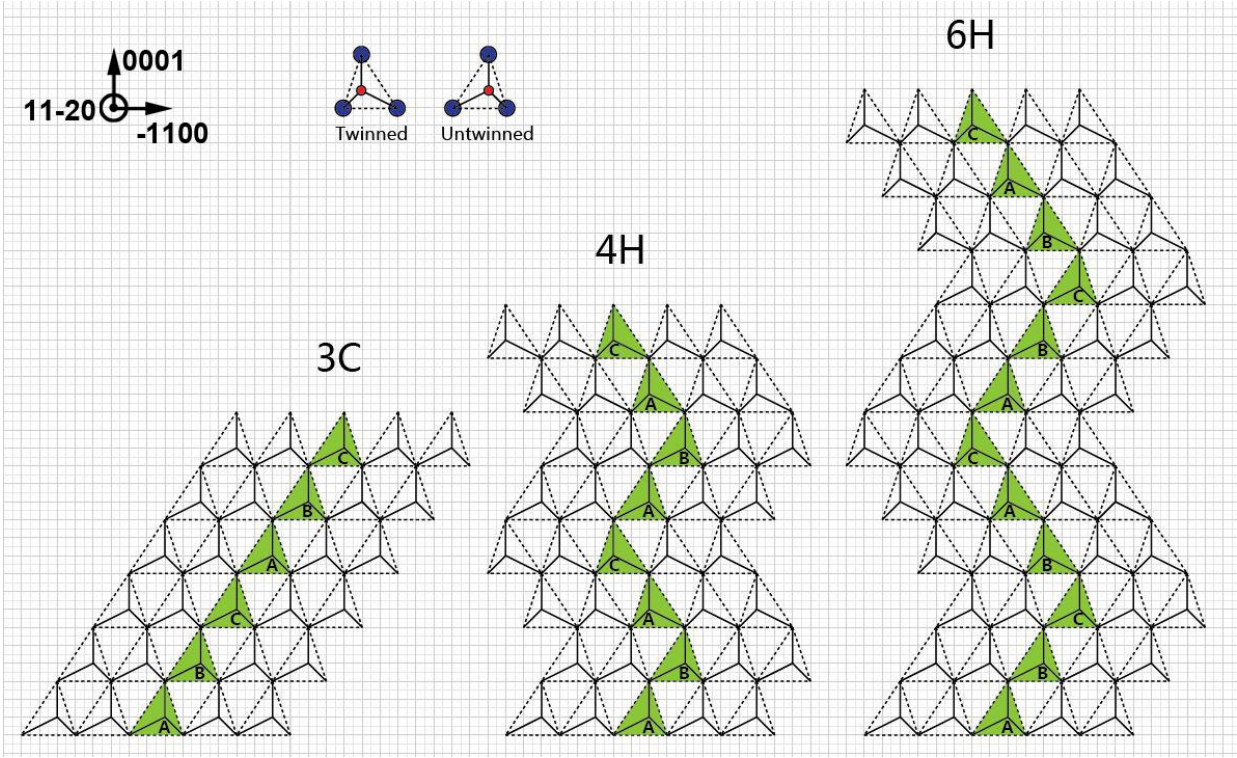

Figure 1.3. Stacking sequences of SiC polytypes in stick (bond only) model

Table 1 Lattice parameters of SiC polytypes in hexagonal crystal system

	3C	4H	6H	15R
a (Å)	3.07	3.08	3.08	3.07
c (Å)	7.57	10.05	15.12	37.70

1.2 Physical Merits

The bandgap (E_g) of 3C-, 4H-, and 6H-SiC is measured to be 2.36ev, 3.26ev, and 3.02ev respectively at room temperature [1], compared to 1.12ev for Si and 1.43ev for GaAs [2] as conventional semiconductors, and hence SiC materials are recognized as wide-bandgap semiconductors. Without external cooling, Si-based electronics fail at temperatures above 200 ℃ due to increasing leakage current of pn junctions or Schottky barrier at reverse bias as a function of temperature. The leakage current is caused by the flow of intrinsic carriers in semiconductor, which are electron and hole pairs generated when electrons are excited from valence band to conduction band. Wider bandgap leads to higher energy that is required to excite a free electron, and thus intrinsic carrier concentration in a wide bandgap semiconductor is less sensitive to heat.

SiC-based electronics are capable of functioning at a much higher temperature, beyond 600℃ [3], according to this fundamental theory.

Wide bandgap is also associated with another important property – high breakdown electric field (E_b). This value for SiC polytypes can be 1.8MV/cm for 3C, 3.5MV/cm for 4H, and 3.8MV/cm for 6H [2], compared to 0.3MV/cm for Si and 0.4MV/cm for GaAs [2]. Breakdown of power devices can be attributed to impact ionization at the junction when a critical electrical field is applied at reverse bias. At the point of breakdown, charge carriers (free electrons and electron holes) are accelerated by the electrical field to have enough kinetic energy to knock a bound electron out from the valence band to the conduction band and create electron-hole pairs, resulting in leakage current multiplication. The wide bandgap of SiC polytypes thus require much higher electric field to excite carriers for impact ionization.

For high frequency application, high carrier mobility and high saturated drift velocity are desirable for a semiconductor material. Carrier mobilities in SiC materials are quite different between different polytypes and also between different doping types. Hole mobilities (μ_h) of p-type doping SiC materials are low and on the order of 20-120 $cm^2v^{-1}s^{-1}$ [4], which impedes their application in high frequency devices. Electron mobilities (μ_e) of n-type doping SiC materials are listed and compared to those of GaAs and Si in Table 2. The value for 6H-SiC is relatively low compared to the other materials and 6H-SiC exhibit strong anisotropy ($\mu_\perp/\mu_\parallel=5$) in this value, which is one of the reasons that 6H-SiC attracts less attention in device fabrication. Although the values for electron mobilities of SiC materials are much smaller than the value for GaAs (which is preferable to Si for high frequency application), the maximum velocities, known as saturation drift velocities (v_{sat}), that electrons in SiC materials can reach at high electric field are higher than in GaAs, as listed in Table 2.

Table 2 Comparison of electron mobility and saturation electron drift velocity of SiC polytypes, GaAS, and Si

	3C-SiC ($N_d=10^{16}cm^{-3}$)	4H-SiC ($N_d=10^{17}cm^{-3}$)	6H-SiC ($N_d=10^{18}cm^{-3}$)	GaAs	Si
Electron Mobility ($cm^2v^{-1}s^{-1}$)	890 [5]	perpendicular to c-axis 947 [4]	perpendicular to c-axis 415 [4]	5000 [2]	1400 [6]
		along c-axis 1141 [4]	along c-axis 83 [4]		
Saturation Electron Drift Velocity (10^7cms^{-1})	2.5 [7]	2.2 [1]	1.9 [1]	1.2 [8]	1 [8]

Single crystalline SiC materials have high thermal conductivity (K), which make them even more suitable for fabrication of power devices. High thermal conductivity prevents semiconductors from degradation at elevated temperature due to accumulation of dissipated power and enables integration of devices at high packing densities. The values for thermal conductivities of 3C-, 4H-, and 6H-SiC at room temperature are 3.6 W $cm^{-1}K^{-1}$, 3.7 W $cm^{-1}K^{-1}$, and 4.9 W $cm^{-1}K^{-1}$ respectively [9], compared to a decent value of 1.5 W $cm^{-1}K^{-1}$ for Si [10] and a low value of 0.55 $cm^{-1}K^{-1}$ [11] for GaAs.

1.3 Defects and Problems

Currently, the development of SiC power devices, especially 4H-SiC based, are ahead of other also promising wide-bandgap semiconductors, such as gallium nitride (GaN) and diamond, due to the availability of high-quality large-size SiC substrates and epitaxial wafers. Although the superiority of SiC as a wide-bandgap semiconductor had been long acknowledged back to 1950's [12], the early development of SiC electronics was unsteady and the "material problem", which referred to difficulties in growth of single crystal and high defect densities, seemed to be extremely difficult to overcome. SiC bulk materials are usually grown with sublimation (physical vapor transport (PVT)) method. Breakthrough was made in 1981 when the seeded sublimation method (also known as the modified Lely method) [13] was introduced, and since then improvements in this technique led to one after another records for both wafer size and crystal quality [14, 15]. Extensive studies on epitaxial growth of SiC started in the 1980's. Chemical vapor deposition (CVD) has been used to grow 3C-SiC on Si substrates [16], and 4H- and 6H-SiC epilayers are homoepitaxially grown with a special designed CVD technique, called step-controlled epitaxy, which features the usage of substrates with a small off-cut angle [17, 18]. Among different SiC polytypes, 4H-SiC is more popular than the others in power device fabrication because of its high electron mobility. On the other hand, 6H-SiC shows strong anisotropy in its electrical properties, which are not preferable for power device fabrication; heteroepitaxial growth of 3C-SiC on Si needs to deal with various problems, such as high density of stacking faults, caused by large mismatch between epilayer and substrate in lattice parameters and thermal expansion coefficients.

Large size 4H-SiC substrate and epitaxial wafers, up to 150 mm in diameter [19], are commercially available at present and decrease in defect densities allow various 4H-SiC based devices [1] being built and tested. However, it is found that defects in the active layers of devices can affect device performance and reliability. The crystallographic defects in 4H-SiC bulk crystals and epilayers that have been reported in literatures are summarized in Table 3.

Table 3 Crystallographic defects in 4H-SiC bulk crystals and homoepitaxial layers

		Location	Nature	Typical density at present	Impact
Growth Dislocation	Micropipe	Substrate; replicating into epi	Burger vector > 3×<0001>	<0.1cm^{-2}	>50% breakdown voltage (V_b) reduction for pn diodes [20]
	Threading screw dislocation (TSD)	Substrate; replicating into epi	Burger vector = <0001>	10^2-10^3cm^{-2}	5-35% breakdown voltage (V_b) reduction pn diodes [21]
	Threading edge dislocation (TED)	Substrate; replicating into epi	Burger vector = 1/3<11-20>	10^3-10^4cm^{-2} in the substrate	no significant damage
Basal plane dislocation (BPD)		Substrate; <2% replicating into eip, and >98% converted into TEDs in epi	Burger vector = 1/3<11-20>	10^3-10^4cm^{-2} in the substrate	degradation of bipolar device (through nucleating Shockley faults) [22]
Interfacial dislocation and half loop array		Epi	Burger vector = 1/3<11-20>	/	same as BPD
Stacking fault	Shockley fault	Substrate; Epi	(31) stacking sequence	/	increase in the forward voltage drop (V_f) for bipolar devices [22]
	Double Shockley fault	Substrate; Epi	(60) stacking sequence	/	resistivity increase for unipolar devices [23]; plastic deformation in device fabrication [24, 25]
	8H fault	Epi	(44) stacking sequence	/	~20% breakdown voltage (V_b) reduction for Schottky barrier diodes [26]
	Intrinsic Frank fault	Epi	(50) stacking sequence	/	/
	Carrot defect	Epi	a basal fault having (30) stacking sequence plus a prismatic fault	<0.1cm^{-2}	two orders increase in reverse leakage current for for Schottky barrier diodes [27]
3C triangular defect		Epi	3C polytype inclusion	<0.1cm^{-2}	>65% breakdown voltage (V_b) reduction for pn diodes [28]

1.3.1 Micropipe

Micropipes are hollow tubes running approximately along the c-axis direction, which is usually the crystal growth direction, throughout the entire boule. The diameter of the hollow cores can be measured by scanning electron microscopy (SEM) [29] or atomic force microscopy (AFM) [30] and ranges from 0.1-10 um. Because of the large scale in their size, micropipes can be seen even using optical microscopy [31]. At the as-grown surface of a boule, micropipes can be found at the positions of the axes of growth spirals, which are usually associated with the emergent ends of screw dislocations. Therefore, micropipes are often considered to be hollow-core super screw dislocations. Synchrotron x-ray topography studies, in Dudley's group, of the strain field associated with micropipes confirmed their nature as screw dislocations [32] and their Burgers vectors were determined to be multiple ***c***. The minimum magnitude for a micropipe is 3c for 4H-SiC and 2c for 6H-SiC [33]. The characteristics of micropipe being open-core can be explained with the theory proposed by Frank [34] involving an status of energy equilibrium between releasing the strain energy associated with a dislocation with large Burgers vector by breaking bonds to form an empty tube and increasing the surface energy as area of the free surface increases. Frank also proposed that the radius of the empty tube is proportional to the square of the Burgers vector. Dudley et al. demonstrated that micropipes can be nucleated during the process of incorporation of inclusions into the growing crystal [35].

1.3.2 Threading screw dislocation

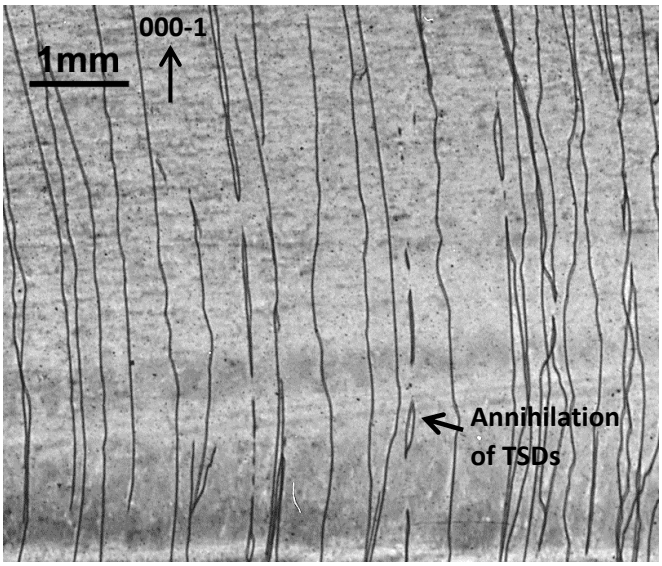

Figure 1.4 SWBXT transmission image of (0004) reflection showing TSDs propagating along c-axis

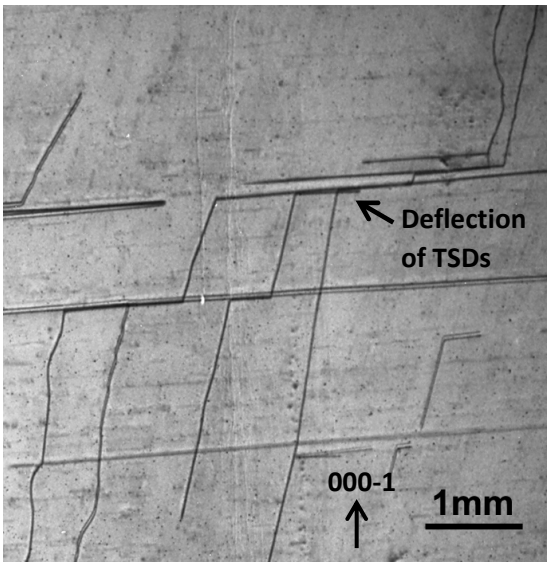

Figure 1.5 SWBXT transmission image of (0004) reflection showing deflection of TSDs onto the basal plane

Threading screw dislocations (TSDs) are screw type dislocations with Burgers vector of one ***c*** running approximately along c-axis. TSDs, as well as micropipes, are growth dislocations, which means they are connected to the growth front and propagate as the growth front advances. It is generally considered that TSDs cannot glide because of the large magnitude of their Burgers vector ($|\boldsymbol{c}|$ is about three times as big as $|\boldsymbol{a}|$ in 4H-SiC). Therefore, TSDs are usually long and straight in the boule, as shown in Figure 1.4. Annihilation could happen if two opposite-sign

TSDs get close to each when they interact with vacancies and climb behind the growth front [36]. During the growth, TSDs sometimes can be deflected onto the basal plane, as shown in Figure 1.5, by overgrowth of macrosteps, and these deflected dislocations may have chance to be redirected back to the threading orientation in response to any large step coming from the opposite direction. Annihilation and deflection of TSDs can contribute to the decrease in their density as the crystal grows thicker. Recent synchrotron x-ray topography studies reveals that many dislocations that are traditionally considered as threading screw dislocations actually have a mixed Burgers vector of one ***c*** plus one ***a***. The nucleation, propagation and mutual interactions of these threading c+a dislocations will be discussed in Chapter 3 and 4.

1.3.3 Threading edge dislocation

Threading edge dislocations (TEDs) are edge type dislocations with Burgers vector of one ***a*** running approximately along c-axis. TEDs are also growth dislocations; differing from TSDs, TEDs are able to glide behind the growth front under thermal stress, which are induced by inhomogeneous thermal expansion due to temperature gradient [37] in a growing crystal. The slip systems for TEDs are {1-100}<11-20> and the slip planes {1-100} are called prismatic planes. Glide of TEDs on prismatic planes can generate segments of screw types BPDs in the wake of glide, as shown in Figure 1.6. During the growth, TED lines could slightly deviate from the c-axis direction and pass through multiple prismatic planes, because the growth front is usually either convex or concave. The TED segments lying right in the prismatic planes get pinned by the remaining parts of the dislocations and only these TED segments on the prismatic planes can glide under certain stress.

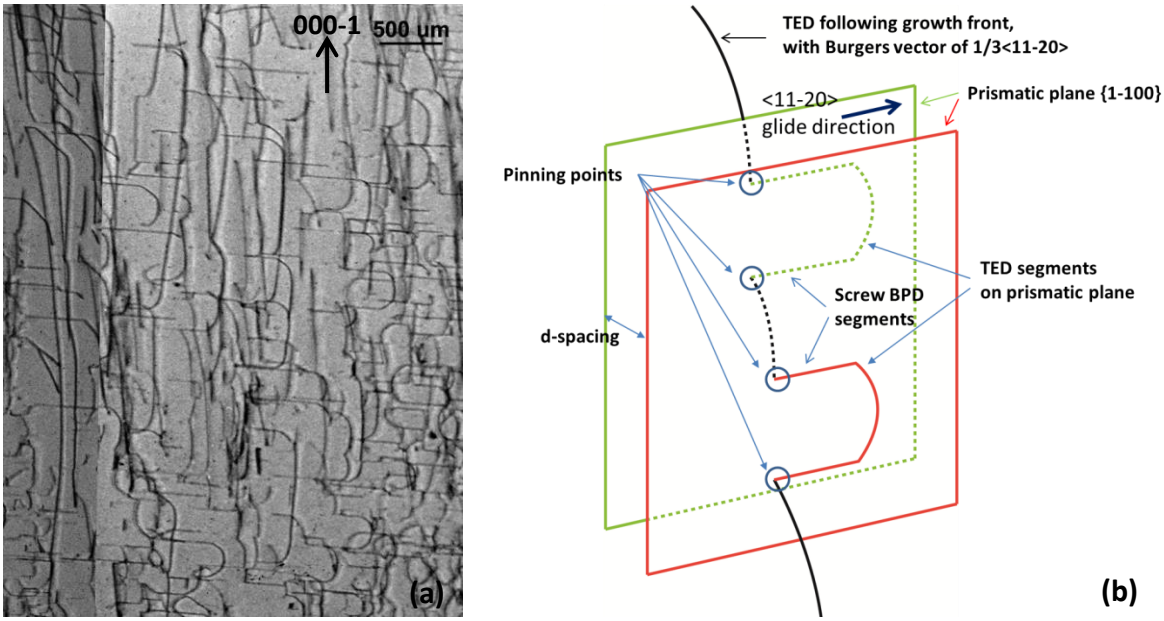

Figure 1.6 (a) SWBXT transmission image of -12-10 reflection showing prismatic slip of TEDs; (b) Schematic drawing of TEDs glide on the prismatic plane

1.3.4 Basal plane dislocation and Shockley partials

Basal plane dislocations (BPDs) refer specially to those dislocations lying on (0001) basal plane and having Burgers vector of one ***a***. BPDs in SiC are actually composed of two partial dislocations separated by a narrow band of Shockley fault with width of 30-70 nm [38]. The partial dislocations have Burgers vector of 1/3<1-100> type, according to the following reactions:

$$1/3\langle 11\text{-}20\rangle \rightarrow 1/3\langle 10\text{-}10\rangle + 1/3\langle 01\text{-}10\rangle \quad (1)$$

In the case of compound semiconductors, the core of the dislocations consists of only one atom type; that is to say, for SiC, the Shockley partial dislocations are either Si-core or C-core [39]. For example, a 60° BPD dissociates into a 90° and a 30° partial having the same core structure (either both Si-core or both C-core); A screw BPD dissociates into two 30° partials having different core structure (one Si-core and the other one C-core). Pirouz et al. suggest that above the brittle-to-ductile transition temperature ($T_{BDT,}$ in the range from 1030 ℃ to 1100 ℃ depending on stain rates in the deformation tests) two partials of a BPD can glide in tandem on the basal plane in response to stress, while below T_{BDT} only the Si-core partial is able to glide, which causes the expansion of the Shockley fault. Such mobility difference between partials with different core structures also exists in the situation of electron-hole recombination enhanced dislocation motion in bipolar devices (for example pin diodes) under forward bias [22]. Si-core partials can couple with electron-hole recombination and move while C-core partials cannot, which results in the expansion of Shockley faults. It has been proved by various studies, such as synchrotron x-ray topography [40, 41], electroluminescence [42], cathodoluminescence [43], transmission electron microscopy (TEM) [44], that such expansion of Shockley faults is responsible for the degradation of SiC bipolar devices. The expanded Shockley faults can impede current flow and thus increase the on-state resistance of the devices, leading to increase in the forward voltage drop [22].

Since BPDs are an obvious nucleation site for Shockley faults, reducing BPD density in epilayers, which devices are built on, could be the most straightforward strategy to prevent the damage. One major source of BPDs in the epilayers is the BPDs that reach the surface of substrate, which is cut several degrees off the basal plane. Most of these BPDs (>85%) can be converted to TEDs during the initial epitaxial growth within several microns, without any special treatment [45]. This phenomenon can be interpreted as a result of image force [46] attracting BPDs toward the free surface. Many technical approaches have been used to increase the conversion ratio from BPDs to TEDs, for example, using the substrate with smaller off-cut angle [47], applying molten KOH etching on the substrate surface before epitaxial growth [48, 49], or implementing in situ growth interruption which induces hydrogen etching (>98% conversion ratio reported) [50, 51].

1.3.5 Interfacial dislocation and half loop array

It has been reported that the BPDs replicating into the epilayer are all of screw type with line direction parallel to the step flow direction [11-20] [52]. While screw BPDs in the epilayer can be a nucleation site for Shockley faults, they can become even more harmful if they are forced to glide during the epitaxial growth to simultaneously produce interfacial dislocations and half loop arrays [53]. The structure of interfacial dislocations and half loop arrays is schematically shown in Figure 1.7. The screw BPD was first propagated from the substrate and

then forced to glide on the basal plane in the epilayer. At the down-step side (step-flow direction) on the growth front, the gliding screw BPD frequently produces short BPD segments which are not screw oriented any longer and can immediately convert to TEDs at both ends of the segments [54], forming half loop arrays in the wake of glide. At the up-step side (opposite to step-flow direction) behind the growth front, a long BPD segment, which is referred to as interfacial dislocation, conserving the same Burgers vector with the gliding screw BPD is produced in the wake of glide along the intersection of the substrate/epi interface and the basal plane. Since the Burgers vector is 90 °to the line direction, the interfacial dislocations are edge type BPDs. At this point, new nucleation sites for Shockley fault, i.e. the interfacial dislocation and the short BPD segments of half loop arrays, are generated. One driving force for the formation of interfacial dislocations and half loop arrays is the misfit strain induced by doping level difference between the epilayer and the substrate when a critical thickness of the epilayer is reached [55]. Another driving force, demonstrated by X. Zhang et al., is the thermal stress induced by temperature gradient across the epi wafer exceeding a critical value [56].

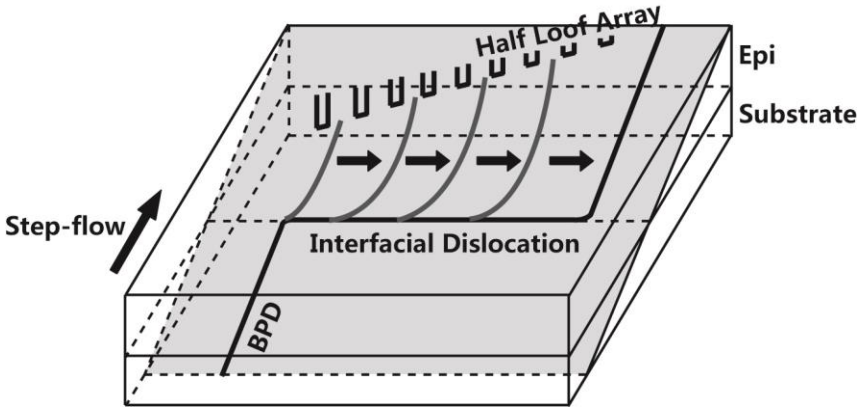

Figure 1.7 Schematic drawing of the formation of an interface dislocation and half loop array through sideway glide of a BPD in the epilayer

1.3.6 Stacking faults — Shockley fault, double Shockley fault, and 8H fault

As described above, Shockley faults are created by glide of Shockley partials with Burgers vector of 1/3<-1100> type. Glide of a Shockley partial dislocation on the basal slip plane can change the SiC tetrahedra from untwinned structure to twinned structure (or from twinned to untwinned) by shifting atoms to a different stacking position, as illustrated in Figure 1.8, and thus glide of Shockley partial on just one basal slip plane can change the original (22) stacking sequence of 4H-SiC to a faulted stacking sequence of (31), as shown in Figure 1.9, column II. Above and below the faulted region, the material retains the (22) stacking sequence.

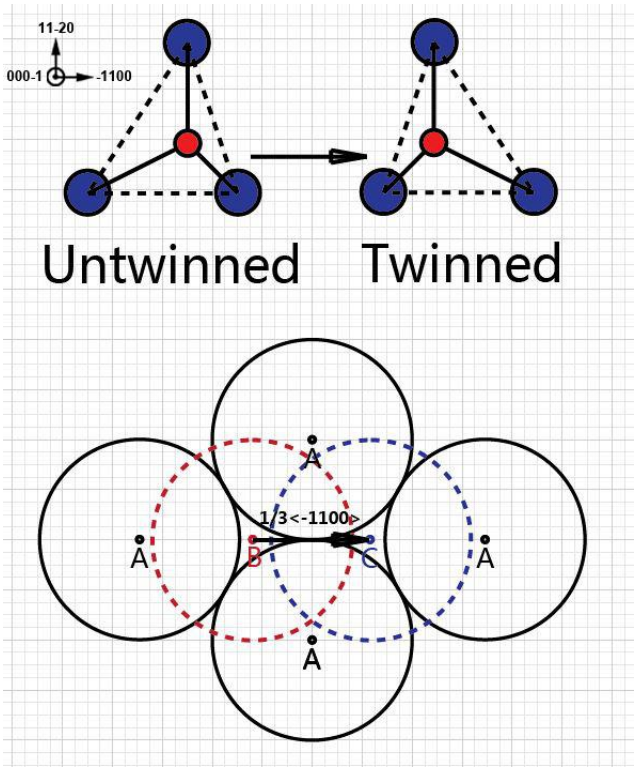

Figure 1.8 Change of stacking position from B to C due to glide of Shockley partial on the basal slip plane and the consequent change of SiC tetrahedra structure from untwinned to twinned

If there is another Shockley partial gliding on the adjacent basal slip plane, the so-called double Shockley fault (DSF) will be generated with a faulted stacking sequence of (60) (note that in many references this stacking sequence is referred to as (62)), as shown in Figure 1.9, column III. It has been reported that a high density of DSFs could be generated, during high temperature processing, in the heavily nitrogen-doped epilayers [24, 25] or in the area of epi-wafers where the nitrogen doping concentration is higher than in the rest area in the substrates [23, 57]. J. Liu reported DSFs were generated in bare substrate wafers having high doping concentrations during annealing under stress less condition and thus excluded that stress as the driving force for the formation of DSF [58]. Pirouz et al. interpreted the electronic mechanism of stacking fault expansion (developed by Miao et al. [59]) and demonstrated that there is an intrinsic driving force for the generation of DSFs in 4H-SiC crystal with high nitrogen doping concentration [23]. DSFs can produce an energy level lower than the conduction band in the bandgap of 4H-SiC material. For the heavily nitrogen doped 4H-SiC material ($2X10^{19}cm^{-3}$ for the theoretical threshold doping concentration), the Fermi level can be raised so much that it is higher the energy level induced by DSFs. Electrons tend to fit in this defect level if there are DSFs generated and thus lower the energy state, which provides the intrinsic driving force for the formation of DSFs. Specifically, when the energy difference between the Fermi level and the defect level is large enough to compensate the stacking fault energy which is required for increasing the area of DSFs, the system (crystal) becomes favorable to having DSFs. Even so, the expansion of DSFs (or say, the movement of two Shockley partials at the same time) still needs to overcome the activation barrier (Peierls energy [60]). The energy to overcome this

barrier can be thermal when increasing the temperature of the system. The nucleation sites for DSFs could be two BPD segments close to each other on adjacent basal slip planes.

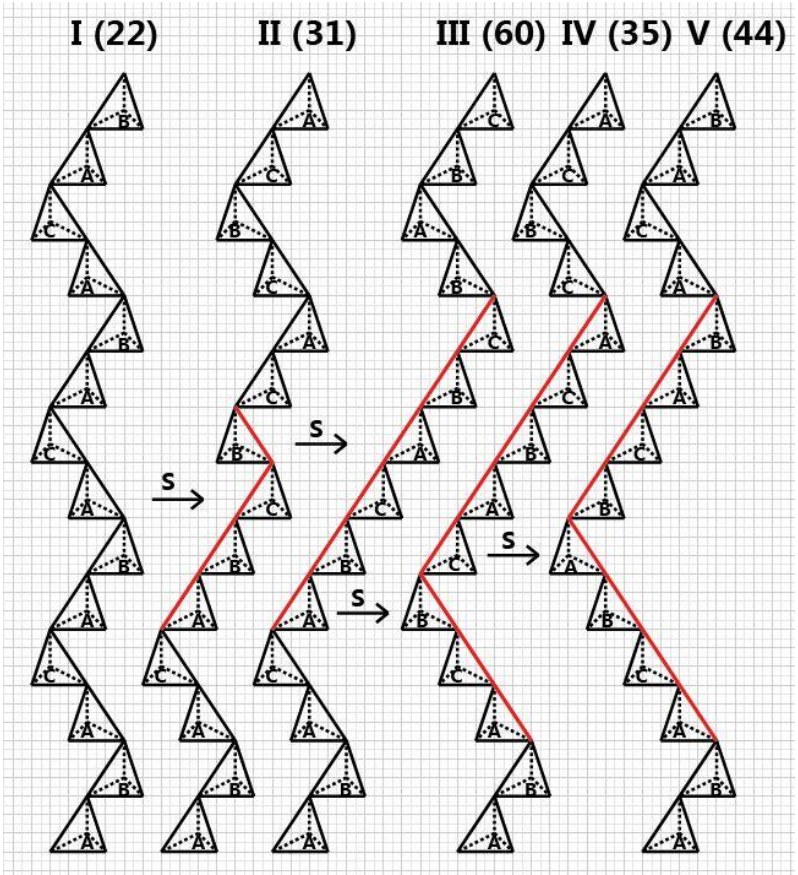

Figure 1.9 Glide of Shockley partials on different basal slip planes gradually changing stacking sequence from (22) at column I to (31) at column II , to (60) at column III, to (53) at column VI and to (44) at column V

If glide of Shockley partial happens on another two neighboring basal slip planes starting from the (60) stacking sequence of DSF, an 8H fault [26, 61-63] with (44) stacking sequence will be created, as schematically shown in Figure 1.9 from column III to V. Although (44) stacking sequence of 8H fault can be artificially created in the drawing by glide of Shockley partials on four consecutive basal slip planes, a mechanism to explain such concerted movement of dislocations is lacking. In reality, there is unlikely to be proper nucleation sites like four BPD segments on top of one another along c-axis direction, especially considering the situation that observation of 8H faults are observed not as an independent event but seems quite often. 8H faults are observed to have triangular shape opening toward down-step direction and their length corresponds to the width of the basal plane in the off-cut epilayer [26, 61], which all suggest that 8H faults nucleate at the epi/substrate interface and then extend as the step flow continues. So far, the mechanism of why/how 8H faults can be generated during the epitaxial growth is still open for discussion. General topics about transformation of stacking sequences in 4H-SiC will be discussed in Chapter 11 and 12.

1.3.7 Stacking faults — intrinsic Frank fault, carrot defect

Tsuchida et al. observed stacking faults having (50) stacking sequence [64], which is the same structure of the intrinsic Frank fault predicted by Skowronski et al. [22], in the 4H-SiC epilayers. These Frank type stacking faults are connected to TSDs at their nucleation points in two ways: (1) to the TSDs in the substrate, as schematically shown in Figure 1.10(a); (2) to the TSDs in the epilayers, as schematically shown in Figure 1.10(b). The first case can be interpreted to be nucleation of a stacking fault from the surface spiral associated with a TSD on the substrate surface in the beginning of epitaxial growth when misalignment happens to the merging of spiral steps and vicinal steps [64]. The second case can be the situation when a new TSD and a stacking fault are simultaneously generated in the epilayer during epitaxial growth, though without a clear formation mechanism.

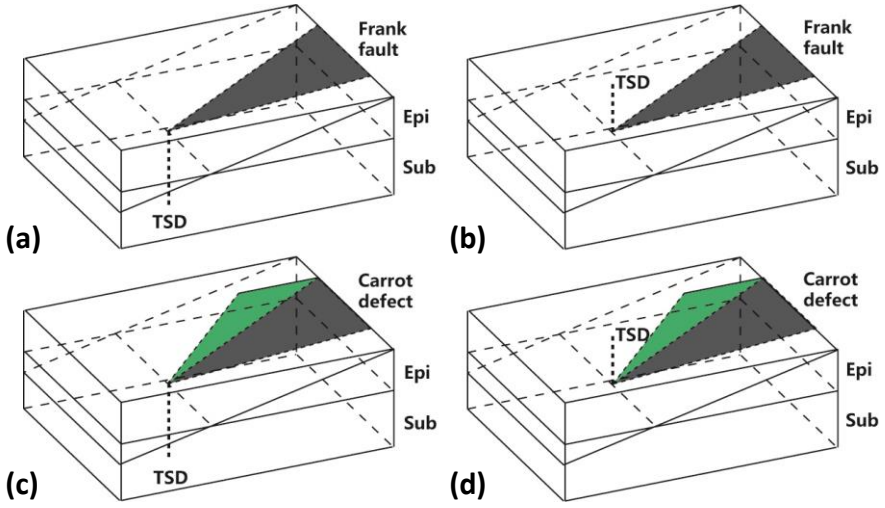

Figure 1.10 Configurations of intrinsic Frank faults and carrot defects: (a) TSD in the substrate converts to intrinsic Frank fault in the epilayer; (b) simultaneous nucleation of TSD and intrinsic Frank fault in the epilayer; (c) TSD in the substrate converts to carrot defect in the epilayer; (d) simultaneous nucleation of TSD and carrot defect in the epilayer

Unlike the other stacking faults described above, carrot defects can be easily observed with optical microscope and their name come from their surface morphology. Carrot defects are also observed to connect to either TSDs in the substrate or TSDs in the epilayer at their nucleation points [52, 65, 66]. The configuration of carrot defects are compared with intrinsic Frank faults in Figure 1.10. A carrot defect consists of one stacking fault on the basal plane and anther stacking fault on the (1-100) prismatic plane in the epilayer. The fault vector (displacement vector) of the basal fault has been determined to be 1/12[4-403] using different diffraction conditions of TEM [65] and the stacking sequence has been observed to be (30) using high resolution TEM [52]. A general topic about correlation between fault vectors and stacking sequences in 4H-SiC will be discussed in Chapter 11. For the prismatic fault, it is only known that its fault vector is different from that of the basal fault, and its atomic structure is still unclear.

In addition to the stacking faults listed in Table 3, several new types of stacking faults have been investigated in the studies of this dissertation and their structures and formation mechanisms will be discussed in Chapters 6 to 10.

1.3.8 3C triangular inclusion

Triangular defects in 4H-SiC used to specially refer to those defects in the epilayer with large triangular surface morphological features [67], which were actually determined to be 3C polytype inclusions [68]. Synchrotron x-ray topography studies reveal that no defects in the regular substrates or on their surface, such as TSDs or growth pits, are directly associated with the formation of 3c triangular inclusions. Furthermore, it is found that increasing the off-cut angles of substrates greatly reduces both the size and the density of 3C-SiC inclusions [68].

The 4H-SiC homoepitaxial layers are usually grown using a special CVD growth technique, called "step controlled epitaxy" [69]. It features using the substrates with several degree off-cut angles so that the terraces at the growth front can be narrowed and the adsorbed species can reach the steps. Thus vicinal step flow growth can overcome 2D nucleation to realize polytype control. The steps at the growth front serve as a template to ensure the growth of the same polytype. When the step density is low or the supersaturation is high, some degree of 2D nucleation will happen. The 2D nucleation of polytypes is thermodynamically determined by growth conditions, especially the temperature. For the temperature range (1200 ℃ – 1600 ℃) of CVD growth of 4H-SiC, 3C polytype is more stable [70, 71] and 2D nucleation tends to generate 3C polytype. Studies show that low temperature or high C/Si ratio can easily lead to the formation of 3C triangular inclusions [17, 72].

1.4 Motivation

As discussed above, although 4H-SiC possesses superior properties which make it the ideal material for fabrication of next generation power devices, various defects generated during either crystal growth, device fabrication, or even device operation can impede realization of the great potential of this material. For the community who are committed to eliminating the defects or mitigate their hazards, it is important to gain a correct and complete understanding of different kinds of defects, involving their locations, structures, origins and formation mechanisms. However, it is always easier said than done. Firstly, it is very often that our understanding is subject to the limited information we can possibly obtain. For example, the TSD density in 4H-SiC was extreme high ($>10^4 cm^{-2}$) for quite a long time and x-ray topography studies on the individual dislocations was difficult to carry out due to complications of image overlap at high density. Recently, the overall defects density in 4H-SiC was greatly decreased due to better thermal stress control during the crystal growth, which provides a unique opportunity to study details of dislocation behavior using x-ray topography. As a result, threading c+a dislocations have been recognized from those traditionally considered as threading screw dislocations (see Chapters 3) and they actually account for more than half of the total number of threading dislocations with c-component of Burgers vector. Secondly, new defect types keep being discovered as diverse strategies have been tested to increase the crystal size or to improve the crystal quality. Such examples include six-pointed-star shaped stacking faults discussed in Chapter 8, 6H stacking faults discussed in Chapter 9, and V shaped defects discussed in Chapter 10. The primary motivation for the studies in this dissertation is to improve the understanding of

4H-SiC material, defects, growth and applications, in collaboration with the whole SiC community.

2. Experimental Techniques

2.1 Synchrotron x-ray topography

2.1.1 Synchrotron X-ray

Synchrotron radiations are the electromagnetic radiations emitted when electrons are radially accelerated to a high energy level in various synchrotron sources. They have a continuous spectral distribution. At the Stony Brook Synchrotron Topography, Beamline X-19C at the National Synchrotron Light Source (NSLS), the original beam successively passes through a 254 um thick beryllium window, an 25.4 um thick aluminum foil vacuum shield, and a 4 meter long air path and as a result, the spectral distribution is in the range of 0.2 to 2 Å with its maximum at 0.8 Å and is thus called synchrotron white beam x-ray. Synchrotron monochromatic beam can be obtained from the white beam x-ray when it passes a monochromator is applied which is usually channel-cut, highly perfect silicon single crystals [73]. Synchrotron x-ray intensities are several orders of magnitude higher than conventional x-rays from laboratory sources, so the exposure time for recording an x-ray topograph can be significantly reduced in inverse ratio.

Since there is no magnification involved, resolution in synchrotron x-ray topography is controlled by geometry. The geometrical spatial resolution (R_s) o f a topograph is determined in the following equation:

$$R_s = D_{sf}\frac{S_h}{D_{ss}} \quad \text{.....(2)}$$

where S_h is the source dimension and D_{sf} and D_{ss} are the sample-to-film distance and the source-to-specimen distance. At Beamline X-19C at NSLS, the effective source size is (0.15mm x 0.35mm) and the long source-to-specimen distance is 25m, which give rise to the spatial resolution of about 1.4um at a specimen-to-film distance of 10cm.

The divergence angle of synchrotron radiation is given approximately by m_0c^2/E, where m_0 is the rest mass of electron, c is the velocity of light and E is the electron energy. This vertical divergence for NSLS is typically 0.1 mrad (20'') while the horizontal divergence is typically 0.7 mrad (140''). The large specimen-to-detector distance (up to 30cm with acceptable spatial resolution) at Beamline X-19C at NSLS greatly enhances the angular resolution and thus can separate contrast features that is associated with misorientation induced by defects like grain boundaries.

2.1.2 Imaging Geometry

All x-ray topographic methods are based on the reflection of x-rays by a set of lattice planes (hkl) of a crystal and must obey Bragg's law which can be expressed in the following equation [74]:

$$2d_{hkl}sin\theta_B = \lambda \quad \text{.....(3)}$$

where λ is the wavelength of the X-rays, d_{hkl} is interplaner spacing and θ_B is the reflection angle.

For synchrotron monochromatic beam x-ray topography (SMBXT), the x-ray beam is incident on the single crystal at a set Bragg angle to the diffraction plane and the corresponding diffracted beam is projected onto a two dimensional detector (usually high resolution x-ray films). The recorded two-dimensional diffraction spot constitutes an x-ray topograph, contrast of which gives the information about variation of the diffracted intensity as a function of position. The local diffracted intensity is affected by the displacement field associated with a defect. Through interpreting the contrast of intensity variation, different defect types can be characterized.

For synchrotron white beam x-ray topography (SWBXT), a single crystal is placed at a particular orientation in the path of the x-ray beam and each set of atomic planes will select a particular wavelength to diffract the incident beam according to Bragg's law. Each spot of the diffraction pattern obtained on the x-ray film constitutes an x-ray topograph.

2.1.2.1 Transmission geometry

When the incident and diffracted beams enter through and exit from opposite faces of a crystal, the diffraction geometry is called the transmission geometry (Figure 2.1(a)). Since the x-rays pass through the entire thickness of the sample, this technique is used to characterize overall defect content of a crystal. The high intensities of synchrotron x-ray make it possible to record images from relatively thick specimens using this technique.

2.1.2.2 Reflection geometry

When the incident and diffracted beams enter through and exit from the same face of a crystal, the diffraction geometry is called the reflection geometry (Figure 2.1). This technique is generally used to characterize a limited volume close to the surface of crystals, especially when crystals are either too thick, or when absorption conditions are too high, or when defect densities are too high to permit the use of the transmission geometry. Owing to its surface sensitivity, topography in the reflection geometry is also useful for the characterization of surface defects within epitaxial layers.

The penetration depth of x-ray into the crystals is determined either by the kinematical penetration depth (in imperfect crystals) or by the dynamical penetration depth (in highly perfect single crystals). The kinematical penetration depth (t^k_p) can be determined simply by geometrical relations between the incident and diffracted beams when the fractional decrease in the beam intensity (I_0/I) is set, and is given by [75]:

$$t = \frac{\ln(I_0/I)}{\mu(\frac{1}{sin\Phi_0}+\frac{1}{sin\Phi_h})} \quad \text{.....(4)}$$

where μ is the linear absorption coefficient, and Φ_o and Φ_h are the angles of the incident and diffracted beams with respect to the surface respectively.

The dynamical penetration depth z_e is given by:

$$z_e = \frac{\xi_g}{2\pi\sqrt{1-\eta^2}} \quad \text{.....(5)}$$

Where η is the deviation parameter (the deviation from the rocking curve peak) and ξ_g is the extinction length (the period of the beat in Pendell ösung effect) [76].

Since the main contrast from dislocations in 4H-SiC projection topography is generated by x-rays being diffracted kinematically from the distorted region associated with dislocations, the kinematical penetration depth is chosen to determine the penetration depth in the studies of this dissertation.

Two important reflection geometries, i.e. back reflection and grazing-incidence diffraction, are frequently used in x-ray topography studies.

(1) Back Reflection

The back reflection is the reflection geometry when the incident beam enters the crystal with an angle close to 90 ° and the diffracted beam exits the same face with a large angle to the surface (Figure 2.1(b)). The back reflection has a relatively large penetration depth.

(2) Grazing-incidence diffraction

In grazing geometry, the incident beam enters the crystal with a small angle and the diffracted beam exits the same face with an angle close to 90 ° to the surface (Figure 2.1(c)). Grazing-incidence diffraction has better near surface sensitivity, since the grazing angels of the incident and diffracted beams can be easily varied, so that topographs can be recorded at different penetration depths from several hundred nanometers to dozens of microns and thus can create a depth profile of the defects in the inspected volume of the crystal.

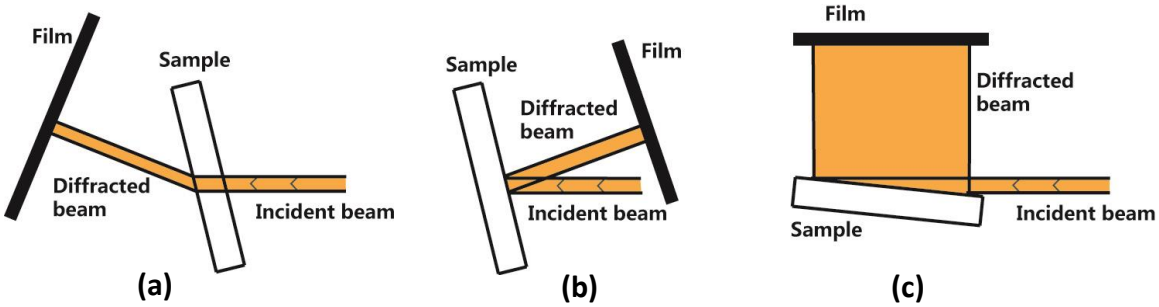

Figure 2.1 Imaging geometries for x-ray topography: (a) Transmission; (b) Back reflection; (c) Grazing-incidence diffraction

2.1.3 Contrast from perfect crystals

Two fundamental theories have been developed to interpret the intensities observed in x-ray diffraction studies: the kinematical theory and the dynamic theory. In kinematical theory, an assumption is made that x-rays penetrating the materials will only diffracted by atomic planes for once and then pass through the materials without further diffraction. A reasonable accuracy can

be obtained when it is used to account for the diffracted intensities from powder or small crystals. However, the measured intensities of diffracted beams from perfect single crystals at large sizes are significantly less than the theoretically predicted ones, which suggests that the kinematical theory breaks down for such applications.

In dynamic theory [76], x-rays entering the perfect crystals will be diffracted many times by atomic planes before exiting from the crystals. Each time x-rays are diffracted from an atomic plane, a phase change of $\pi/2$ will be induced. As schematically shown in Figure 2.2, when x-rays get diffracted twice by the atomic planes, they propagate in the same direction as the incident beam but are complete out of phase (a phase change of π), leading to a reduction in the total diffracted intensities. This effect is referred to as primary extinction.

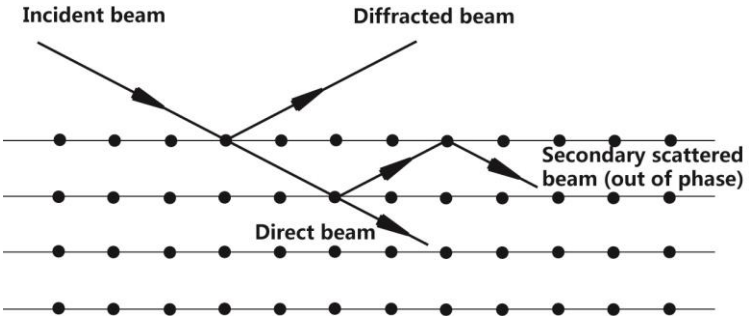

Figure 2.2 Schematic showing primary extinction

2.1.4 Contrast from Defects

The contrast from defects in x-ray topographs are either dark or light contrast relative to the grey background. The background is produced when the crystal which contains defects but remains perfect crystalline structure in most regions diffracts the x-ray beam dynamically. Dark contrast from defects is due to enhanced intensities diffracted from the local regions around defects and on the contrary, light contrast is due to reduced intensities. There are two fundamental mechanisms for contrast generation from defects in x-ray topographs, i.e. orientation contrast and extinction contrast. The dominant contrast formation mechanism strongly depends on crystal properties and dimension, the defect type and density, the type of x-ray beam and imaging geometry. Contrast from defects in SWBXT topographs recorded in transmission geometry is discussed here using grain boundaries and dislocations in 4H-SiC for examples. Compared to the conventional x-ray source which is usually monochromatic beam with angular divergence around 0.1° (360’’), the synchrotron white beam x-ray has continuous spectrum and the angular divergence is much smaller around 80’’, which makes interpreting the contrast of SWBXT slightly different from that of conventional x-ray topography.

2.1.4.1 Orientation contrast

Orientation contrast arises when a part of the crystal is misoriented from its bulk matrix so that the diffracted image from the misoriented region is projected in a direction different from the matrix. Change of crystal orientations across grain boundaries is abrupt and consequently in SWBXT all the sub-grains will automatically choose their own wavelength from the white

spectrum to diffract the x-ray beam according to the Bragg's law. Black-strip-like contrast appears when the two images diffracted from the sub-grain and the bulk matrix overlap and white-strip-like contrast appears when the two images diffracted from the sub-grain and the bulk matrix separate, as schematically shown in Figure 2.3(a). For a sub-grain which is completely included in the matrix, the observation is expected that contrast from the boundary on one side of the sub-grain is black and contrast from the boundary on the other side is white, like the example shown in Figure 2.3(b). The image width of the orientation contrast is geometrically determined by the sample-to-film distances and the misorientation angle caused by the defect.

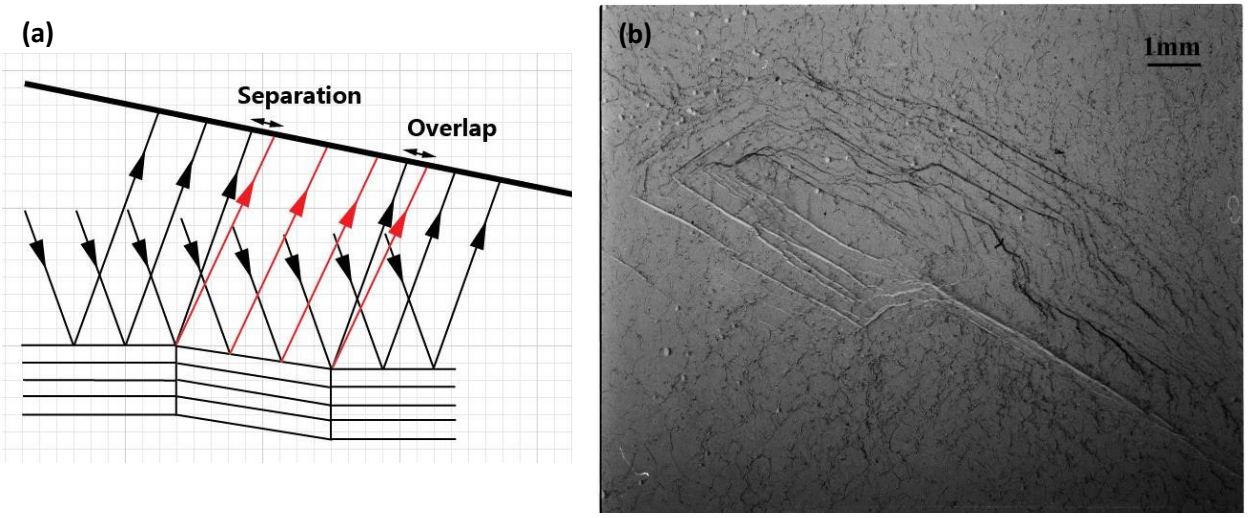

Figure 2.3 (a) Schematic showing orientation contrast; (b) Gazing-incidence SWBXT image of 11-28 reflection showing contrast from grain boundaries

2.1.4.2 Extinction contrast

Extinction contrast occurs when the diffracting power in the vicinity of a defect differs from the bulk matrix and consists of three components: direct image, dynamic image and intermediate image [76]. Depending on absorption conditions (the product of the linear absorption coefficient μ and the thickness of the crystal t), the contrast mechanism varies: under low absorption conditions ($\mu t<1$), direct image gives the dominant contrast; under high absorption condition ($\mu t>4$), dynamic image gives the dominant contrast; under medium absorption condition ($1<\mu t<4$), the intermediate image can be identified. Since 4H-SiC has low linear absorption coefficient (in Table 4) and samples inspected in the studies of this dissertation usually have thicknesses between 300um and 500um, the absorption condition is in the low region and hence the direct image dominates the contrast from defects like dislocations.

For a specific wavelength, the dynamical diffraction allows reflecting of the incident beam at a narrow range around the Bragg angle θ_b, which is known as the rocking curve width $\Delta\theta$. The rocking curve with is in the order of a few seconds of arc (in Table 4) and is much smaller than the divergence of the incident beam, which means that only a small proportion of the incident beam will actually undergo diffraction. However, the lattice misorientation induced by defects like dislocations will allow the part of incident beam outside the rocking curve to diffract. The misoriented regions associated with dislocations are very limited and thus don't

suffer from primary extinction, in others words, they diffract kinematically. Therefore, the diffracted intensities from dislocations are higher than that from the bulk matrix and hence dark line images will appear on the X-ray film. Images produced in such way are referred to as direct images. For white beam x-ray, the increase in diffracted intensities from dislocations can also be caused by the lattice dilation induced by dislocations, because the distorted lattice planes can select the right wavelengths from the continuous spectrum to diffract more incident x-rays.

Table 4 Various parameters for reflections in SWBXT studies of 4H-SiC crystals in this dissertation

hkil	d_{hkl} (Å)	θ_b	λ (Å)	μ (mm^{-1})	F_{hkl}	Δθ	Geometry
0004	2.51	6°	0.52	0.5	40.8	2.66''	Transmission
11-20	1.54	10°	0.53	0.6	41.2	1.69''	Transmission
1-100	2.67	8°	0.74	1.6	13.48	1.42''	Transmission
1-101	2.58	7°	0.62	1	19.98	1.66''	Transmission
11-28	0.97	37.2°	1.17	6.4	18.46	1.31''	Grazing, t^k_p= ~38um
* d_{hkl} : interplanar distance; θ_b : Bragg angles; λ : wavelength; μ : linear absorption coefficient; F_{hkl} : structure factor; Δθ : rocking curve width							

2.2 High resolution transmission electron microscopy

High resolution transmission electron microscopy (HRTEM) is a microscopy technique that can produce atomic-resolution images. Specifically, the TEM experiment tool JEOL 2100F, used in the studies of this dissertation can provide a 1.9Å point-to-point resolution. Like other TEM techniques, the images are formed after an electron beam passes through and interacts with an ultra-thin specimen. The main different is that the contrast in HRTEM images relies on phase contrast which arise from the interference of the scattered electron waves having differences in the phase [77]. Unlike other forms of TEM imaging, such as bright field or dark filed, which select a single transmission beam either the direct beam or one of the diffracted beams, a phase-contrast image requires the selection of more than one beams and the more beams collected, the higher the resolution. Figure 2.4 shows typical HRTEM images of 3C- and 4H-SiC on 11-20 axes. It is necessary to point out that the images generated by phase contrast actually consist of on-axis lattice fringes, though they look so like direct images of atomic planes. Technically, one needs to run simulations to interpret the lattice-fringe images; however, in most cases, many lattice-fringe images (at least >99%) can be interpreted intuitively if one have gained basic knowledge about the material and defect structures. For example, it can be easily recognized from the HRTEM image in Figure 2.4 that 4H-SiC has a stacking sequence of (22).

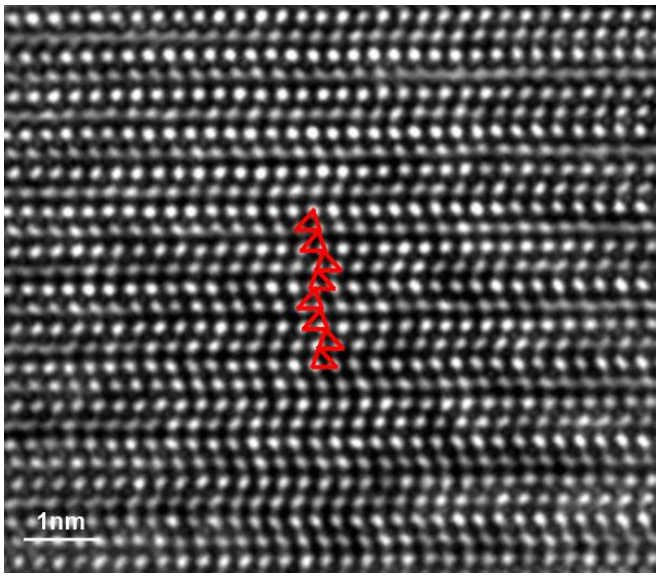

Figure 2.4 HRTEM image showing (22) stacking sequence of 4H-SiC

To generate TEM images, electrons must pass through the specimens and thinner the specimen, better the image quality. For HRTEM, the specimen thicknesses should be less than 50nm, and this strict requirement makes the specimen preparation very difficult. The specimens can be first mechanically polished down to 1um and then finally thinned down by ion milling in which energetic ions (usually Ar or He) are bombarded onto the polished specimens and sputter the material out. Alternatively, TEM specimens can be prepared with a focused ion beam (FIB) tool, which can make patterns on the wafer surface with ion beam (usually Ga) and then directly lift out slabs (~1um) of materials and mount them onto TEM grids with a probe. These slabs of materials will next be precisely thinned down with ion beam inside the same tool.

2.3 Chemical etching

Chemical etching is extensively used for defect evaluation due to its merits of low cost, and simple experimental procedure [78]. Although SiC materials are highly inert chemically, they can be etched by molten potassium hydroxide (KOH) at 450-600 ℃. The etch pits are produced because the local etch rates at defects are different compared with the defect-free regions. Different patterns of etch pits arise due to the inhomogeneous nature of defects (either in composition, physical structure, or both) compared with the crystal matrix. After different etch pits patterns are carefully calibrated with defects directly observed with other techniques such as X-ray topography, TEM, or AFM, they can be used to estimate defect densities in the crystal by measuring the etch pit densities. Figure 2.5 shows an area from the surface of an off-axis 4H-SiC wafer after KOH etching at 580 ℃ for 12 minutes and at least three types of etch pits can be observed. The large hexagonal pits correspond to threading screw dislocation (TSDs); the small hexagonal pits (some may look like round) correspond to threading edge dislocations (TEDs); the small oval pits correspond to basal plane dislocations (BPDs). Besides, an etch pit pattern of stacking fault can be found in Chapter 10, which is composed of a shallow trench that

corresponds to the surface intersection of the stacking fault and two small oval pits that correspond to the two partial dislocations bounding the stacking fault.

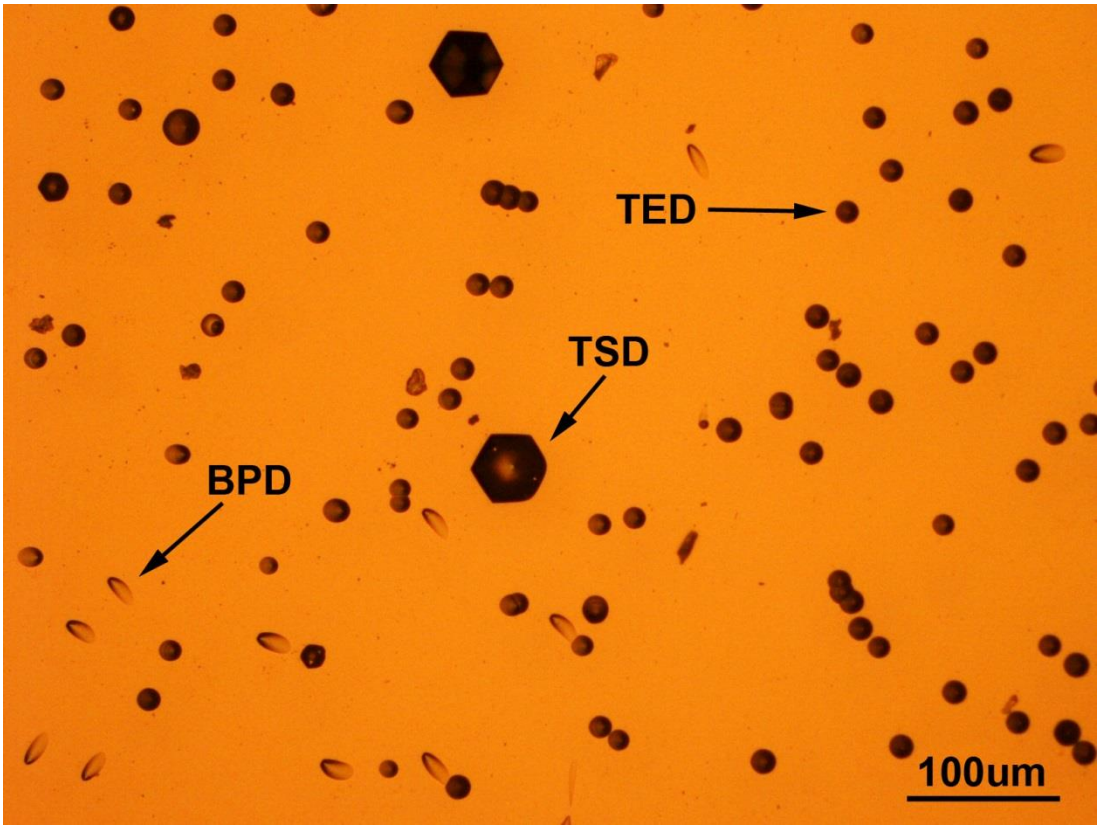

Figure 2.5 Optical image recorded from Si face of 4H-SiC wafer after KOH etching at 580°C for 12 minutes

3. Direct observation of the Existence of Threading c+a Dislocations

3.1 Outline.

Synchrotron White Beam X-ray Topography (SWBXT) imaging of wafers cut parallel to the growth axis from 4H-SiC boules grown using Physical Vapor Transport has enabled visualization of the evolution of the defect microstructure. Observations are presented of the propagation and post-growth mutual interaction of threading growth dislocations with *c*-component of Burgers vector. Detailed contrast extinction studies reveal the presence of two types of such dislocations: pure *c*-axis screw dislocations and those with Burgers Vector n_1**c**+n_2**a** [79], where n_1 is equal to 1 and n_2 is equal to 1 or 2. In addition, observations of dislocation propagation show that some of the threading dislocations with *c*-component of Burgers adopt a curved, slightly helical morphology which can drive the dislocations from adjacent nucleation sites together enabling them to respond to the inter-dislocation forces and react. Since all of the dislocations exhibiting such helical configurations have significant screw component, and in view of the fact that such dislocations are typically not observed to glide, it is believed that such morphologies result in large part from the interaction of a non-equilibrium concentration of vacancies with the originally approximately straight dislocation cores behind growth front. Such interactions can lead to complete or partial Burgers vector annihilation. Among the reactions observed are: (a) the reaction between opposite-sign threading screw dislocations with Burgers vectors **c** and –**c** wherein some segments annihilate leaving others in the form of trails of stranded loops comprising closed dislocation dipoles; (b) the reaction between threading dislocations with Burgers vectors of **-c**+**a** and **c**+**a** wherein the opposite **c**-components annihilate leaving behind the two **a**-components; (c) the similar reaction between threading dislocations with Burgers vectors of **-c** and **c**+**a** leaving behind the **a**-component.

3.2 Introduction

Recent progress in bulk crystal growth of silicon carbide has enabled the effective elimination of the micropipe, arguably the most harmful defect in this material [14]. However, it is well known that other threading defects in this material can have a detrimental effect on device performance. For example, the impact of closed-core threading screw dislocations has been well documented [80, 81]. Recent reports have shown that such threading dislocations are not restricted to those of pure screw character but can comprise all dislocations with *c*-component of Burgers vector, i.e. with b= n_1c+n_2a [82-84]. In this part of the work, synchrotron X-ray topographic studies are carried out on axial slices taken from 4H-SiC boules wherein the densities of such defects are sufficiently low that detailed interactions can be discerned. Understanding the interactions between such threading dislocations is of great interest as this might provide insight into mechanisms by which their densities may be reduced.

3.3 Results and Discussion

Fig. 3.1 (a) shows an SWBXT image recorded with g=0004 from an axial slice exhibiting low threading dislocation density. Segments of six dislocations are visible although dislocations 3 and 4 appear to have interacted such that parts of their length (between the two arrows on Fig. 3.1(a)) have apparently annihilated. Figs. 3.1(b) - (f) show images recorded from the same region with g vectors of 0-110, 1-210, 01-11, 0-111, and 10-1-5. Note that dislocations 2 and 5 are out

of contrast on Fig. 3.1(b)&(c) so that they are pure screw in character, i.e. TSDs, **b**=**c**. The background in Fig. 3.1(b) consists of horizontal lines which are segments of basal plane dislocations and some short *c*-axis threading segments which are threading edge dislocations; both of these have Burgers vectors of 1/3<11-20> i.e. **b**=**a**, and are invisible (as expected) on Fig. 3.1(a). Note that line 1 is visible in the 0004, 0-110 and 11-20 reflections, which suggest that it is neither pure screw nor pure edge in character. However, it is invisible in Fig. 3.1(d) and computation of **g**.**b** shows that its Burgers vector is 1/3[1-213], i.e., **c**+**a**.

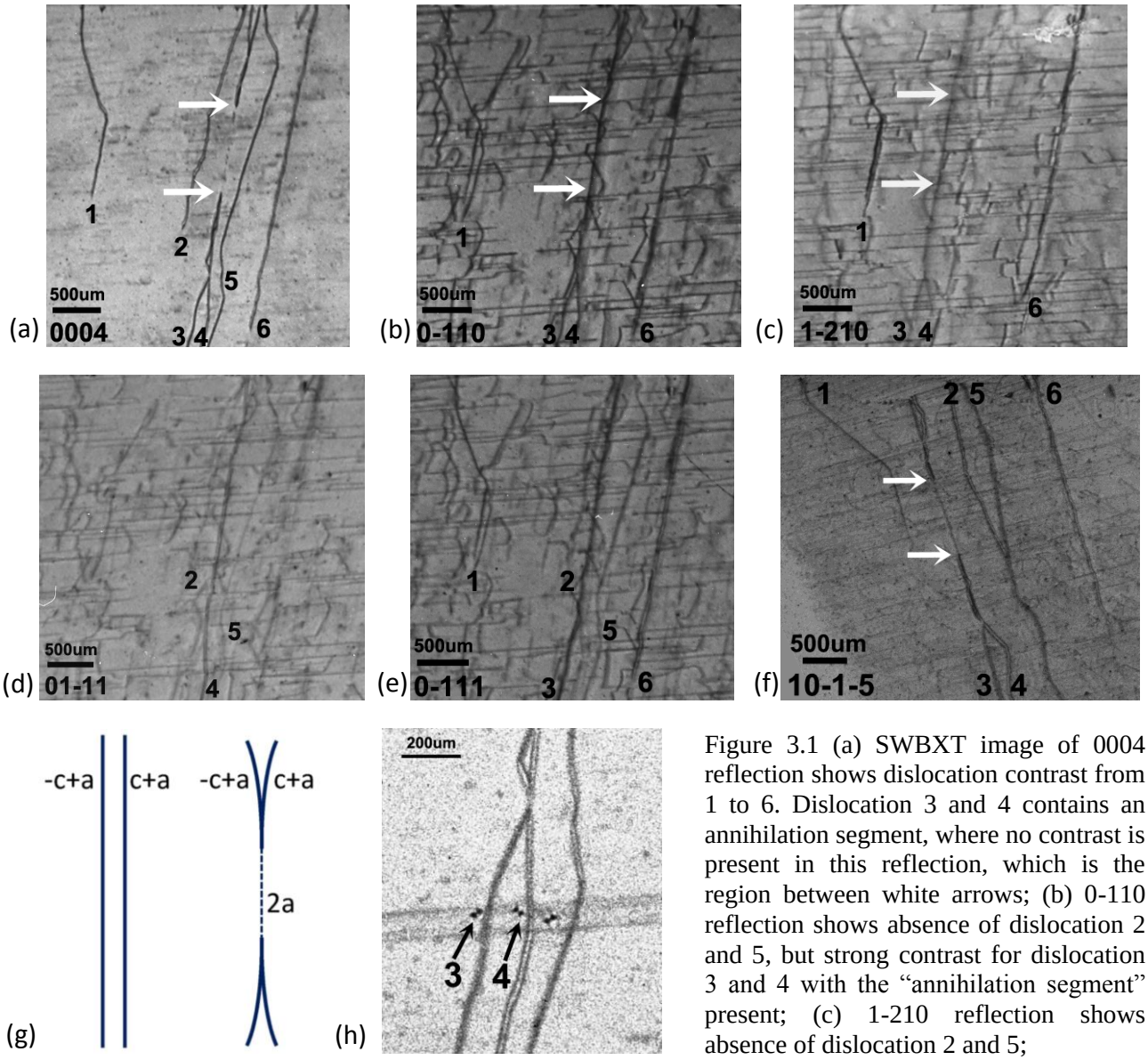

Figure 3.1 (a) SWBXT image of 0004 reflection shows dislocation contrast from 1 to 6. Dislocation 3 and 4 contains an annihilation segment, where no contrast is present in this reflection, which is the region between white arrows; (b) 0-110 reflection shows absence of dislocation 2 and 5, but strong contrast for dislocation 3 and 4 with the "annihilation segment" present; (c) 1-210 reflection shows absence of dislocation 2 and 5; (d) 01-11 reflection shows contrast from 2, 4 and 5; (e) 0-111 reflection shows contrast from 1, 2, 3, 5 and 6; (f) 10-1-5 reflection shows sharp difference in contrast between the partially annihilated segment, marked by arrows, and the rest of dislocations 3 and 4; (g) illustration of the reaction between $-c+a$ and $c+a$ dislocation; (h) overlapping 0004 section topograph on projection topograph shows opposite signs of dislocation 3 and 4, since their screw arrangements are mirror images.

By doing similar contrast analysis, the Burgers vectors of dislocations 3, 4 and 6 can be also determined as **c**+**a** type, as summarized in Table 5. In view of the fact that contrast from dislocations 3 and 4 is lighter than that from dislocation 1 in Fig. 3.1(c), it can be inferred that dislocations 3 and 4 have different *a*-component from dislocation 1. Performing **g**.**b** analysis using the suggested Burgers vectors in Table 5, dislocations 3 and 4 have a smaller **g**.**b** value than dislocation 1 when g is equal to 1-210, which explains the weaker contrast in Fig. 3.1(c). Careful examination of Figs. 3.1(d) and (e) shows that dislocations 3, 4 and 6 do not completely disappear in related <01-11> type reflections when **g**.**b**=0. This is due to the fact that these dislocations have mixed character and as such will exhibit very weak but not zero contrast when **g**.**b**=0 [76].

Further evidence for the existence of c+a dislocations in 4H-SiC can be found from the reaction between dislocation 3 and 4. In Fig. 3.1(a), a segment of line 3 and 4, marked with arrows, appears to have annihilated and shows no contrast. However, this segment is clearly present on Figs. 3.1(b)&(c), which suggest that it contains only an a-component of Burgers vector so that dislocations 3 and 4 only partially annihilate. As illustrated in Fig. 3.1(g), dislocation 3 and 4 have opposite sign c-components and these c-component annihilate while the two a-components are left behind. This can be further proved by Fig. 3.1(f) from which sharp difference in contrast between the partially annihilated segment, marked by arrows, and the rest of dislocations 3 and 4 can be observed. Fig. 3.1(f) is recorded from 10-1-5 reflection and the fourth index of this reflection is much bigger than others. When performing the **g**.**b** calculation, the c-component contributes much more to the final value, which means that the c-component shows much stronger contrast than the a-component in this reflection. Another interesting thing in Fig. 3.1(f) is that position of line 2 is shifted compared to its position in Fig. 3.1(a), because the 10-1-5 reflection is recorded by rotating the crystal through a large angle and differences in the depth position of the dislocations in the axial slice will appear as a change in relative line position. Fig. 3.1(h) shows a section topograph, which is sensitive to the sense of dislocation, shown overlapped onto an 0004 projection topograph. Arrows point to the contrast from dislocation 3 and 4 in the section topograph. From the sense of the mutual shift between the bimodal image components, it can be seen that dislocation 3 has right-handed screw components while dislocation 4 has left-handed, which confirms that dislocations 3 and 4 have opposite c-components which can thus annihilate.

Table 5 **g**·**b** values for dislocations from 1 to 6 in Fig. 3.1

g.b / **g** / **b**	**0004**	**0-110**	**1-210**	**01-11**	**0-111**	**10-1-5**
L1&6: 1/3[1-213], *c*+*a*	4	1	2	0	2	-5
L3: 1/3[-1-123], *c*+*a*	4	1	1	0	2	-5
L4: 1/3[-1-12-3], -*c*+*a*	-4	1	1	-2	0	5
L2&5: <0001> , TSD	4	0	0	1	1	-5
Arrow: 2/3[-1-120], 2*a*	0	2	2	-2	2	-2

Fig. 3.2 shows a similar reaction between –*c* and *c*+*a* dislocations. As illustrated in Fig. 3.2(a), the –*c* TSD annihilate with the opposite sign *c*-component of the *c*+*a* dislocation leaving

a single *a*-component behind. Dislocation 7, which is TSD, is visible in Fig. 3.2(b) and out of contrast in Fig. 3.2(c). Dislocation 8 is visible in both images, which suggest that it has both *c*- and *a*-components. The annihilated segment, marked by arrows, is invisible in Fig. 3.2(b) and visible in Fig. 3.2(c), which indicates that the annihilated segment has only an *a*-component of Burgers vector.

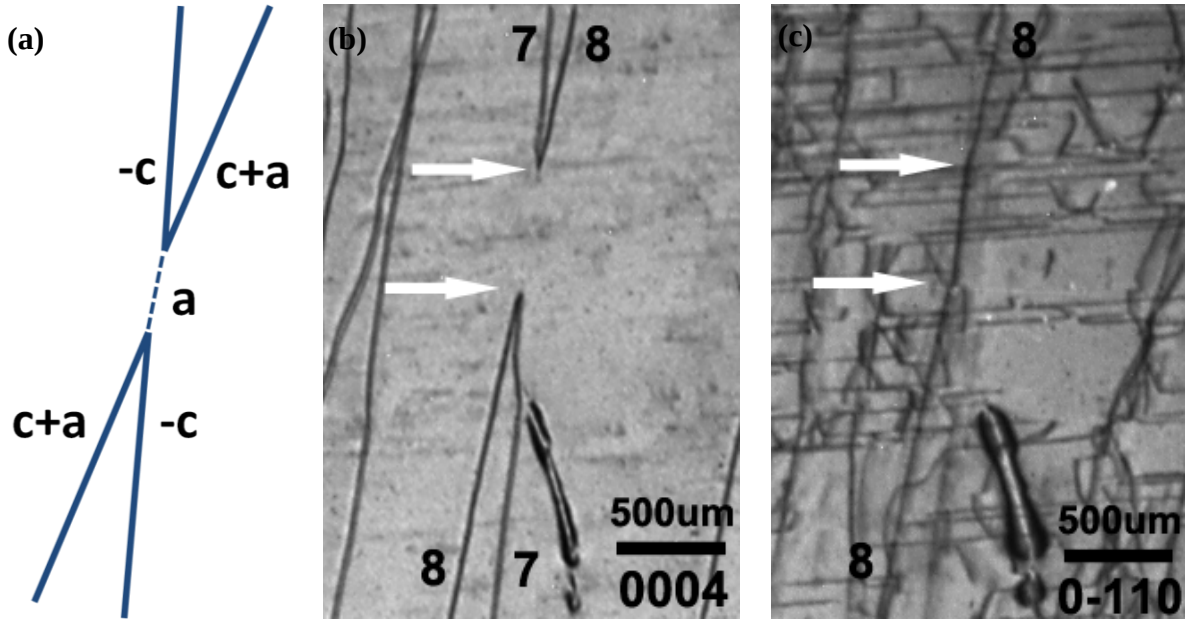

Figure 3.2 (a) illustration of the reaction between -*c* and *a*+*c* dislocation; (b) SWBXT image of 0004 reflection showing the annihilation of -*c* and *c*+*a* dislocation, named 7 and 8 respectively; (c) 0-110 reflection showing the strong contrast of dislocation 8 as well as "the annihilation segment", and absence of dislocation 7.

The mechanism involved in these reactions requires a driving force between the pairs of dislocations. In 4H-SiC, the *c*-component of Burgers vector has magnitude of 10.05Å, almost three times as big as that of the *a*-component at 3.08Å in magnitude. Two closed-core threading dislocations with opposite *c*-component experience a strong attractive force. By calculating the square of Burgers vector magnitude of dislocations before and after reaction, it can be found that the *c*-component annihilation also lower the energy of the dislocation. Although the reactions is favorable in energy, the reaction is hard to conduct via slip which is usually considered to be quite difficult because of the large magnitude of the Burgers vectors and the atomically rough slip planes parallel to the *c*-axis leading to high Peierls stress. On the other hand, many threading dislocations with *c*-component of Burgers vectors are observed to adopt a curved, slightly helical morphology. Such morphologies result in large part from the interaction of a non-equilibrium concentration of vacancies with the screw components of the originally approximately straight dislocation cores behind growth front, which can enable the dislocations from adjacent nucleation sites to respond to their mutual attractive forces and come together and react. Fig. 3.3(a) shows a typical helical morphology of a TSD and when two dislocations like this are close to each other, the interaction between TSDs with opposite signs of Burgers vectors will occur, as shown in Fig. 3.3(b) where some segments annihilate leaving others in the form of trails of stranded loops comprising closed dislocation dipoles.

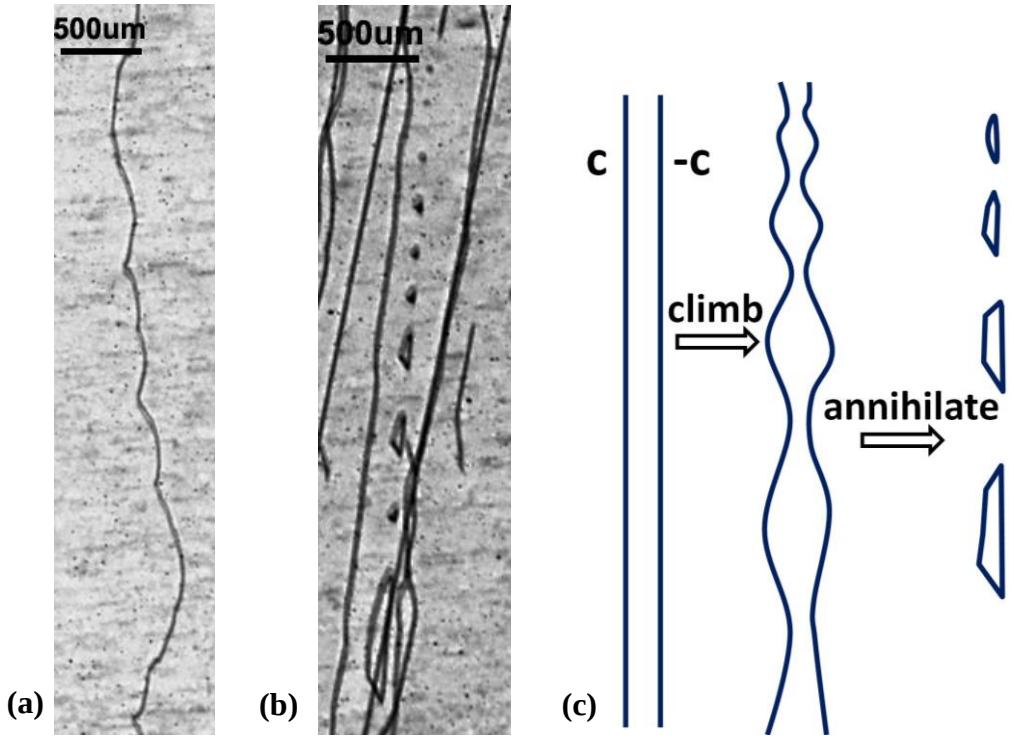

Figure 3.3 (a) SWBXT image of 0004 reflection showing curved slightly helical morphology of *c* dislocation; (b) 0004 reflection at different region showing annihilation of *c* and *–c* dislocation at some segments leaving others in the form of stranded loops comprising closed dislocation dipoles; (c) illustration of the reaction between *c* and *–c* dislocation.

3.4 Conclusion

Observations of mutual interaction between threading dislocations with *c*-component of Burgers vector have been made using SWBXT. Interaction of a non-equilibrium concentration of vacancies with the *c*-component of Burgers vector enable the dislocations to respond to the attractive forces they experience and come together to react. Such interactions can lead to complete or partial Burgers vector annihilation. Among the reactions observed are: (a) the reaction between opposite-sign threading screw dislocations with Burgers vectors **c** and –**c** wherein some segments annihilate leaving others in the form of trails of stranded loops comprising closed dislocation dipoles; (b) the reaction between threading dislocations with Burgers vectors of **-c**+**a** and **c**+**a** wherein the opposite **c**-components annihilate leaving behind the two **a**-components; (c) the similar reaction between threading dislocations with Burgers vectors of **-c** and **c**+**a** leaving behind the **a**-component.

4. Nucleation and Propagation of Threading c+a Dislocations

4.1 Outline

Studies of threading dislocations with Burgers vector of *c+a* have been carried out using synchrotron white beam X-ray topography. The nucleation and propagation of pairs of opposite sign threading c+a dislocations is observed. Overgrowth of inclusions by growth steps leads to lattice closure failure and the stresses associated with this can be relaxed by the nucleation of opposite sign pairs of dislocations with Burgers vector *c+a*. Once these dislocations are nucleated they propagate along the c-axis growth direction, or can be deflected onto the basal plane by overgrowth of macrosteps. For the c+a dislocations, partial deflection can occasionally occur, e.g. the a-component deflects onto basal plane while the c-component continuously propagates along the growth direction. One factor controlling the details of these deflection processes is suggested to be related to the ratio between the height of the overgrowing macrostep and that of the surface spiral hillock associated with the threading growth dislocations with c-component of Burgers vector.

4.2 Introduction

Recently, an increased emphasis has been placed on the impact of threading screw dislocations (TSDs) on the performance of 4H-SiC power devices, as the density of micropipes, formerly the most significant defect in SiC, shrank to practically zero [14]. In view of the fact that TSDs can also cause detrimental effect [80], the development of strategies to minimize their density is a key step for next stage of bulk crystal growth. However, the successful development of such strategies relies on acquiring a proper understanding of the properties of these kinds of dislocation. Latest reports have shown that such threading dislocations are not restricted to those of pure screw character but can comprise all dislocations with c-component of Burgers vector, i.e. with $b= n_1c+n_2a$, where $n_1=1$, $n_2=1$ or 2 [82-84]. Observation of threading dislocations with Burgers vector c+a was reported in the previous chapter and their contrast behavior was compared with that of TSDs, which enables the determination of their Burgers vector. In this continuing work, the nucleation and propagation of threading c+a dislocations is observed and carefully analyzed using synchrotron white beam X-ray topography (SWBXT). Wafers cut parallel to the growth axis from 4H-SiC boules grown using physical vapor transport (PVT) are studied.

4.3 Results and Discussion

Fig. 4.1(a) shows a pair of c+a dislocations nucleate from an inclusion at the left corner of the image, whose contrast is composed of two lobes, one of white and the other of dark contrast [76]. This is consistent with an approximately spherical strain field of the kind associated with an inclusion. Since the dark lobe is on the negative side of the g-vector, one can discern that the inclusion is putting the lattice surrounding it under tension (i.e. the inclusion is smaller than the hole occupied by it in the lattice). The nature of inclusion was not yet explicitly determined.

In order to satisfy Burgers vector conservation, these two dislocations originating from an isolated inclusion inside a perfect crystal region must have opposite sense of Burgers vector.

This is supported by Fig. 4.1(b) that shows a section topograph, which is sensitive to the sense of the dislocation, shown overlapped onto a 0004 projection topograph. Arrows point to the contrast from dislocation 1 and 2 in the section topograph. From the sense of the mutual shift between the bimodal image components, it can be seen that dislocation 1 has right-handed screw component while dislocation 2 has left-handed which confirms that dislocations 1 and 2 have opposite c-components.

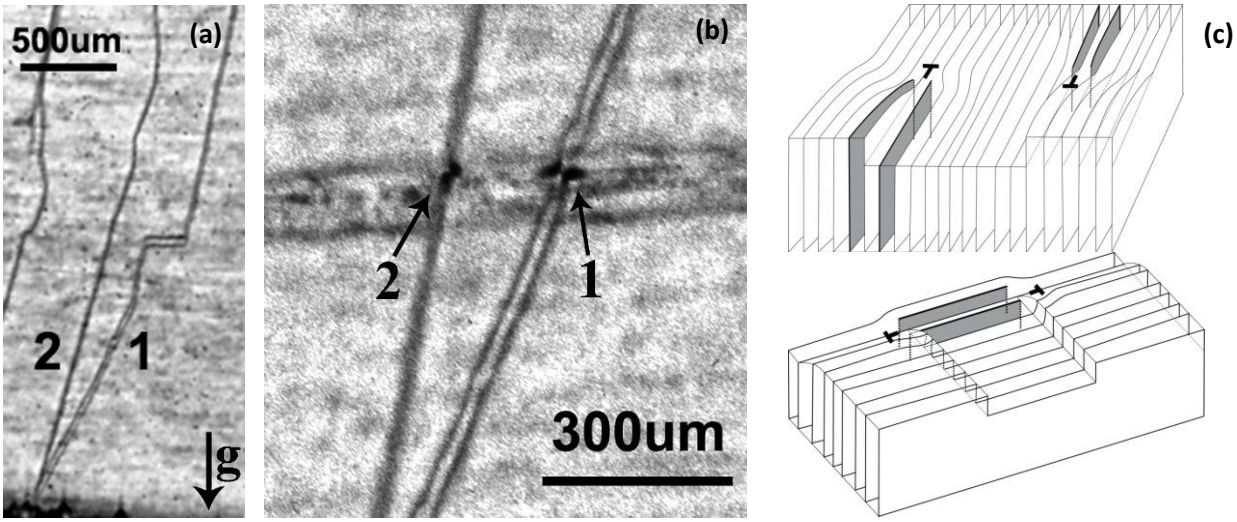

Figure 4.1 (a) SWBXT transmission image of 0004 reflection; (b) a section topograph superimposed on a projection topograph revealing the sense of the opposite sign dislocation pairs. (c) Two possible configurations of the opposite sign c+a dislocations being nucleated

A mechanism for nucleation of screw dislocation pairs with pure c-component at an inclusion was previously presented in detail [35]. In this model, overgrowth of an inclusion during step flow crystal growth created a closure failure which was accommodated by the nucleation of the opposite sign pair of screw dislocations. Similar approach can be adopted here on c+a dislocations. When an inclusion is overgrown by growth steps on the growth face, lattice deformation of opposite sense might occur. By realizing that the magnitude of such deformation depends on the size of the inclusion and the height of growth steps, it becomes possible that dislocations of opposite sense are created to accommodate the misalignment that has magnitude equal to $c+a$. Two possible surface configurations at the growth front after the generation of the opposite sign pairs are shown Fig. 4.1(c). Two extra half-planes are associated with a-component of c+a dislocations and the surface outcrop at the dislocation core is associated with c-component of the dislocations.

From our observation, all threading dislocations with c-component of Burgers vector are growth dislocation, which replicate as growth proceeds, since they are typically very long (up to several centimeters in length) and oriented approximately along the growth direction. However, it is also observed that many such dislocations abruptly change their line direction as they propagate, as for example shown for the case of the two dislocations marked by arrows in Fig 4.2. The deflected dislocation can be redirected back into the threading orientation, as the dislocation marked by black arrows behaves in Fig 4.2(b).

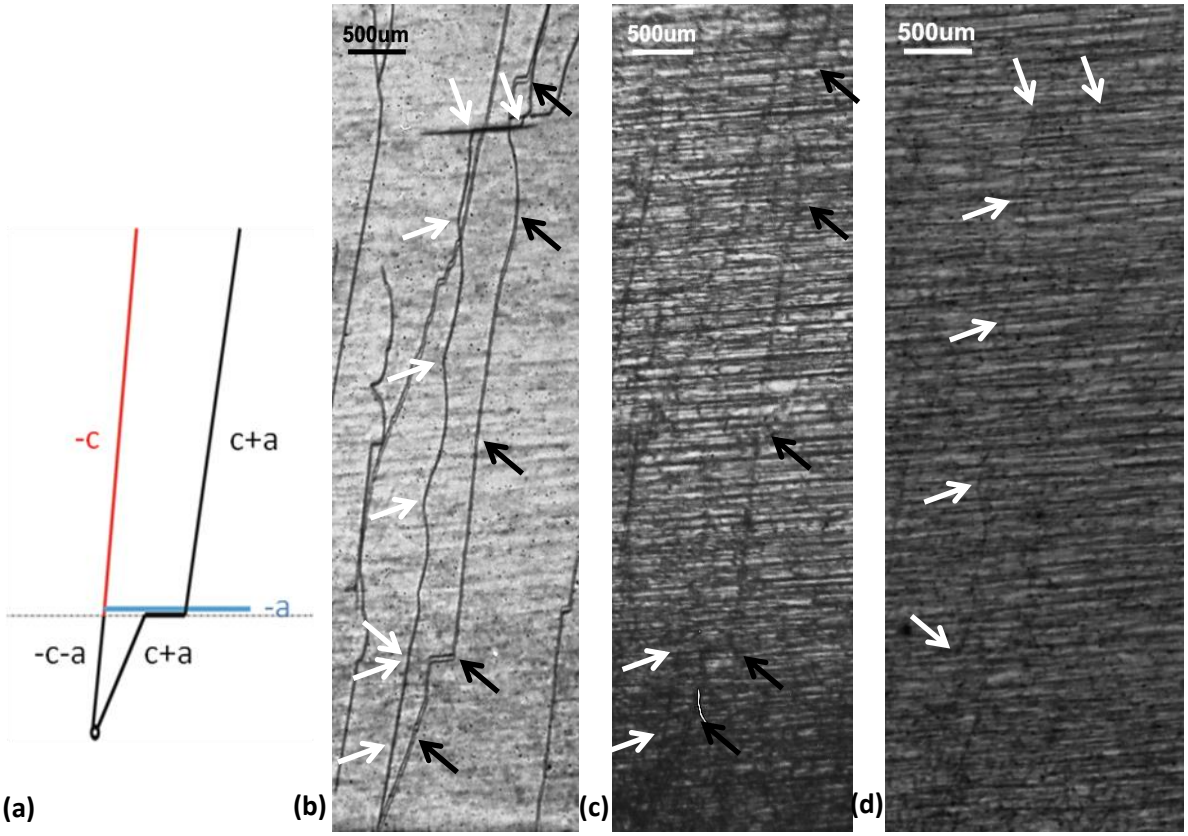

Figure 4.2 (a) Illustration of partial deflection of threading c+a dislocations shown in (b)-(d); (b) 0004 reflection shows a pair of opposite-sign threading c+a dislocations as well as a segment of pure screw dislocation; (c) 01-10 reflection shows contrast from the segments of –c-a dislocation marked by white arrows and c+a dislocations marked by black arrows; (d) 01-11 reflection shows contrast from the segment of pure screw dislocation marked by white arrows

Occasionally, partial deflection of c+a dislocation is observed, in which a-component of c+a dislocation deflects onto basal plane and c-component continues growing along the growth direction; as a result, c+a dislocation diverges into a BPD with $b=a$ and a TSD with $b=c$, as in the case schematically shown in Fig. 4.2(a). Fig. 4.2(a) illustrates the situation in Fig. 4.2(b)-(d), where the pair of opposite sign c+a dislocations described above prorogates along growth direction, and later at some level, a-component of the dislocation on the left is deflected onto the basal plane and the c-component continues to propagate while the c+a dislocation on the right is completely deflected onto the basal plane and later redirected back into the growth direction. In Fig. 4.2(b), the complete morphology of the opposite sign dislocations is in contrast. White arrows point to the –c-a dislocation and black arrows point to the c+a dislocation. The dislocation marked by black arrows shows contrast in 01-10 reflection in Fig. 4.2(c) and is out of contrast in 01-11 reflection in Fig. 4.2(d), which confirms that it has burgers vector of $c+a$ type, in this particular case to be 1/3[-1-123]. It should be mentioned that the background of Fig. 4.2(c) and (d) are somewhat obscured contrast from basal plane dislocations which are out of contrast in Fig. 4.2(b). The contrast from basal dislocation makes the c+a dislocation difficult to see but it is still distinguishable and their identification can by confirmed by the curvature of the

dislocation lines. Part of dislocation marked by white arrows is in contrast in 01-10 reflection and out of contrast in 01-11 reflection and its Burgers vector can be determined to be 1/3[11-2-3], i.e. *–c-a*. The remaining part of this dislocation behaves in the opposite way, and as a result the Burgers vector can be determined to be [000-1], *c* type.

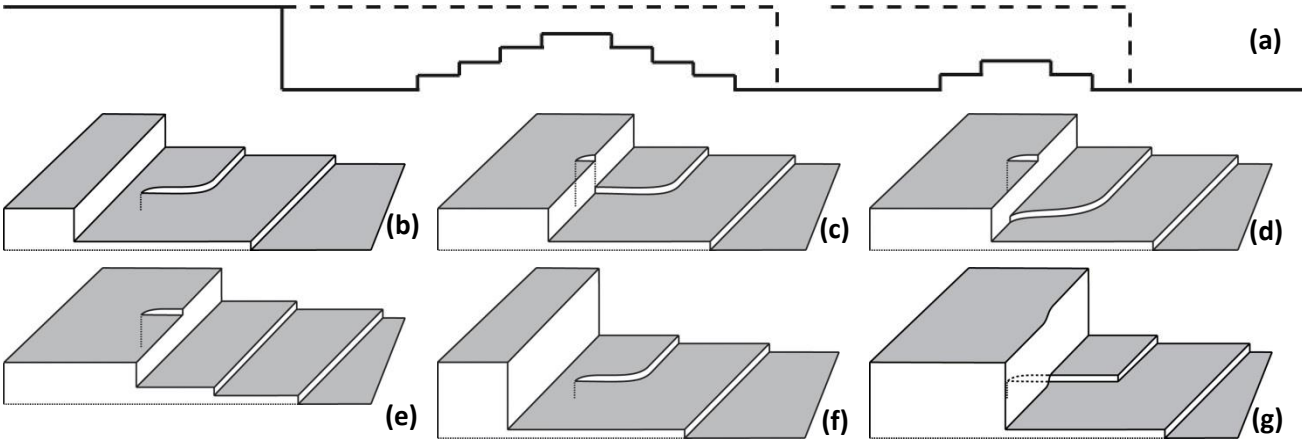

Figure 4.3 (a) Schematic diagram of the surface morphology of growth front containing a pair of dislocations with c-component and a macrostep; (b-e) diagrams showing the step movement when the height difference between macrostep and growth hillock is small; (f-g) the step movement when the height difference between macrostep and growth hillock is big

The deflection process is postulated here to be strongly related to the advancement of macrosteps. The process is schematically shown in Fig. 4.3. Fig. 4.3(a) shows that two growth hillocks are formed at the growth front associated with the c-component of the two dislocations nucleated at the inclusion. It is supposed that the left hillock is better developed than the right one and thus is higher. A macrostep is advancing and will meet the two growth hillocks. The dashed lines indicate two positions the macrostep will reach. It can be noticed that the height difference between macrostep and the left hillock is smaller than that between macrostep and the right one. This height difference can cause behavior differences when the macrostep meets the two hillocks. Fig. 4.3(b)-(e) illustrate the situation when the height difference is small. When macropipe is approaching the growth spiral associated the c-component of the dislocation, it splits at the dislocation core and the growth spiral is reproduced on top of the macrostep, as shown in Fig. 4.3(c). At the molecular level, this process occurs by the arrival of molecular species adsorbed onto the terrace exhibiting the growth spiral and the macrostep splits as it advances enabling it to follow the existing morphology of growth spiral.

In case when the height difference between macrostep and growth hillock is large, the macrostep will simply overgrow the growth spiral without any slip process, as shown in Fig. 4.3(f)&(g). At the molecular level, this process achieves by arrival atoms adsorbed to the macrostep maintaining the integrity of atomic lattice of the macrostep albeit elastically deformed. As a result, the dislocation is deflected. As for the a-component, there is no surface outcrop associated with it. Therefore, the half planes associated with the a-component end when macrostep arrives and the a-component of the dislocations will get deflected in both cases above. The critical height of a macrostep required to cause the deflection of the c-component has not yet been determined but it is of great interest since such deflection processes generally lead to the

exit of the threading dislocations through the crystal sidewalls, which will provide a potential way to lower the dislocation density.

4.4 Conclusion

The nucleation and propagation of pairs of opposite sign threading c+a dislocations is observed using SWBXT techniques. The nucleation of opposite sign pairs of dislocations with Burgers vector c+a is attributed to the overgrowth of inclusions by growth steps, leading to lattice closure failure. Once these dislocations are nucleated they propagate along the c-axis growth direction, or can be deflected onto the basal plane by overgrowth of macrosteps. For the c+a dislocations, partial deflection can occasionally occur, e.g. the a-component deflects onto basal plane while the c-component continuously propagates along the growth direction. One factor controlling the details of these deflection processes is suggested to be related to the ratio between the height of the overgrowing macrostep and that of the surface spiral hillock associated with the threading growth dislocations with c-component of Burgers vector.

5. Simulation of Grazing-Incidence Synchrotron X-Ray Topographic Images of Threading c+a Dislocations

5.1 Outline

Synchrotron monochromatic beam x-ray topography (SMBXT) has been performed on the 4° off-cut 4H-SiC basal wafers at grazing incidence geometry. Reflections of three 11-28 types have been successfully recorded having various contrast from c+a dislocations. Ray tracing simulation has been implemented to determine the Burgers vector of these c+a dislocations.

5.2 Introduction

In Chapter 3, synchrotron white beam x-ray topography studies on axial slices cut from 4H-SiC PVT-grown boules unambiguously proved the existence of threading dislocations with Burgers vector of c+a. However, cutting such axial slices while good for research purposes is not economical as it is destructive to the boule. Recently we also reported observations carried out on commercial offcut (0001) wafers of complex stacking faults with fault vectors such as s+c/2 and s+c/4 which was interpreted as indirect evidence for the existence of threading dislocations with Burgers vector of c+a [82-84]. The formation mechanism of these faults involved the deflection of threading c+a dislocations onto the basal plane. For those threading c+a dislocations that go through the wafer, interaction with the surface must exist and evidence to reveal the character must exist if suitable characterization technique can be used. Etching is widely used to characterize the defects in SiC crystals, but no evidence to date has been found to support the existence of threading c+a dislocations. This may simply be due to the fact that the stress field associated with the c-component of Burgers vector is much stronger than that of a-component so that the etching associated with the c-component may mask that of the a-component. On the other hand, synchrotron x-ray topography, which has much higher resolution than traditional x-ray topography, is sensitive to the detailed stress field associated with defects. Back reflection and grazing incidence geometries are frequently used to examine threading dislocations and the contrast behavior can be interpreted by comparison with detailed image simulation. Amongst the various simulation techniques, the ray tracing method, which was developed in our group, provides a straightforward way of simulating defect images. This technique has been successfully used to simulate many different kinds of defects in SiC. For example, Chen et al. were able to determine the sense of micropipes and TSDs via grazing topography [85]; Kamata et al used the technique to determine the Burgers vector of six different types of threading edge dislocations (TEDs) from grazing topography [86]; and X. Huang et al. also used the technique to determine the signs of basal plane dislocations [87]. In this part of the work, ray-tracing simulation of contrast from threading c+a dislocations in grazing-incidence synchrotron x-ray topograph is carried out and the results are compared with the observed contrast patterns to determine their Burgers vectors.

5.3 Experiment

4H-SiC wafers grown by physical vapor transport technique were used in our study. Grazing-incidence SXRT images of 11-28, -12-18, and 2-1-18 reflections were recorded from Si-faces of the specimens at an x-ray incident angle of 2°, using Agfa Structurix D3-SC film at a specimen-to-film distance of 25–35 cm. The imaging was carried out at the Stony Brook

Synchrotron Topography Station, Beamline X-19C, at the National Synchrotron Light Source at Brookhaven National Laboratory.

5.4 Theory

The ray-tracing method is used to simulate the grazing-incidence topographic images of threading dislocations, and the simulation is carried out using the commercial software Mathematica 8. Orientation contrast and extinction contrast are two main contrast mechanisms associated with the dislocations in x-ray topography. It has been proved that orientation contrast is the dominant one in imaging SiC thick crystal by extensive comparisons between experiment and simulation [88]. In ray-tracing simulation, the specimen surface is divided into small units of constant area. The plane normal of the reflective plane in perfect crystal is defined as $\boldsymbol{n^0}$(x,y,z) and the plane normal $\boldsymbol{n}$(x,y,z) after distortion by dislocation is calculated for each constant area according to the strain field associated with the dislocation. The contrast on the simulated image is determined by the superimposition or separation of beams reflected from individual small areas on the specimen surface. The schematic of simulation based on ray-tracing principle is shown in Fig. 5.1.

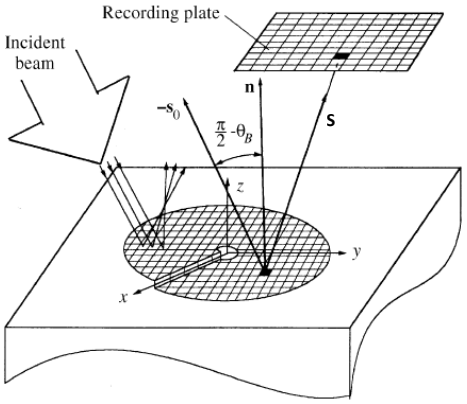

Figure 5.1 Schematic of ray-tracing simulation [9]

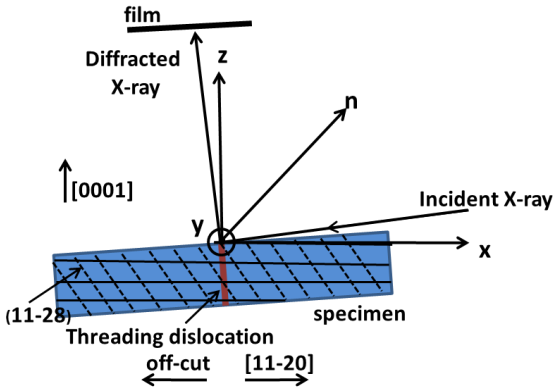

Figure 5.2 Setting of the coordinate system used in simulation

Setting of the rectangular coordinate system used in the simulation is schematically shown in Fig 5.2. The origin is set at the intersection of the specimen surface and the core of threading dislocation. The *z*-axis is chosen to parallel to the ***c***-axis of the specimen, the *x*-axis is chosen along the [11-20] direction (parallel to the off-cut direction), and the y-axis is chosen along [1-100] direction. The x-ray beam parallels to the *xz* plane and is incident at a 2^o angle to the specimen surface. The reflective plane is (11-28) which has a 39.2^o angle to the [11-20] direction.

The plane normal $\boldsymbol{n}$(x,y,z) after distortion due to the strain fields associated with the dislocation is given by [89]

$$\bar{n}(x,y,z) = \bar{n}^{0}(x,y,z) - \nabla[\bar{n}^{0}(x,y,z)\cdot\bar{u}(x,y,z)] \quad \text{.....(6)}$$

where ***u****(x,y,z)* is the displacement field of the dislocation. In order to obtain ***n***(x,y,z), the displacement field ***u*** of threading c+a dislocation should be calculated. It can be considered as the sum of the displacement field of c-component and that of a-component. The c-component of Burgers vectors is parallel to *c*-axis and according to the fundamental dislocation theory the displacement field has only *z-axis* component [60]

$$u_{z1} = \left(\frac{b_1}{2\pi}\right)\cdot \arctan\left(\frac{y}{x}\right) \quad \text{.....(7)}$$

where b_1 is the Burgers vector of c.

According to Eshelby and Stroh [90], the strain components perpendicular to the crystal surface has to be zero in order to satisfy the free surface condition if a screw dislocation is close to the surface. Therefore, an additional displacement in c-plane needs to be taken into consideration in simulation due to such surface relaxation effect. This additional displacement field is given by

$$u_{x1} = u_\theta(x,y,z)\frac{-y}{\sqrt{x^2+y^2}} \quad ;$$

$$u_{y1} = u_\theta(x,y,z)\frac{x}{\sqrt{x^2+y^2}} \quad \text{.....(8)}$$

Where

$$u_\theta(x,y,z) = -\frac{b_1}{2\pi}\sum_{n=0}^{\infty}(-1)^n\{\frac{\sqrt{x^2+y^2}}{(2n+1)t - z + \sqrt{[(2n+1)t-z]^2+(x^2+y^2)}} - \frac{\sqrt{x^2+y^2}}{(2n+1)t + z + \sqrt{[(2n+1)t+z]^2+(x^2+y^2)}}\} \quad \text{.....(9)}$$

As for the a-component, the Burgers vector can be at angle θ to the x-axis. A new coordinate system x'y'z is set in such way that the x'-axis is parallel to the Burgers vector direction, y'-axis is pointing toward the extra half plane associated with the a-component, and z-axis remains the same, as shown in Fig. 5.3.

The displacement associated with the a-component is given by [60]:

$$u_x' = \frac{b_2}{2\pi}[\tan^{-1}\frac{y'}{x'} + \frac{x'y'}{2(1-v)(x'^2+y'^2)}]$$

$$u_y' = -\frac{b_2}{2\pi}[\frac{1-2v}{4(1-v)}\ln(x'^2+y'^2) + \frac{x'^2-y'^2}{4(1-v)(x'^2+y'^2)}] \quad \text{.....(10)}$$

$$u_{x2} = \cos\theta u_x' - \sin\theta u_y' \;;$$

$$u_{y2} = \cos\theta u_y' + \sin\theta u_x' \quad \text{.....(11)}$$

Therefore, the displacement field of c+a is

$u_z = u_{z1}$;

$u_x = u_{x1} + u_{x2}$;

$u_y = u_{y1} + u_{y2}$ ……(12)

Substituting eqn. 7 to eqn. 1, the plane normal ***n*** after distortion can be calculated. Once it is known, the diffracted wave vector ***s*** can be calculated based on equation

$\bar{s}^0 \times \bar{n} = -\bar{n} \times \bar{s}$ ……(13)

where s^0 is the wave vector of incidence beam, which is known from the setting of imaging. The dislocation image, which is actually an intensity map of the diffracted beam, on the x-ray film can be simulated by calculating the wave vector of each diffracted beam from each small units of constant area defined on the crystal surface.

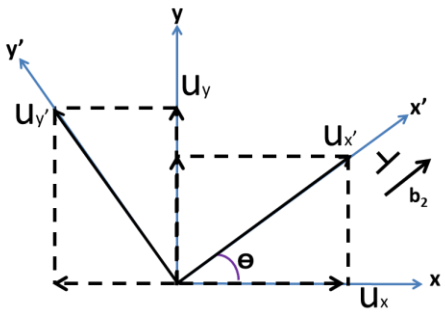

Figure 5.3 Transit coordinate system x'y'z used to calculate the displacement field associated with a-component of Burgers vector

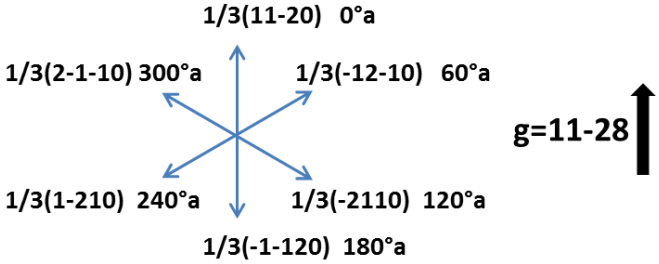

Figure 5.4 Definition of six different a-component of Burgers vector

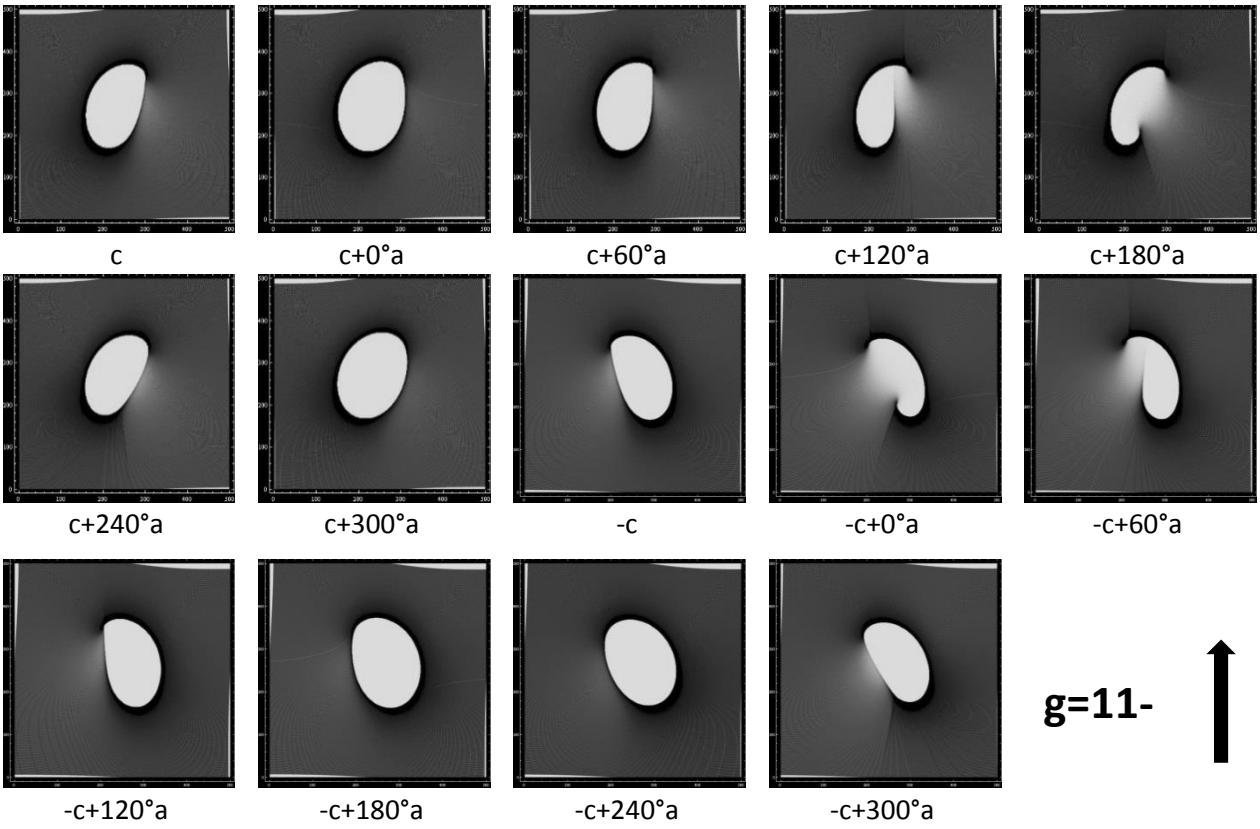

Figure 5.5 Simulation results of the contrast of all 14 threading dislocations with c-component of Burgers vector in 11-28 grazing-incidence topograph. Size of simulation box is 50um×50um.

5.5 Discussion

For threading dislocations with c-component of Burgers vector, there are 14 combinations between opposite sign c-components and six possible a-components. The a-component is defined in such way that 1/3(11-20) is the reference direction, referred to as 0°a which is 0° to the g vector, 1/3(-12-10) is 60°a which is 60° to the g vector, and so on, as shown in Fig. 5.4. Simulation results of the contrast of all 14 threading dislocations with c-component of Burgers vector in 11-28 grazing-incidence topograph are shown in Fig. 5.5. Generally, the contrast pattern contains a white and tilted elliptical spot in the center and a black perimeter surrounding the spot. The contrast pattern can be divided into two groups according to the tilt direction of the ellipse. When the c-component of Burgers vector is positive, the ellipses are tilted to the right; when the c-component of Burgers vector is negative, the ellipses are tilted to the left.

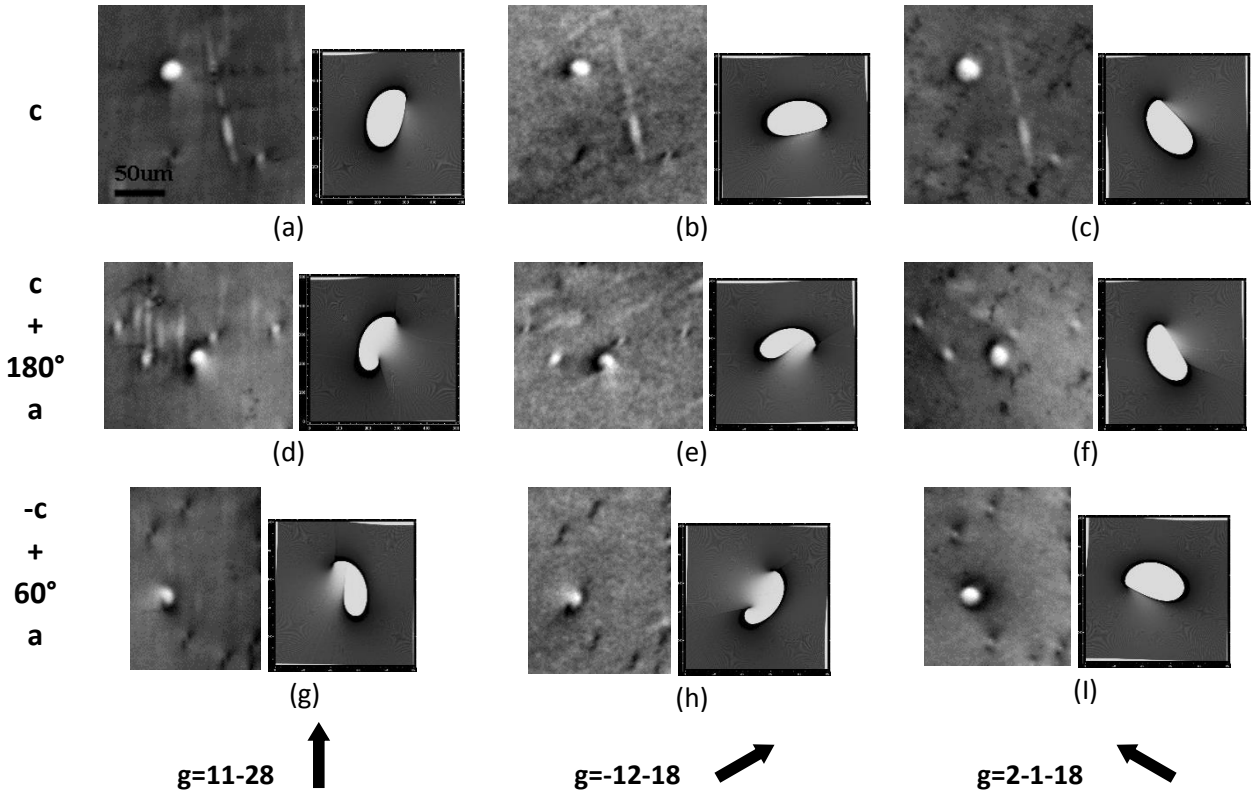

Figure 5.6 Correlation between topography images and simulation results are made for c, c+180°a and –c+60°a. (a) (d) & (g) are 11-28 reflection topographs and related simulation images; (b) (e) & (h) are -12-1-8 reflection topographs and related simulation images; (c) (f) & (I) are 2-1-18 reflection topographs and related simulation images.

Considering the situation when the c-component is positive, compare the contrast pattern of mixed dislocations with c-component and different a-components with that of pure c. The contrast pattern of c+0 °a is more round than that of pure c and the tilt angle decreases. Though these differences can be found when the patterns are compared side by side, it would be difficult to use them to distinguish c+0 °a from pure c on real topographs because a slight change of the shape of the contrast can happen for many reasons, for example, the film may not be exactly parallel to the wafer surface. Similar difficulties exist when comparing c+60 °a, c+240 °a, or c+300 °a with pure c. However, in case of c+120 °a and c+180 °a, the differences between their contrast pattern and those of pure c are obvious: the ellipses become open and black rings become discontinuous and concave, features which can be readily used to identify the c+a dislocation. Similar analysis can be performed when the c-component of threading dislocation is negative.

Correlation between topography images and simulation results are made for c, c+180 °a and –c+60 °a in 11-28 reflection, as shown in Fig. 5.6 (a), (d) & (g). The large features on these images are the contrast features from threading dislocations with c-component of Burgers vector, while the relatively small features originate from TEDs, which have been simulated before [86], and can be used as reference points. In order to further verify the character of these threading dislocations, -12-18 and 2-1-18 grazing-incidence reflection are recorded on the same areas, as

shown in Fig. 5.6. The contrast patterns from the same dislocation vary from reflection to reflection. Simulations for these threading dislocations in different topography geometries are also made and compared side by side with related topography images in Fig. 5.6. As a result, the Burgers vector of these threading dislocations can be determined from studies of commercial wafers.

5.6 Conclusion

Contrast from fourteen different threading dislocations with c-component of Burgers vector has been simulated using ray tracing simulation technique for three different 11-28 reflections of grazing incidence geometry. The contrast from some of the threading c+a dislocations look similar in shape, which makes it difficult to precisely determine their Burgers vectors. After careful comparison of contrast in all three reflections of 11-28 types, it is possible to unambiguously match the simulated images and the real x-ray topographs for at least two kinds of threading c+a dislocations, e.g. c+180 °a, -c+60 °a, which in turn can help to interpret the information gathered from X-ray topography.

6. Nucleation of Stacking Faults with Fault Vectors of 1/6<20-23> from Deflected Threading c+a Dislocations

6.1 Outline

Observations have been made, using Synchrotron White Beam X-ray Topography, of stacking faults in 4H-SiC with fault vectors of kind $1/6\langle 20\bar{2}3\rangle$. A mechanism has been postulated for their formation which involves overgrowth by a macrostep of the surface outcrop of a *c*-axis threading screw dislocation, with two *c*/2-height surface spiral steps, which has several threading dislocations of Burgers vector **c**+**a**, with *c*-height spiral steps, which protrude onto the terrace in between the *c*/2-risers. Such overgrowth processes deflect the threading dislocations onto the basal plane, enabling them to exit the crystal and thereby providing a mechanism to lower their densities.

6.2 Introduction

Three types of stacking fault have been observed to date in SiC: Shockley faults, Frank faults and those which comprise some kind of combination of these two. The presence of Shockley faults is explained by the low Shockley stacking fault energy [38] so that dislocations are dissociated on the basal plane into Si-core and C-core partial dislocations separated by a Shockley stacking fault. Above the brittle to ductile transition temperature (BDTT), the partial pairs move in tandem with partial separations on the order of 30-70 nm [38] whereas below the BDTT C-core partials are sessile so that glide of mobile Si-core partials leads to Shockley fault expansion [39]. Similar stacking fault expansion occurs during the forward bias of *pin* junction diodes where again C-core partials are sessile and Si-core partials glide (driven by recombination) leading to Shockley fault expansion [22]. Frank faults are considered to be "in-grown" stacking faults and are thought to result from the overgrowth of *c*-axis screw dislocations whose surface growth spiral steps were separated into *c*/4, *c*/2, and 3*c*/4 step heights [64]. "So called" 8H faults have been observed by many groups [26, 61] and are also considered to be "in-grown" in nature although no model has been postulated for their formation mechanism. Skowronski et al [65], Chen et al [91] and Tsuchida et al [52] have made observations of stacking faults associated with "Carrot" defects which have fault vectors of $1/12\langle 4\bar{4}03\rangle$ which comprises the sum of a *c*/4 Frank fault with a $1/3\langle 1\bar{1}00\rangle$ Shockley fault. Chen et al [9] postulated that such faults arise from the overgrowth of *c*-axis screw dislocations which have dissociated basal plane dislocations pinned at their cores. Dudley et al [82, 84] recently reported that such faults can arise from the deflection of *c*-axis threading dislocations of Burgers vector **c**+**a** onto the basal plane. If the spiral step risers of such dislocations divide into *c*/4 and 3*c*/4 increments, overgrowth can be facilitated by the simultaneous dragging of one of the Shockley partials associated with the core structure of the original dislocation by the overgrowing macrostep. This acts like an interfacial Shockley partial and adds the Shockley component to the *c*/4 Frank component of fault vector. In this letter we present observations of stacking faults comprising combinations of *c*/2 Frank faults with Shockley faults. We present a model for their formation mechanism which involves the combined deflection, via macrostep overgrowth, of the surface outcrops of threading dislocations with Burgers vectors of **c** and **c**+**a**. These deflection processes provide a mechanism by which the density of threading dislocations in the boules can be lowered.

6.3 Results and Discussion

Figs. 6.1(a)-(c) show a series of Synchrotron White Beam X-ray Topographic (SWBXT) images recorded from a region near the edge of a 76mm wafer cut from a boule grown using Physical Vapor Transport (PVT) under low stress conditions. Two types of stacking fault are present, labeled A and B. Faults A exhibit strong contrast on $\{1\bar{1}00\}$ reflections, weak contrast on $\{01\bar{1}1\}$ reflections, and no contrast on $\{11\bar{2}0\}$ reflections, while faults B exhibit strong contrast on $\{01\bar{1}1\}$ reflections but no contrast on either $\{1\bar{1}00\}$ or $\{11\bar{2}0\}$ reflections. The contrast from stacking faults in X-ray topography arises from the phase shift experienced by the X-ray wavefields as they cross the fault plane [92]. This phase shift has been computed to be equal to $\delta=(-2\pi\,\mathbf{g}.\mathbf{R})$, where **g** is the active reciprocal lattice vector for the reflection and **R** is the fault vector. Contrast is expected to disappear when $\delta=0$ (corresponding to $\mathbf{g}.\mathbf{R}$=integer) and is expected to be very weak when $\delta=\pm\pi/6$ (corresponding to $\mathbf{g}.\mathbf{R}=\pm1/12,\ \pm11/12$) and weak but visible for $\delta=\pm\pi/3$ (corresponding to $\mathbf{g}.\mathbf{R}=\pm1/6,\ \pm5/6$). Contrast should be very well marked for $\delta=\pm\pi$ and $\pm2\pi/3$ (corresponding to $\mathbf{g}.\mathbf{R}=\pm1/2,\ \pm1/3$ and $\pm2/3$).Detailed analysis of the fault contrast on different reflections shows that these observations are consistent with a fault vector, $\mathbf{R}_B$, of $c/2$ for faults B and $c/2$ plus a Shockley displacement for faults A, i.e. $\mathbf{R}_A=1/6<20\bar{2}3>$ (see Table 6).

Table 6 **g·R** values for stacking faults A and B

g·R (R \ g)	$(01\bar{1}0)$	$(0\bar{1}11)$	$(\bar{2}110)$
$\mathbf{R}_A=1/6<20\bar{2}3>$	1/3	1/6	-1
$\mathbf{R}_B=1/2\,[0001]$	0	1/2	0

We postulate that such fault configurations arise from macrostep overgrowth of a *c*-axis threading screw dislocation (TSD) whose spiral step riser has divided into two *c*/2-high demisteps and which has several *c*-axis dislocations of Burgers vector **c**+**a** with *c*-height spiral step risers protruding onto the terrace between the two demisteps. Overgrowth of the this TSD alone would deflect it onto the basal plane creating two *c*/2 Frank partial dislocations (at the locations of the demistep risers) separated by a *c*/2 Frank fault. The simultaneous overgrowth of the threading **c**+**a** dislocations (CPADs) protruding onto the terrace between the demistep risers would deflect them onto the exact same basal plane as the *c*/2 fault (as shown for a single such threading CPAD in Figs. 6.2(a)-(c)).

During this deflection process, the surface termination lines of the two extra half-planes associated with the *a*-component of Burgers vector of the threading CPAD will become the line directions of two Shockley partials associated with the *a*-component of the deflected dislocation while the lines of termination of the four bilayers which constitute the spiral step riser (*c*-component of the threading CPAD) will become the lines of termination of the extra half planes associated with a Frank dislocation which comprises the *c*-component of the deflected dislocation as shown in Figs. 6.2(a)-(c).

Once on the basal plane, it becomes possible that a CPAD can dissociate into its *c* and *a* components since the latter is potentially glissile on the basal plane. Usually, above the brittle to ductile transition, pairs of Shockleys would move in tandem under shear stress (τ). If the stress

drives the partials to the right, as shown schematically in Figs. 6.2(e)–(f), the leading partial converts the tetrahedra protruding onto the glide plane from twinned configuration (primed) into untwinned and the trailing partial reverses this process [93]. However, if the *c*-height step riser associated with the *c*-component of the Burgers vector of this CPAD is oriented so as to bisect the two extra half planes associated with its *a*-component (see Fig. 6.2(a)) when overgrowth occurs, then the surface termination lines of the two extra half-planes will be mutually displaced along the *c*-axis by one unit cell. Since these become the line directions of the two Shockley partials during macrostep overgrowth this means that they are also mutually displaced by the same amount or in other words the cores of the two Shockleys are on two parallel slip planes separated by a unit cell height as shown schematically in Figs. 6.2(b)-(c).

In this case, if the crystal experiences stress with a sense such that the partials are driven towards the right, then the leading partial is on the terrace below the c-height step. This partial converts the tetrahedra protruding onto the glide plane from twinned configuration into untwinned, while the trailing partial is prevented from reversing this process since it encounters a terminating glide plane and so becomes sessile, as shown schematically in Fig. 6.2(g).

For the reverse sense of stress, the partials would be driven towards the left, and the upper partial would be the leading partial which would, for example, convert the tetrahedra protruding into the glide plane from twinned configuration into untwinned. However, the trailing partial would like to reverse this process but the tetrahedra protruding onto its glide plane are already in twinned configuration and so that it also becomes sessile, as shown schematically in Fig. 6.2(h).

Thus, for either sense of stress, the trailing partial is sessile while the leading partial is glissile. Should thermal gradients subsequently experienced by the crystal whilst in the growth chamber generate shear stress on the basal plane, the glissile partial can glide leading to Shockley fault expansion. Since this Shockley glide occurs on the exact same basal plane, the Shockley fault vector will simply combine with the *c*/2 Frank fault vector creating a net fault vector of type $1/6\langle 20\bar{2}3\rangle$, as shown schematically in Fig. 6.2(d).

If there are several CPADs with different *a* components deflected onto the *c*/2 Frank fault terrace by overgrowth of the same macrostep, then glide of the glissile partials can lead to the similar creation of three possible kinds of $1/6\langle 20\bar{2}3\rangle$ faults. For the case observed here, the Burgers vectors of the various partials bounding the faults were determined by contrast extinction analysis, and from this we can infer the Burgers vectors of the original CPADs. The results are shown schematically in Figs. 6.2(i)-(k).

It is also interesting to note that A type faults are typically bounded by a straight partial on one side and a curved partial on the other. This is consistent with the model in that the glissile Shockley is expected to be curved as it glides and gets pinned at various obstacles while the sessile partial is expected to be trapped at the straight c-height step riser associated with the original CPAD. The original outer limit of the B type fault (prior to the glissile Shockley glide) is also expected to be bounded by straight partials corresponding to the straight demistep risers. This again is consistent with observations. The deflection of these threading dislocations evidently provides an efficient mechanism by which their densities can be reduced. When such deflection occurs near the periphery of the boule, the deflected dislocations exit through the side

face of the boule effectively reducing the threading dislocation density in the subsequently grown region of crystal. Further studies of this dislocation reduction process are underway.

6.4 Conclusion

Observations have been made using SWBXT of stacking faults in PVT-grown 4H-SiC with fault vectors of kind 1/6$<20\bar{2}3>$. A mechanism has been postulated for their formation which involves overgrowth by a macrostep of the surface outcrop of a *c*-axis TSD, with two *c*/2-height surface spiral steps, which has several threading CPADs with *c*-height spiral steps which protrude onto the terrace in between the *c*/2 risers. During overgrowth, the *c*/2 step risers give rise to a *c*/2 Frank fault, while the two Shockley partials which result from the overgrowth of the threading CPADs can become separated onto different slip planes such that one becomes mobile and the other sessile. Should the crystal, while still in the growth chamber, subsequently experience shear stress on the basal plane, the mobile partial will move leading to Shockley fault expansion resulting in a local net fault vector of *c*/2 plus a Shockley, i.e. 1/6$<20\bar{2}3>$. Such overgrowth processes deflect the threading dislocations onto the basal plane, enabling them to exit the crystal, effectively reducing the threading dislocation density in the crystal.

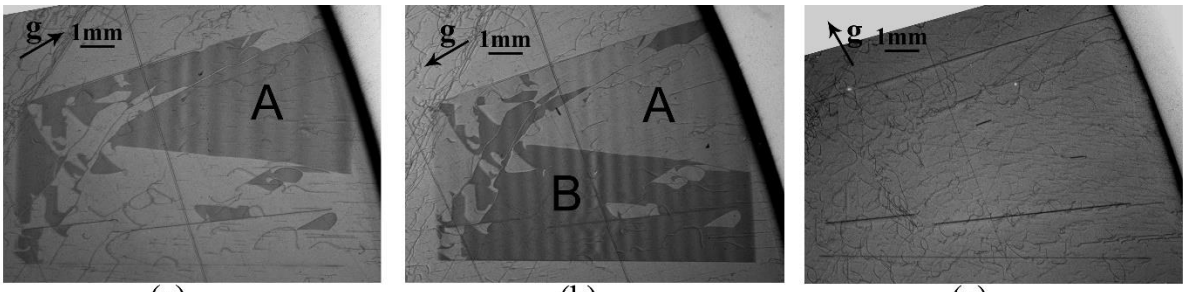

Figure 6.1 SWBXT Images recorded from a region near the edge of a 76mm wafer cut with 4 degrees offcut towards $[11\bar{2}0]$: (a) $01\bar{1}0$ reflection showing stacking fault contrast from fault A only; (b) $0\bar{1}11$ reflection showing strong fault contrast from fault B and weak fault contrast from fault A; (c) $\bar{2}110$ reflection showing absence of all fault contrast.

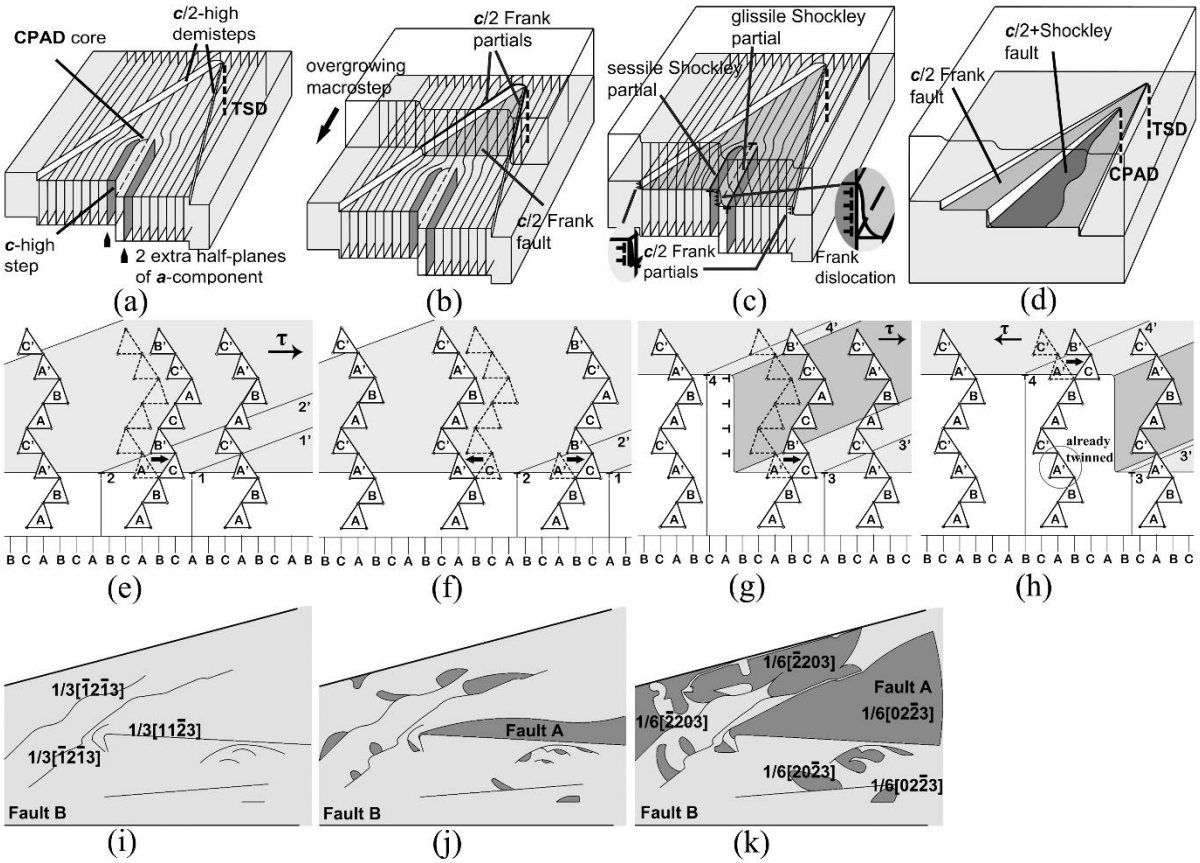

Figure 6.2 (a) Schematic of macrostep overgrowth of the surface outcrop of a TSD with two *c*/2-height surface spiral steps which has a CPAD with a *c*-height spiral step protruding onto the terrace between the two *c*/2-height steps; (b) creation of two *c*/2 Frank partial dislocations separating a *c*/2 Frank fault; (c) overgrowth of the outcrop of the threading CPAD, creating another Frank dislocation and two Shockley partials lying on the basal plane which are on slip planes separated by one unit cell; (d) glide of glissile Shockley under thermal stress leaving a Shockley fault in its wake, giving a net fault vector in this region of *c*/2 plus Shockley; (e) schematic of glide of dissociated basal plane dislocation above the BDTT wherein the two Shockleys move in tandem under stress, with the leading partial 11', for example, converting twinned tetrahedra in the middle column into untwinned (in the middle column, tetrahedra are drawn using dotted lines prior to glide and full lines after); (f) after further glide in, the trailing partial 22' reverses this process; (g) if the two partials are on two parallel slip planes separated by a unit cell height, the leading partial 33' is glissile and converts twinned tetrahedra into untwinned while the trailing partial 44' is sessile because it encounters a terminating glide plane; (h) for the reverse sense of stress, the leading partial 44' is glissile and converts twinned tetrahedra into untwinned while the trailing partial 33' (which would normally convert untwinned tetrahedra into twinned) is sessile because the tetrahedra on its glide plane are already twinned. (i)-(k) Expansion of different 1/6< $20\bar{2}3$ > faults from overgrowth of several CPADs with different *a*-components (as indicated by the original CPAD Burgers vectors) which protruded onto the terrace between the two *c*/2 spiral steps.

7. Direct Observation of Stacking Fault Nucleation from Deflected Threading c+a Dislocations

7.1 Outline

In our previous studies [82-84], four kinds of stacking faults in 4H-SiC bulk crystal have been distinguished based on their contrast behavior differences in synchrotron white beam x-ray topography images. These faults are Shockley faults, Frank faults, Shockley plus c/2 Frank faults, and Shockley plus c/4 Frank faults. Our proposed formation mechanisms for these stacking faults involve the overgrowth of the surface outcrop associated with threading screw dislocations (TSDs) or threading mixed dislocations (TMDs) with Burgers vector of c+a by macrosteps and the consequent deflection of TSDs or TMDs onto the basal plane. Previous synchrotron x-ray topography observations were made in offcut basal wafers using transmission geometry. In this part of the work, further evidence is reported to confirm the proposed stacking fault formation mechanism. Observations are made in axially cut slices with surface plane {11-20}. Several kinds of stacking faults are recognized and their contrast behavior agrees with the four kinds previously reported. Direct observation is obtained of a Shockley plus c/4 Frank stacking fault nucleating from a TMD deflected onto the basal plane. The contrast from stacking faults on the basal plane in the axial slices is enhanced by recording images after rotating the crystal about the active -1010 reflection vector enabling a broader projection of the basal plane.

7.2 Introduction

High quality 4H-SiC crystals are required to make substrate wafers and are currently grown using physical vapor transport technique (PVT). In the past decade, defect densities in 4H-SiC have been dramatically reduced. For example, micropipes have been practically eliminated [14], while TSD and BPD densities have decreased by orders of magnitude down to several hundred and several thousand per square centimeter respectively. Stacking faults in the substrates have gained some attention recently and in our previous work four kinds of stacking faults have been reported in terms of their fault vectors, e.g. Shockley faults, Frank faults, Shockley plus c/2 Frank faults, and Shockley plus c/4 Frank faults [82-84]. Generally speaking, defects reaching the growth surface will extend into the epi layer and may potentially harm the performance of devices grown on it. Understanding the formation mechanism of stacking faults may lead us to a potential strategy to eliminate this category of defects.

7.3 Experiment

PVT grown 4H-SiC crystals are studied using both synchrotron white beam x-ray topography (SWBXT) and synchrotron monochromatic beam x-ray topography (SMBXT). Axially cut slices with surface plane of {11-20} type are imaged using transmission geometry: {0004} reflections are recorded to study the contrast behavior of TSDs and TMDs, {1-100} and {1-101} reflections 20° tilted about reflection vector g are recorded to study the contrast behavior of stacking faults. Fig. 7.1 (a) and (b) show the difference between regular (-1010) reflection and tilted (-1010) reflection in setting geometry and also in the information collected on the film. For the regular (-1010) reflection, with the incident beam parallel to the (0001) plane upon which the stacking fault sits, the projected image of the stacking fault on the film would be

a straight line. When the sample is tilted about the g vector, the stacking fault will show area contrast thus allowing contrast analysis to be conducted.

Offcut basal wafers with surface plane of (0001) are studied using both SWBXT and SMBXT in grazing geometry. Ray tracing simulation has been carried out for contrast from defects in the SMBXT images. The simulation is based on orientation contrast [88] and is carried out using the commercial software Mathematica 8.

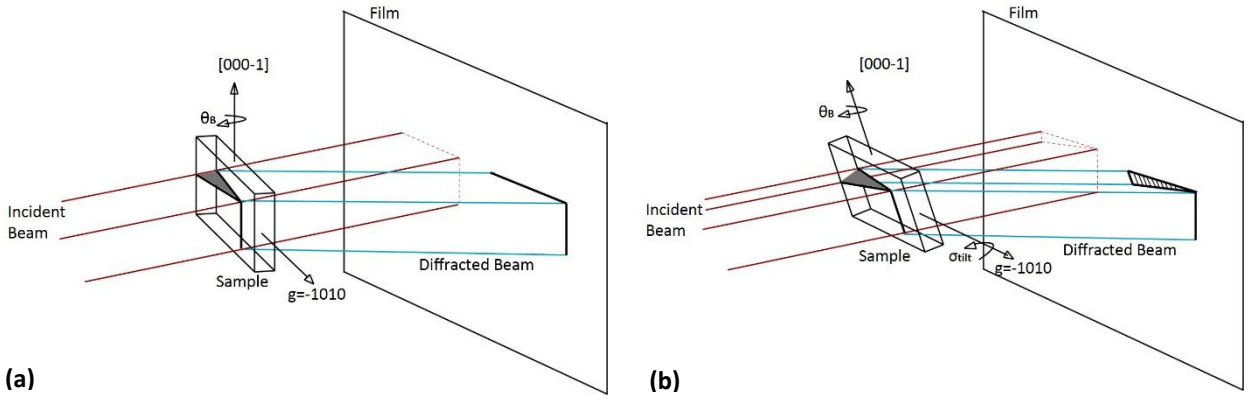

Figure 7.1 (a) Regular setting geometry of transmission SWBXT of -1010 reflection; (b) setting geometry of the same reflection but with the sample tilted about g vector

7.4 Results and discussion

Four types of stacking faults have been distinguished in our previous study on offcut basal wafers and based on their difference in Burgers vector, they could be Shockley faults with fault vector 1/3<1-100>, Frank faults with fault vector ½<0001>, Shockley plus c/2 Frank faults with fault vector of 1/6<2-203>, or Shockley plus c/4 Frank faults with fault vector of 1/12<4-403> [82-84]. The same types of stacking faults are observed on the topography images recorded from axially cut slices as shown in Fig. 7.2, and their fault vectors can be determined using the g ŀR criterion, where g corresponds to the reflection vector and R corresponds to the fault vector. Contrast from stacking faults is expected to disappear when g ŀR is equal to an integer (including zero) and is expected to be very weak (almost invisible) when g ŀR equals to ±1/12 or ±11/12. Contrast should be weak but visible when g ŀR equals to ±1/6 or ±5/6 and well-marked when g ŀR equals to ±1/2, ±1/3, or ±2/3. Stacking faults are numbered from 1 to 6 on the images and the g ŀR calculation is summarized in Table 7.

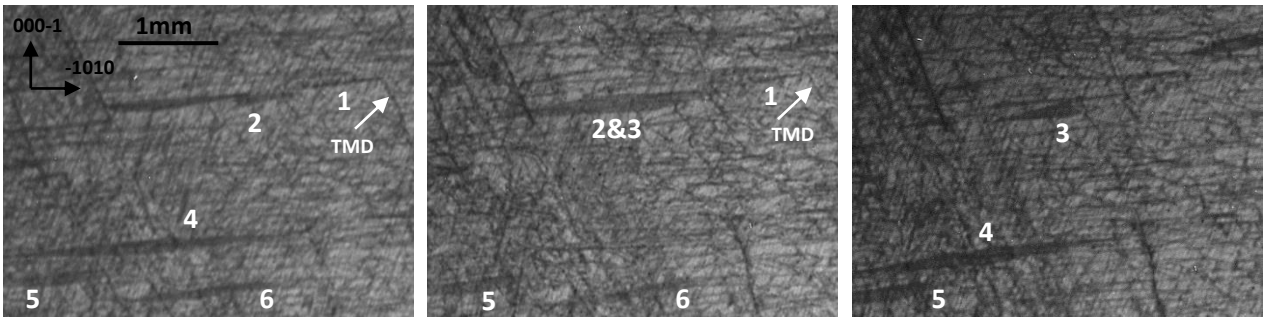

(a) g=10-1-1 (b) g=10-10 (c) g=10-11

Figure 7.2 SWBXT images of (a)10-1-1 reflection, 20° tilted about g vector, (b) 10-10 reflection, 20° tilted about g vector, (c) 10-11 reflection, 20° tilted about g vector, recorded from the same region containing stacking faults 1 to 6 in a axially cut 4H-SiC slice

In our postulated stacking fault formation mechanism, stacking faults arise from the deflection of threading dislocations with c-component of Burgers vector onto the basal plane. It is therefore expected that there should be a TSD or TMD connecting to the nucleation point of the stacking fault. However, depending on where the axial slice intersects the stacking fault, their nucleation point may or may not be included in the limited volume of the sample. In Fig. 7.2(a) in addition to the area contrast from stacking faults, line contrast from dislocations is evident in the background, and stacking fault 1 can be clearly seen to connect with a threading dislocation. Through contrast analysis (contrast from dislocations is weak when $\mathbf{g}\cdot\mathbf{b}=0$), this threading dislocation is determined to be a TMD with Burgers vector 1/3<-2113>, as summarized in Table 7.

Table 7 g·R calculation for stacking faults 1 to 6 and g·b calculation for TMD segment AB

g·R / R / g	R=1/12<-4403> (SF #1, 2, 6)	R=1/12<4-403> (SF #3)	R=1/2<0001> (SF #4)	R=1/3<1-100> (SF #5)	b=1/3<-2113> (TMD segment AB)
g=10-1-1	-7/12	1/12	-1/2	1/3	-2
g=10-10	-4/12	4/12	0	1/3	-1
g=10-11	-1/12	7/12	1/2	1/3	0

Fig. 7.3(a) shows an enlarged image of the region containing stacking fault #1 of 10-1-1 reflection (20 ° titled about g vector). TMD segment AB aligns roughly along the growth direction and is deflected into basal plane at point B, from which stacking fault #1 nucleates. 0004 reflection in Fig. 7.3(b) gives better resolution to threading dislocations with c-component of Burgers vector, since BPDs ($\mathbf{g}\cdot\mathbf{b}=0$) and TEDs ($\mathbf{g}\cdot\mathbf{b}=0$ and $\mathbf{g}\cdot\mathbf{b}\times\mathbf{l}=0$) are out of contrast. Connecting to point B in Fig. 7.3(b), the stacking fault is projected onto the film without a tilt angle to become a line and the line contrast is actually from the partial dislocations associated with the stacking faults. Notice that TMD segment CDEF also is deflected into basal plane at pint D, but redirected back to threading orientation at point E. No area contrast from stacking

faults is observed between points E and D in Fig. 7.3(a), which suggests TMD segment CDEF remains as single dislocation during the whole deflection and reorientation process. Therefore, a good comparison can be built between line contrast from a deflected TMD segment DE and the area contrast from stacking fault #1.

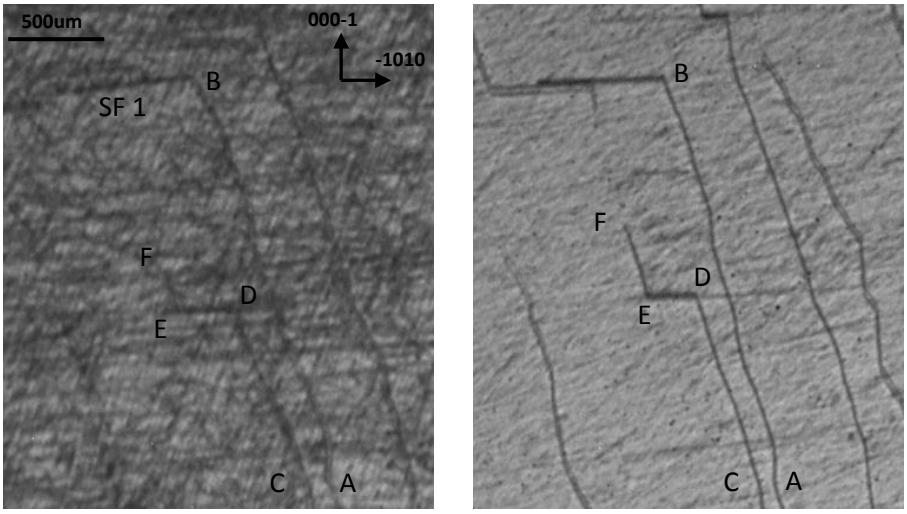

(a) g=10-1-1 (b) g=0004

Figure 7.3 SWBXT images showing stacking fault #1 nucleating from the deflection point B of TMD segment AB: (a) 10-1-1 reflection, 20° tilted about g vector, (b) 0004 reflection

Evidence to support the stacking fault formation mechanism can also be found on grazing incidence x-ray topography images recorded from offcut basal wafers with surface plane of (0001). Fig. 7.4(a) is a transmission x-ray topography image featuring a stacking fault which shows dark area contrast of triangular shape. The black circle on the image marks the nucleation point of the stacking fault. Fig. 7.4(b) is the grazing incidence x-ray topography image recorded from the Si face at the same region with a penetration depth of 49um, showing contrast from defects close to the sample surface. Inside the black circle in Fig. 7.4(b) which marks the corresponding position of the other one in Fig. 7.4(a), contrast from a threading dislocation with c-component of Burgers vector is observed as a back dot, which corresponds to the intersection point where the threading dislocation hits the surface. Since the 4H-SiC crystal is grown on c face by PVT, one can build the model that this threading dislocation propagates along the [000-1] direction (into this paper surface) and then deflects onto the basal plane, nucleating stacking faults during the crystal growth.

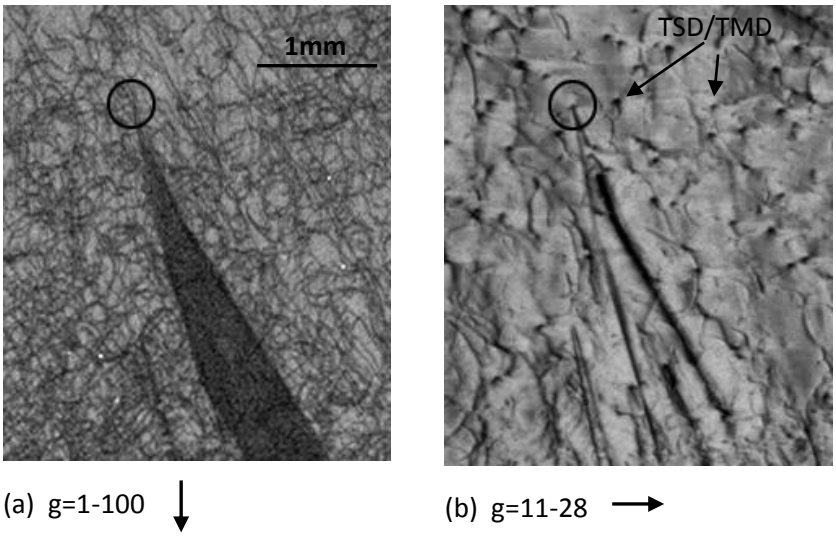

Figure 7.4 SWBXT images of (a) transmission 1-100 reflection, (b) grazing 11-28 reflection, recorded from the same region have a stacking fault in a offcut basal wafer

Figure 7.5 Ray tracing simulation the contrast from deflected TMDs in grazing incidence SMBXT images of 11-28 reflection, box size 50um × 50um

Fig. 7.5 shows a series of images of ray tracing simulation of the contrast from deflected TMDs in grazing incidence SMBXT images of 11-28 reflection. The contrast is mainly composed of a black line and a white gap on one side of the back line. When the sign of c-component of Burgers vector opposites, the white gap switches to the other side of the back line, as what happens changing from Fig. 7.5(a) to Fig 7.5(b) or from Fig 7.5(c) to Fig 7.5(d). When the sign of a-component of Burgers vector opposites, the width of white gap changes, as what happens changing from Fig 7.5(a) to Fig 7.5(c) or from Fig 7.5(b) to Fig 7.5(d); however, this width change could be subtle to notice on the actual topography image. Therefore, by comparing the relative position of the black and white contrast, the sign of c-component of Burgers vector of TMDs can be determined. This method also applies to determining the sign of c-component of the two partial dislocations associated with stacking faults, which could have smaller magnitude of both c-component and a-component than TMDs. The actual SMBXT images of 11-28 grazing incidence are shown in Fig. 7.6. The black circle in Fig. 7.6(a) marks a single deflected TMD as an example to show the blank and white contrast and the sign of c-component of Burgers vector is determined to be positive. The white line contrast in the background of the image is from surface scratches, which contribute to the noises that decrease the topography resolution. The black circle in Fig. 7.6(b) marks a pair of partial dislocations associated with stacking faults.

Since the white gaps are on the same side of the black lines, two partial dislocations are determined to have the same sign of the c-component of Burgers vector. This result also support the postulated stacking fault formation mechanism, because according the conservation law of Burgers vector, the partial dislocations split from a deflected threading dislocation should have the same sign of c-component of Burgers vector as the original threading dislocation has.

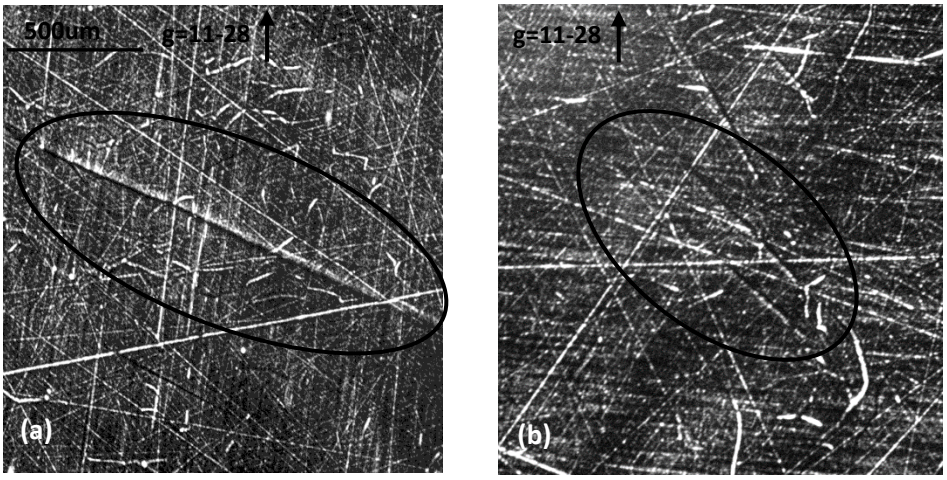

Figure 7.6 Grazing incidence SMBXT image of 11-28 reflection: (a) a single deflected TMD, (b) two partial dislocations associated with a stacking fault

7.5 Conclusion

As part of ongoing work to support our proposed stacking fault formation mechanism via deflection of threading dislocations with c-component of Burgers vector in PVT grown 4H-SiC crystals, SWBXT and SMBXT studies have been carried on both offcut basal wafers and axially cut slices. Contrast from three kinds of stacking faults has been recorded from axially cut slices. Based on their contrast behavior differences in the SWBXT images, their fault vectors are determined to be Shockley type, Frank type, and Shockley plus c/4 Frank type. Direct observation is obtained of Shockley plus c/4 Frank stacking faults nucleating from a deflected TMD with Burgers vector of c+a on the basal plane. The contrast from stacking faults on the basal plane in the axial slice is enhanced by recording images after rotating the crystal about the active -1010 reflection vector enabling a broader projection of the basal plane. According to ray tracing simulation results of the contrast from deflected TMDs in SMBXT images, the two partial dislocations associated with stacking faults are determined to have Burgers vectors which exhibit the same sign in their c-components.

8. Formation of Six-Pointed-Star shaped Stacking Faults in PVT grown 4H-SiC

8.1 Outline

Synchrotron white beam x-ray topography (SWBXT) studies are presented of defects in one hundred millimeter diameter, 4H-SiC wafers grown using physical vapor transport (PVT). SWBXT enables non-destructive examination of thick and large-diameter SiC wafers and defects can be imaged directly. Analysis of the contrast from these defects enables determination of their configuration which, in turn, provides insight into their possible formation mechanisms. Apart from the usual defects present in the wafers, including micropipes, threading edge dislocations, threading screw dislocations and basal plane dislocations, a new stacking fault with a peculiar configuration attracts our interest. This fault has a shape of a six-pointed star comprising faults with three different fault vectors of the Shockley type. Transmission and grazing topography is carried out of the fault area and detailed contrast analysis reveals that the outline of the star is confined by 30-degree Shockley partial dislocations. A micropipe, which became the source of dislocations on both the basal-plane slip system and the prismatic slip system, is found to be associated with the formation of the star fault. The postulated mechanism involves the reaction of 60-degree dislocations of $a/3<\bar{2}110>$ Burgers vector on basal plane and pure screw dislocations of $a/3<11\bar{2}0>$ Burgers vector on prismatic plane and cross slip of the partial dislocation from prismatic plane to basal plane leading to the expansion of the faults.

8.2 Introduction

Intense effort is currently in progress to study and eventually eliminate various defects in SiC in order to improve and stabilize the performance of SiC-based power devices. An active area of research is the origin and expansion of stacking faults in SiC. Although named differently from group to group, three types of stacking faults according to their fault vectors have been reported: Shockley fault with fault vector of $a/3<1\bar{1}00>$ type [22, 39, 84], Frank fault with fault vector of (c/2)[0001] or (c/4)[0001] [64], and those comprising some kind of combination of the previous two [52, 65, 82, 83, 91].

Among these faults Shockley fault has been shown to be associated with the degradation of power devices, as the expansion of the fault in the junction area can impede current flow and, as a result, increase the on-state resistance [22]. In the epilayer, the morphology of the Shockley faults responsible for the device degradation is found to have a rhombus shape with the sides along $<11\bar{2}0>$ directions and angles of $60°$ and $120°$, bounded by $30°$ partial dislocation loops. The fault expands though a mechanism whereby the Si-core partials are electrically active, while the C-core partials are not, and the Si-core partials can couple with electron-hole recombination and move.

In SiC, Shockley faults can also form in response to the applied stresses in the crystal. Above the brittle to ductile transition temperature (BDT), Shockley faults separate the Si-core and C-core partial dislocations that move in tandem but with separation on the order of 30-70 nm. Below the BDT, C-core partial becomes sessile and thus the Shockley fault can expand as the mobile Si-core partial glides [39]. Another mechanism of the fault expansion in SiC crystals is related to existence of threading dislocations with Burgers vectors of c+a [82-84]. It is postulated that two partials associated with the a-component of the dislocation are separated by the surface

step associated with c-component of the deflected c+a dislocation causing one to be sessile and the other glissile. The Shockley fault created by deflection of c+a dislocation is observed to be bounded by a straight sessile partial on one side and a curved glissile partial on the other side. The star stacking fault reported here has a different configuration from those previously studied, and thus a mechanism for its formation is proposed to adapt to its configuration.

8.3 Experiment

One hundred millimeter diameter, longitudinally cut, 4H-SiC wafers grown by the physical vapor transport technique were used in our study. SWBXT transmission images of $\{1\bar{1}00\}$, $\{\bar{1}101\}$ and $\{11\bar{2}0\}$ reflections were recorded using Agfa Structurix D3-SC film. Grazing-incidence images of the $11\bar{2}8$ reflection were recorded from Si-faces of the specimens at an x-ray incident angle of 2°. The imaging was carried out at the Stony Brook Synchrotron Topography Station, Beamline X-19C, at the National Synchrotron Light Source at Brookhaven National Laboratory.

8.4 Results and discussion

1. Characterization of Six-pointed Star Stacking Faults

Fig. 8.1(a) shows contrast from stacking fault configuration of interest which is in a shape of six-pointed star. The contrast is composed of six rhombuses which share one common corner. It is evident that the contrast of each rhombus is not uniform in that it appears that each large rhombus contains one or more smaller rhombuses inside. This is caused by overlapping of contrast from stacking faults on top of each other in different layers of basal planes which are all projected onto one plane of the film forming a plan-view image. In other words, each rhombus of the contrast from the star stacking fault are actually from stacking faults on multiple basal planes. The greater the number of overlapping faults, the stronger the contrast would be. It is clear in the image that all faults are connected to the center of the star.

The star stacking fault shows strong contrast in all $\{1\bar{1}00\}$ reflections, as one example shown in Fig. 8.1(a), and also in all $\{\bar{1}101\}$ reflections, an example of which is shown in Fig. 8.1(b). However, it shows no contrast in all $\{11\bar{2}0\}$ reflections, as shown in Fig. 8.1(d)-(f). According to our pervious understanding of the contrast behavior of various stacking faults [82-84] , the fault vector can be determined to be Shockley type of any of the three $a/3<1\bar{1}00>$ fault vectors.

The three $\{11\bar{2}0\}$ reflections also enable determination of the Burgers vectors of the partials bounding the stacking faults, as shown in Fig. 8.1(d)-(f). Since the stacking faults are out of contrast in these three reflections, the partial dislocations bounding the faults can be clearly observed. However, no reflection of $<11\bar{2}0>$ type shows the complete outline of the star stacking fault and in each reflection the outline of a pair of rhombuses is missing. The Burgers vector of the partials at the edges of the missing rhombuses can be determined through contrast extinction criteria, whereby a dislocation is out of contrast when g.b is equal to zero (b is Burgers vector and g is reflection vector). As a result, the Burgers vector of the partials connected to points 1 and 4 indicated in Fig 8.1.(a) are determined to be $(a/3)[1\bar{1}00]$ as they are out of contrast in the $11\bar{2}0$ reflection in Fig. 8.1(d); the Burgers vector of those connected to points 2 and 5 is

(a/3)[$01\bar{1}0$] as they are out of contrast in the $2\bar{1}\bar{1}0$ reflection in Fig. 8.1(e); and the Burgers vector of those connected to points 3 and 6 is (a/3)[$\bar{1}010$] as they are out of contrast in the $1\bar{2}10$ reflection in Fig. 8.1(f). It is also noticed that all the partials bounding the star stacking faults lie along <$11\bar{2}0$> directions and make angles of 30 °to their Burgers vectors.

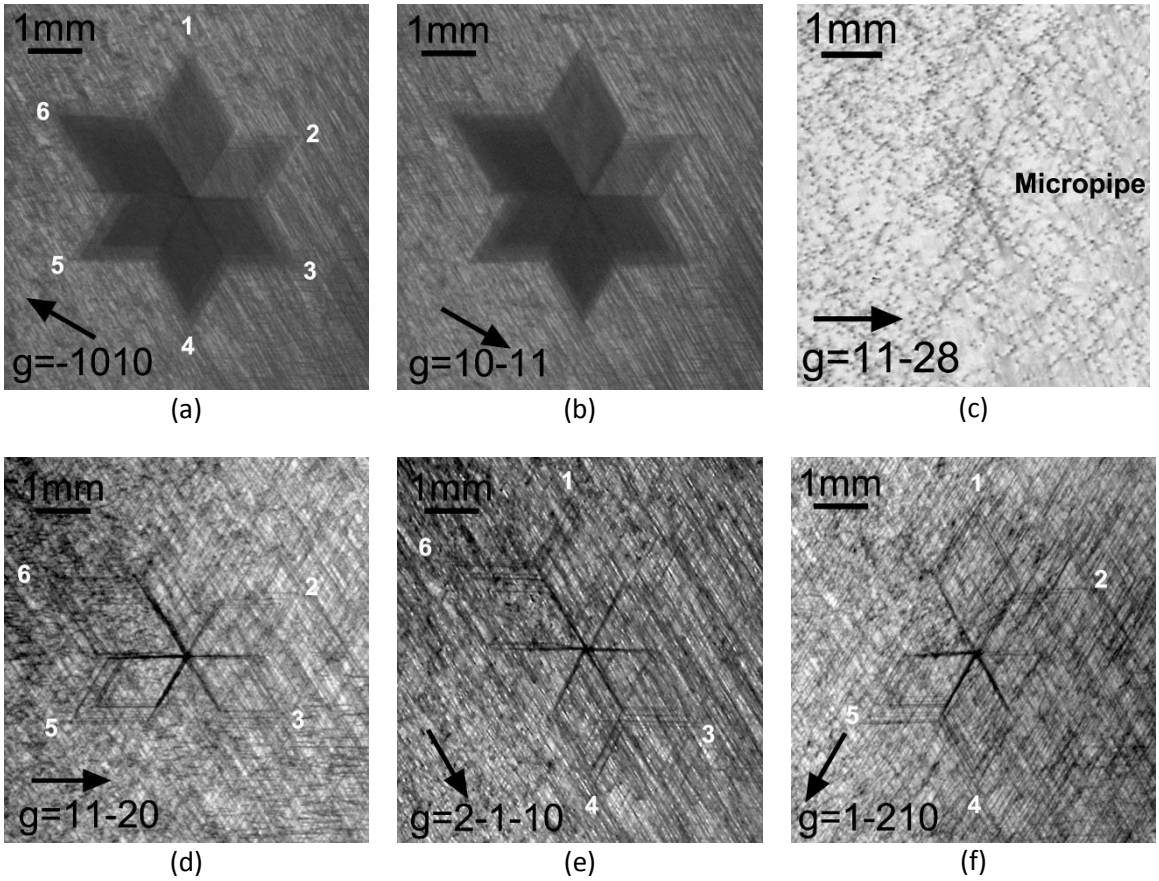

Fig. 8.1 SWBXT images recorded from a region in a 4H-SiC crystal containing six-pointed star stacking faults: (a) transmission image of $\bar{1}010$ reflection where each point of the star is labeled from 1 to 6; (b) transmission image of $10\bar{1}1$ reflection; (c) grazing-incidence image of $11\bar{2}8$ reflection revealing that a small micropipe is located in the center of the star stacking fault; (d)-(f) transmission images of three {$11\bar{2}0$} reflections showing absence of the fault contrast as well as partial dislocations connected to those missing points in each image

The same area containing the star stacking fault was studied using grazing-incidence topography, as shown in Fig. 8.1(c). Contrast from a small micropipe is found in the center of the star stacking fault. It can also be seen that four linear bands of dislocations emanate from the micropipe while the two linear bands of dislocations which are parallel to the reflection vector direction indicated in the image are out of contrast. None of the six bands of dislocations emanating from the micropipe ever completely disappears in any of the {$11\bar{2}0$} or {$1\bar{1}00$} reflections, which implies that none of the bands are composed of dislocations with a single Burgers vector. Instead, each band of dislocations should include dislocations with at least two different Burgers vectors of any (a/3){$11\bar{2}0$} type or (a/3){$1\bar{1}00$} type.

At this point, the configuration of star stacking faults can be summarized to be the shape of a six-pointed star comprising faults with three different fault vectors of the Shockley type. The outline of the star is confined by 30 ° Shockley partial dislocations lying along $<11\bar{2}0>$ directions. A micropipe is located in the center of the star stacking fault from which emanates six bands of dislocations with a mixture of Burgers vector. A schematic representation of the configuration is shown in Fig. 8.2.

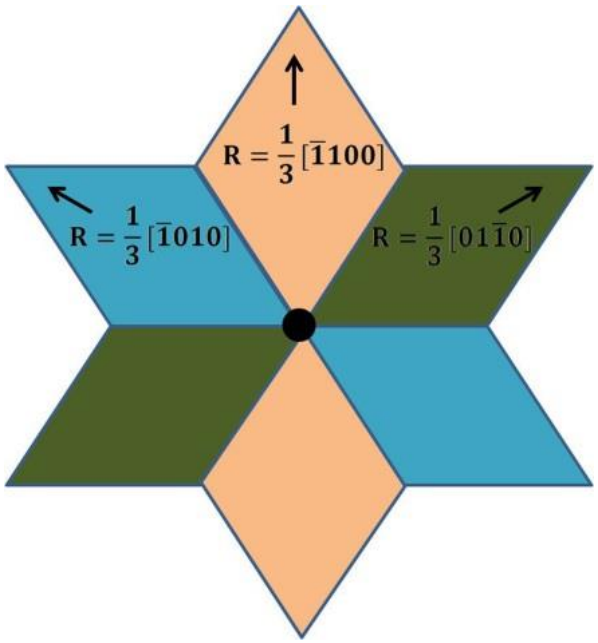

Fig. 8.2 Schematic drawing of the configuration of six-pointed star stacking faults

2. Formation Mechanism of Six-pointed Star Stacking Faults

The background of the star stacking fault in Fig. 8.1(a) comprises straight basal plane dislocations (BPDs) whose contrast is displayed as black lines. Despite their large number in Fig. 8.1(a) it can be identified that they are mainly oriented toward $[\bar{2}110]$ and $[11\bar{2}0]$ directions. Two more $\{1\bar{1}00\}$ reflections recorded from the same area are shown in Fig. 8.3. In the background of Fig. 8.3(a) BPDs are oriented toward $[1\bar{2}10]$ and $[11\bar{2}0]$ direction, but BPDs along $[\bar{2}110]$ direction all disappear in $0\bar{1}10$ reflection. In the background of Fig. 8.3(b) BPDs are oriented toward $[\bar{2}110]$ and $[1\bar{2}10]$ directions, but BPDs along $[11\bar{2}0]$ direction all disappear in $(1\bar{1}00)$ reflection. Therefore, by doing g.b analysis the Burgers vectors of the missing BPDs in each reflection can be determined and it turns out that they are all pure screw dislocations with Burgers vectors of $(a/3)<11\bar{2}0>$. These pure screw dislocations are the precursor to the mechanism of formation of the star stacking fault configuration.

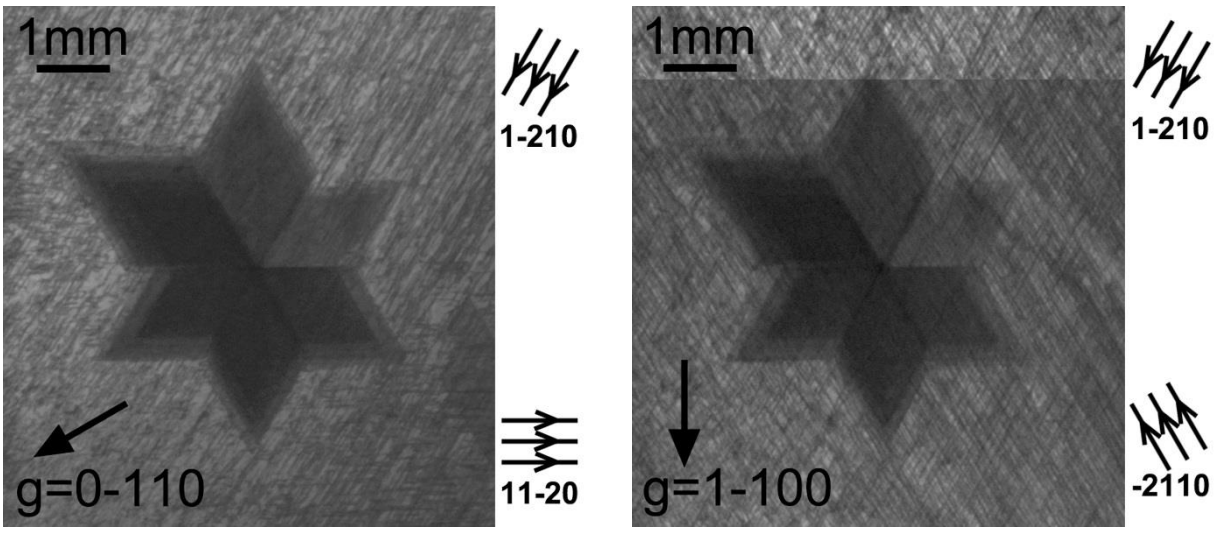

(a) **(b)**

Fig. 8.3 SWBXT images recorded from the region containing six-pointed star stacking fault: (a) transmission image of $0\bar{1}10$ reflection; (b) transmission image of $1\bar{1}00$ reflection

The micropipe located in the center of the star stacking fault is another major player in the formation mechanism. It is known that micropipes can be the source of BPDs [94]. The BPDs generated from micropipe in basal plane slip system $<11\bar{2}0>(0001)$ can have different character, i.e. different angles between their Burgers vectors and line directions. It is well known that the mobility of non-screw dislocations is higher than that of screw dislocations in SiC [39] and thus non-screw BPDs move more easily in response to stress above a certain temperature. Therefore, non-screw dislocations generated from the micropipe are seldom observed in the background of the images of our area of interest. In addition, dislocations generated from micropipes in the prismatic slip system $<11\bar{2}0>\{1\bar{1}00\}$ have also been reported [95, 96]. Furthermore, screw character dislocations with Burgers vectors of $(a/3)<11\bar{2}0>$ can cross slip from prismatic plane $\{1\bar{1}00\}$ onto basal plane [97].

In our model for the formation mechanism of the star stacking fault configuration, dislocations with Burgers vectors of $(a/3)<11\bar{2}0>$ are nucleated from a micropipe in both the basal plane slip system and prismatic slip system, as shown in Fig. 8.4(a). The dislocations which are generated in the prismatic slip system which have screw character can later cross slip onto the basal plane. The dislocations which are generated in basal plane which are operative in our model have $60°$ character (i.e. $60°$ between their Burgers vector and line direction). One example of these two types of dislocations as well as their partials is illustrated in Fig. 8.4(b). Dislocation 1 is generated in prismatic slip system but cross slips into basal plane. It has to be pure screw type and S1 and S2 are its partials. Dislocation 2 is appointed to be generated in basal plane slip system and is a $60°$ dislocation whose partials are S3 and S4. Dislocations 2 and 1 may or may not be in different basal planes at different levels. It should be noted that the Burgers vectors of S3 and S1 are opposite sign. Strong attractive forces might therefore be expected between these two partials.

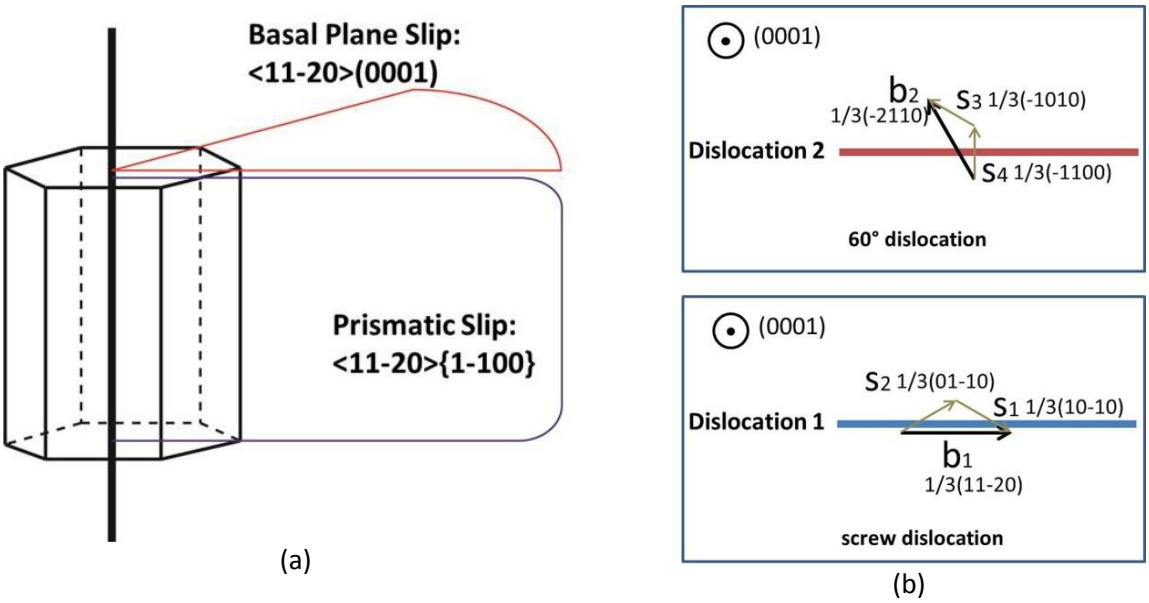

Fig. 8.4 (a) Schematic drawing of dislocations nucleating from a micropipe in both the basal plane slip system and prismatic slip system; (b) Burgers vectors and partials of a 60° dislocation and a screw dislocation on basal plane

The force between these dislocations is calculated in order to understand their mutual influence. According to dislocation theory [60], the total force F exerted on a unit length of a mixed dislocation from another mixed dislocation is

$$F = -(\sigma_{xy} b_x + \sigma_{yz} b_z) i + (\sigma_{xx} b_x + \sigma_{xz} b_z) j \quad \text{..... (14)}$$

Where b_x, b_z is components of the Burgers vector of the former dislocation, σ_{xx}, σ_{xy}, σ_{yz}, σ_{xz} are components of the stress field arising from the latter dislocation. The origin of the coordinate system is set at the dislocation line; z-axis is parallel to the dislocation line direction; x-axis is perpendicular to the dislocation line and lies in the slip plane; y-axis is perpendicular to the slip plane.

For the case of our model, where the dislocations are parallel to each other and may lie in separate basal planes, only the first component of F in eqn. 1 need to be calculated as it is responsible for the glide of the dislocation on the basal plane.

For a screw dislocation,

$$\sigma_{xy} = 0; \sigma_{yz} = -\frac{\mu b}{2\pi} \cdot \frac{x}{x^2 + y^2} \quad \text{..... (15)}$$

For an edge dislocation,

$$\sigma_{xy} = -\frac{\mu b}{2\pi(1-\nu)} \cdot \frac{x(x^2 - y^2)}{(x^2 + y^2)^2}; \sigma_{yz} = 0 \quad \text{..... (16)}$$

where b is the Burgers vector of the dislocation, μ is shear modulus, and ν is Poisson's ratio. A mixed dislocation can be regarded as the combination of a screw and an edge dislocation.

Therefore, the force exerted on S1 from dislocation 2 is

$$-\frac{3s^2t\mu}{8\pi(h^2+t^2)}-\frac{3s^2t(-h^2+t^2)\mu}{8\pi(h^2+t^2)^2(1-\upsilon)} \quad \text{.....(17)}$$

and the force exerted on S2 from dislocation 2 is

$$-\frac{3s^2t\mu}{8\pi(h^2+t^2)}+\frac{3s^2t(-h^2+t^2)\mu}{8\pi(h^2+t^2)^2(1-\upsilon)} \quad \text{.....(18)}$$

where s represents the magnitude of the partial's Burgers vector, h is the separation of two basal planes upon which dislocations 1 and 2 lie, and t is the distance between two dislocations projected onto the basal plane. Two situations are considered. The first situation is when dislocations 1 and 2 are on the same basal plane which means h=0, though the chance of this situation might be relatively small. Taking ν=0.2, eqn. 4 becomes $-\frac{27s^2\mu}{32\pi t}$ and eqn. 2 becomes $\frac{3s^2\mu}{32\pi t}$. This can be interpreted as dislocation 2 has attractive force on S1 and repulsive force on S2. In other words, S1 becomes sessile and S2 becomes glissile and under certain stress S2 can start to move leaving a Shockley fault behind in its wake.

The second situation is when dislocations 1 and 2 are on two different basal planes. The forces on S1 and S2 exerted from dislocation 2 are plotted in Fig. 8.5 (a) and (c), respectively. These graphs are plotted for a h value of 10nm, about 10 atomic layers of 4H-SiC structure. Over a long range of t, the forces on S1 and S2 are opposite, with attractive forces on S1 and repulsive forces on S2 being apparent, as shown in Figs. 8.5(a)&(c). A significant difference exists from the first situation when t is very small, that is, when the partial is very close to dislocation 2 along the slip direction. Fig. 8.5(b) shows the region near the origin of Fig. 8.5(a) at much higher magnification. It indicates that S1 is locked inside a region about +5 nm and -5nm from the position right below (or above) dislocation 2 and can no longer glide. As indicated in Fig. 8.5(d), S2 is stable (locked in position) near the origin, but beyond the position of +30 or -30 nm it will experience continuous repulsive force. Therefore, when dislocation 1 is not nucleated right below (or above) dislocation 2 but with enough mutual lateral shift, the two partials will separate as soon as dislocation 1 cross slips from the prismatic plane to the basal plane and one partial becomes sessile and the other becomes glissile.

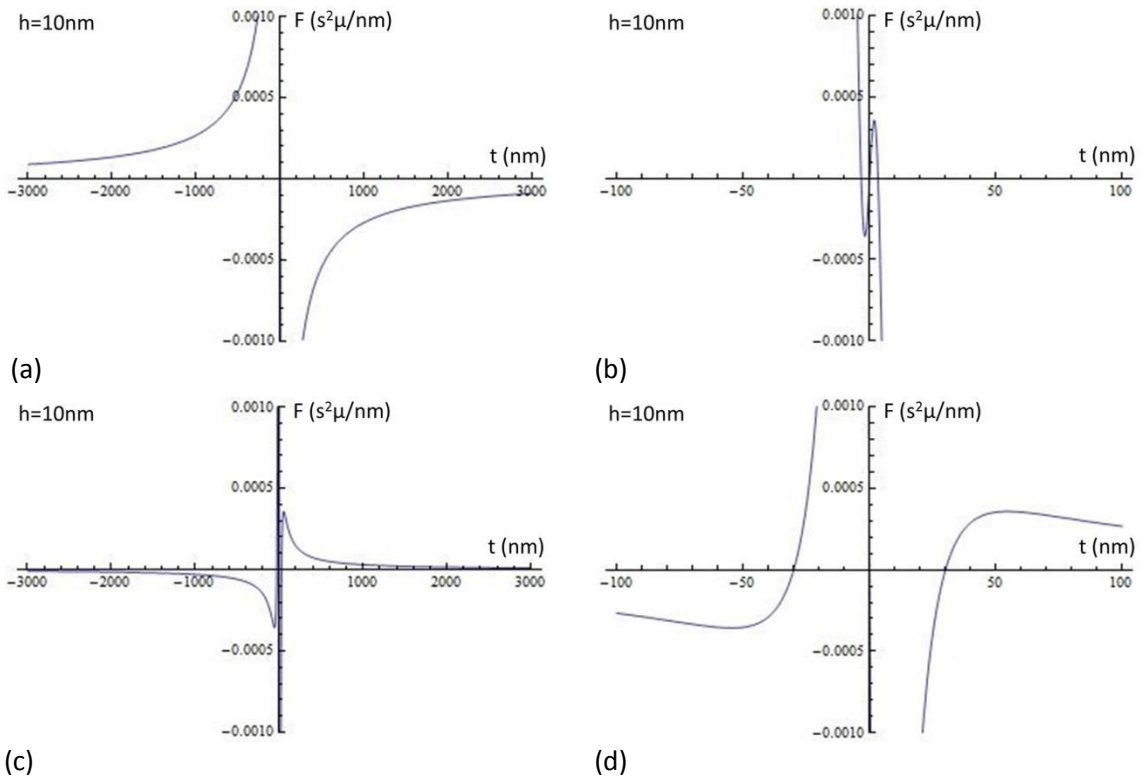

Fig. 8.5 The forces on S1 and S2 exerted by dislocation 2: (a) the force on S1, t in range [-3000, 3000]; (b) the force on S1, t in range [-100, 100]; (c) the force on S2, t in range [-3000, 3000]; (d) the force on S2, t in range [-100, 100]. The unit of force on dislocation line, F, is (s^2 μ /nm). Diagrams are plotted with software Mathematica 8

In the same way one can also calculate the force on S3 and S4 exerted from Dislocation 1. The force on S3 is negative as expected due to its opposite sign of Burgers vector with respect to S2. The force on S4 turns out to be zero. Then, it becomes obvious that S2 is most likely to glide in response to stress and lead to expansion of a Shockley fault since it is the only one among the four partials that can receive continuous repulsive force over a long range.

As 4H-SiC is six-fold symmetric along (0001) growth direction, the dislocation reaction discussed above can happen between all dislocations nucleated at the micropipe core on the six symmetry related prismatic planes and dislocations generated on the basal plane. Those screw segments of dislocations generated on the prismatic plane can cross slip onto the basal plane and the glissile partials, which are 30 °degree dislocations, start to move in response to stress leaving Shockley faults in their wake. The six-pointed star shaped stacking fault configuration forms as the glide of Shockley partials respectively occurs in all six slip directions. Fig. 8.6 illustrates a moment when the star pattern of stacking fault is forming. The solid lines represent the position of partials bounding the Shockley faults already formed and the dashed lines represent the final positions of partials bounding the star stacking fault configuration. The image shows the situation when an (a/3)$[01\bar{1}0]$ Shockley fault is expanding toward the direction indicated by the black arrows, while fault (a/3)$[\bar{1}100]$ is already formed and fault (a/3)$[\bar{1}010]$ has not yet

formed. Eventually, the complete star stacking fault configuration will be like the one illustrated in Fig. 8.2.

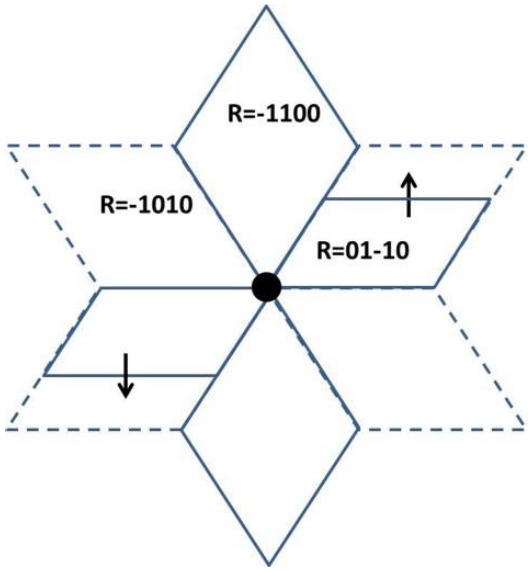

Fig. 8.6 Illustration of a snapshot when six-pointed star shaped stacking fault is forming.

8.5 Conclusion

Stacking faults in a configuration shaped like a six-pointed star comprise faults with three different fault vectors of the Shockley type. The outline of the star is confined by 30 ° Shockley partial dislocations lying along $<11\bar{2}0>$ directions. A micropipe is located in the center of the star stacking fault from which emanates six bands of dislocations with a mixture of Burgers vectors. It is postulated that 60 ° dislocations of $a/3<\bar{2}110>$ Burgers vector on basal plane and pure screw dislocations of $a/3<11\bar{2}0>$ Burgers vector on prismatic plane nucleate from the micropipe. The screw dislocations can cross slip from prismatic plane to basal plane. Then, two partials of a screw dislocation start to separate under stress because one partial is sessile and the other one glissile due to mutual influence of force from dislocations generated in two different slip systems. Shockley faults form and expand as a result of glide of the glissile partials. The six-point star stacking faults appear when the glide of Shockley partials occurs in all six slip directions that are perpendicular to the dislocation line direction.

9. Formation of 6H Stacking faults via 2D nucleation in PVT grown 4H-SiC

9.1 Outline

Synchrotron white beam x-ray topography (SWBXT), synchrotron monochromatic beam x-ray topography (SMBXT), and high resolution transmission electron microscopy (HRTEM) studies have been carried out on stacking faults in PVT grown 4H-SiC crystal. Their fault vectors were determined by SWBXT to be 1/3<-1100>, 1/2<0001>, 1/6<-2203>, 1/12<4-403>, 1/12<-4403>. HRTEM studies reveal their similarity in stacking sequences as limited numbers of bilayers of 6H polytype structure. Simulation results of the two partial dislocations associated with the stacking faults in SMBXT images reveal the opposite sign nature of their Burgers vectors. A mechanism for stacking fault formation via 2D nucleation is postulated.

9.2 Introduction

Minimizing defect density in 4H-SiC bulk crystals is a key issue to improve the performance of power devices fabricated on 4H-SiC substrates. Generally speaking, defects intersecting the growth surface will extend into the homoepitaxial layer during epitaxial growth, potentially impacting device performance. In 4H-SiC, like other polytypes of this material, low stacking fault (SF) energies can lead to a tendency to form SFs on the basal plane. SFs can be created by glide of partial dislocations during post growth processes, such as Shockley faults [39, 44], double Shockley faults [23] and six-pointed star-shaped faults (see Chapter 8), or can form through disordered step flow during growth, such as intrinsic Frank faults [64] and V shaped defects (See Chapter 10).

Our previous studies on SFs in 4H-SiC bulk crystal, grown by the physical vapor transport technique (PVT), indicate that SFs can nucleate from the deflected outcrops of threading dislocations with c-component of Burgers vector overgrown by macrosteps on the basal plane [82-84]. Direct observation of SFs nucleating from threading dislocations with c-component of Burgers vector has been achieved with synchrotron white beam x-ray topography (SWBXT), as discussed in Chapter 7. However, there are also many SFs observed in our studies which are not connected with such dislocations. In this paper, these SFs are studied using SWBXT, synchrotron monochromatic beam x-ray topography (SMBXT), and high resolution transmission electron microscopy (HRTEM).

9.3 Results and Discussion

The SFs were initially observed with SWBXT and their fault vectors, **R**, were determined according to their differences in contrast extinction behavior on topography images with different reflection vectors **g**. Contrast from SFs is expected to disappear when **g ⋅ R** is equal to an integer (including zero) and is expected to be very weak (almost invisible) when **g ⋅ R** equals to ±1/12 or ±11/12. Contrast should be weak but visible when **g ⋅ R** equals to ±1/6 or ±5/6 and well-marked when **g ⋅ R** equals to ±1/2, ±1/3, or ±2/3. In Fig. 9.1, five SFs are marked with Roman numbers from I to V in SWBXT transmission images of regions near the edge of an offcut basal wafer. SF I shows no contrast on the 11-20 reflection; SF II shows weak contrast on the 1-101and 10-11 reflections and no contrast on the 11-20 reflection; SF III is invisible on the -1100 and 1-10-2 reflections; SF IV is invisible on the 1-101 and 11-20 reflections; and SF V is

invisible on the 10-11, 11-20 reflections. Therefore, their fault vectors can be determined to be 1/3<-1100>, 1/6<-2203>, 1/2<0001>, 1/12<4-403>, and 1/12<-4403> respectively.

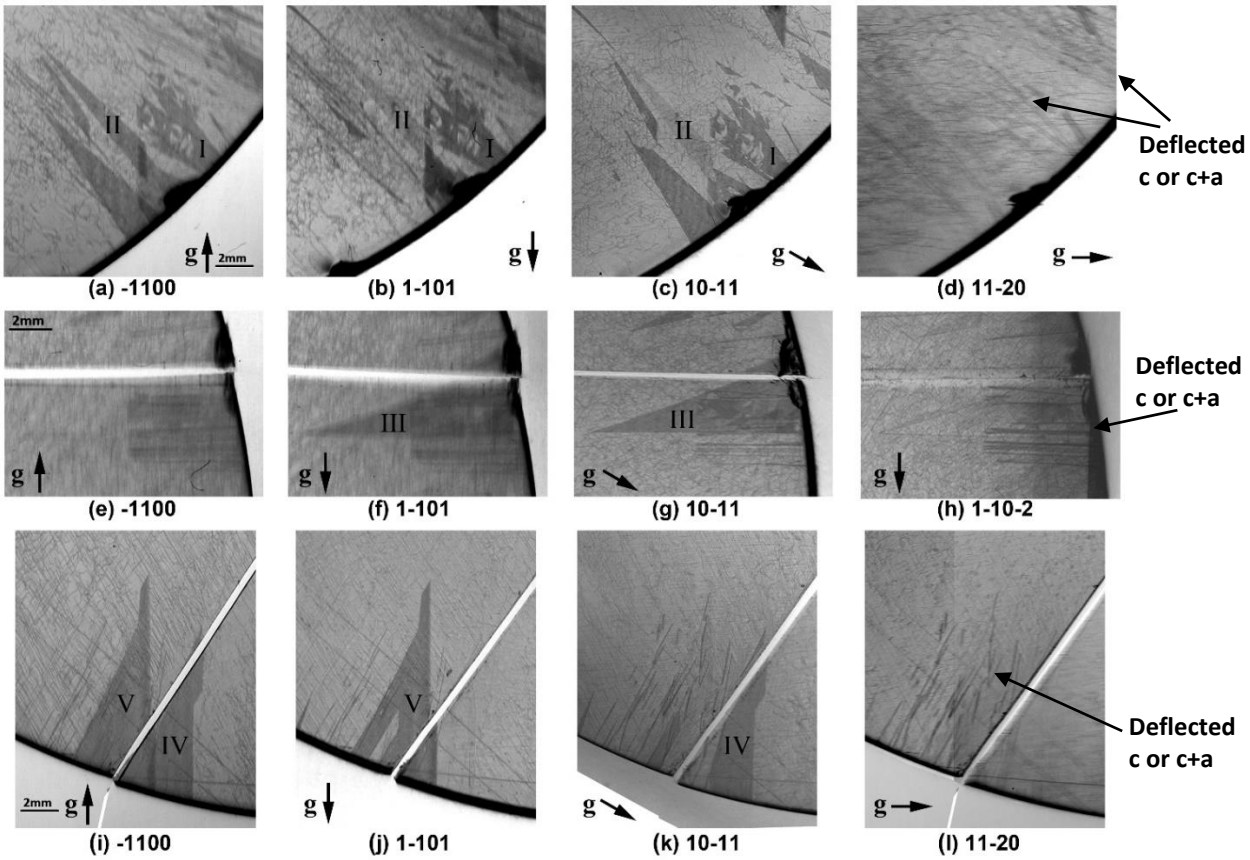

Figure 9.1 SWBXT transmission images recorded from a PVT-grown 4H-SiC basal wafer (with 4° offcut): (a)-(d) contrast behavior of SF I and II; (e)-(h) contrast behavior of SF III; (i)-(l) contrast behavior of SF IV and V

Fig. 9.2(a)&(b) shows images of ray tracing simulation of the contrast from deflected threading c+a dislocations in SMBXT 11-28 grazing images. The contrast is mainly composed of a black line and a white gap on one side of the back line. When the sign of c-component of Burgers vector reverses, the white gap switches to the other side of the back line. Partial dislocations associated with SFs having fault vectors like those of SFs #II, III, VI, V in Fig. 9.1 also contain c-component of Burgers vector and should exhibit similar black/white contrast. In Fig. 9.2(c), an SMBXT 11-28 grazing image is recorded from a region on the Si-face of a wafer with penetration depth of 49um. The pairs of partial dislocations bounding the three SFs in the image show reversed black/white contrast. The ones bounding the right side of the SFs have contrast similar to Fig. 9.2(a) and the other ones bounding the left side have contrast similar to Fig. 9.2(b), which suggests they have opposite sign c-components of Burgers vector. Furthermore, no defects are observed to connect with the apexes of the three SFs in the image which are expected to be their nucleation sites. These two factors lead to the speculation that these SFs spontaneously form during crystal growth.

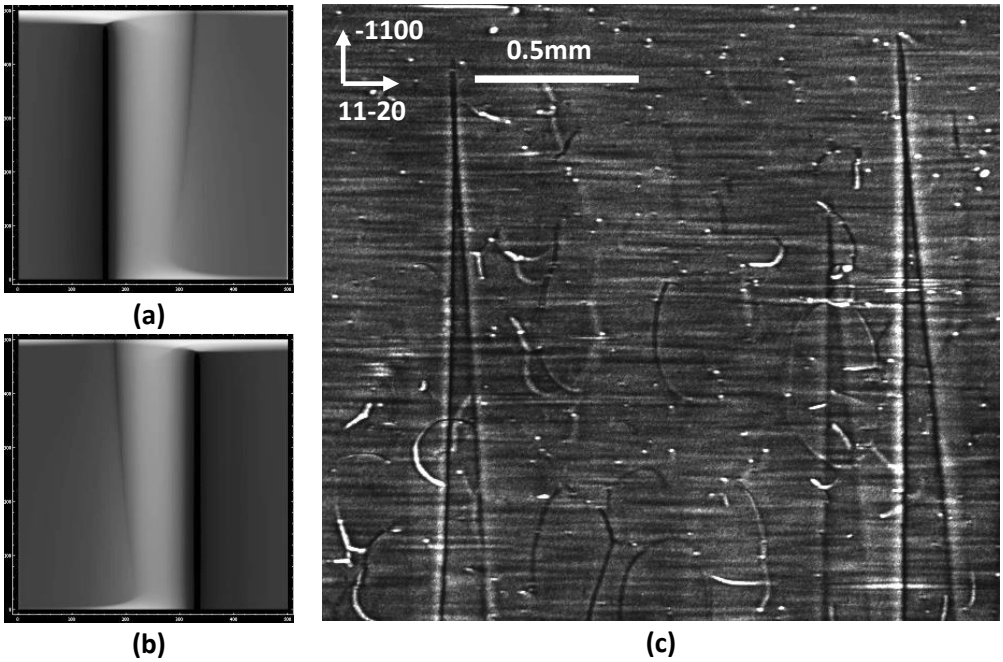

Figure 9.2 (a) Ray tracing simulation of deflected c+60°a dislocation, box size 50um×50um; (b) Ray tracing simulation of deflected -c+60°a dislocation, box size 50um×50um; (c) SMBXT 11-28 grazing image showing reversed back/white contrast from the two partial dislocations associated with stacking faults

{11-20} cross sectional HRTEM studies have been carried out on SFs #II, III, IV, V. Their stacking sequences are observed to be (32223), (33), (333), and (33333) respectively (according to the Zhadnov notation), as shown in Fig. 9.3. The method to obtain the fault vectors based on the observed stacking sequence was presented in Chapter 11. It is easy to find the similarity among these stacking sequences which can be regarded as limited numbers of bilayers of 6H polytype structure. SF II contains two overlapping set of three bilayers of 6H-SiC (33) stacking sequence, seperated by six bilayers of perfect 4H-SiC (22) stacking sequence; SFs III, IV, V have six, nine and fifteen bilyers of 6H-SiC (33) stacking sequence respectively. Therefore, it can be further speculated that very thin layers of 6H polytype have been nucleated during crystal growth and their thicknesses are limited to several atomic layers so that they merely constitute faulted regions in the 4H lattice.

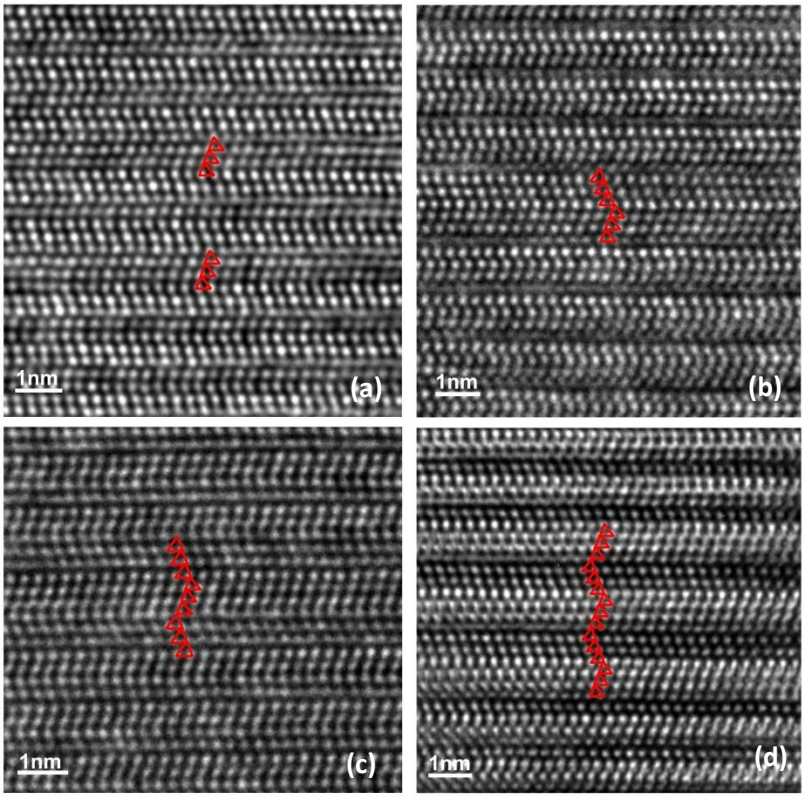

Figure 9.3 HRTEM images recorded from {11-20} cross sectional samples: (a) (32223) stacking sequence of SF II; (b) (33) stacking sequence of SF III; (c) (333) stacking sequence of fault IV; (d) (33333) stacking sequence of SF V

It is observed in SWBXT images (Fig. 9.1) that the appearance of SFs is limited to the edge of the wafer, such as those SFs in Fig. 9.1. The edge region corresponds to a higher temperature region in the growth cell than the center region [98]. Growth of 6H-SiC requires less supersaturation than 4H-SiC and high growth temperature in 4H-SiC bulk growth can readily lead to the formation of 6H-SiC polytype [99-101]. In addition, it is also observed in SWBXT images (Fig. 9.1) that the formation of the stacking faults is often accompanied with deflection of threading dislocations with c-component of Burgers vector in the vicinity, which implies a connection between these two processes. The deflection of such dislocations can happen due to overgrowth by macrosteps (discussed in Chapter 4) which are formed by step bunching [102]. Since the step structure near the edge of the boule is steeper than the center due to the dome shape of growing surface (as those SiC ingots shown in Ref. [101, 102]), more step bunching is expected to happen near the edge region.

9.4 Conclusion

A mechanism for stacking fault formation via 2D nucleation is postulated as schematically shown in Fig. 9.4. Macrosteps first form due to step bunching near the edge region of the growing surface, and their slow speed of advance provides a time interval for the nucleation of 6H-SiC nuclei whose sizes of various atomic layers are thermodynamically determined by temperature, supersaturation and other growth parameters at the growing surface. The 6H-SiC can expand two-dimensionally as newly arrived atoms occupy the energy favorable sites, such as kinks and steps, provided by the 6H-SiC nuclei. One side of the 2D 6H-SiC will soon meet the macrostep because the terrace in front of the macrostep has a limited width. Macrosteps will subsequently overgrow the already formed 6H-SiC to maintain the integrity of

the stacking sequence, while the faulted stacking sequence around the 2D 6H-SiC region will propagate in the direction of step flow and fan out towards the outer periphery of the crystal. Since the distances that 6H nuclei can expand freely before reaching the macrostep are negligible compared to the sizes of fully extended stacking faults, the stacking faults will exhibit triangular shapes.

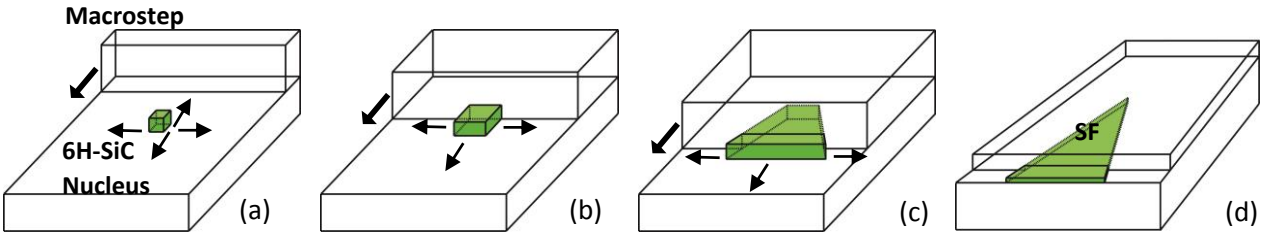

Figure 9.4 Schematic drawings of stacking fault formation via 2D nucleation of 6H-SiC: (a) nucleation of 6H-SiC; (b) 2D expansion of 6H-SiC; (c) overgrowth of 2D 6H-SiC by macrostep; (d) Expansion of 6H stacking fault. (a), (b) and (c) are drawn at micro scale and (d) are drawn at macro scale. Since the size of 2D 6H-SiC before meeting the macrostep is tiny compared to the size of the completely expanded stacking fault, the nucleation point of stacking fault will exhibit as the apex of a triangular shape.

10. Formation of V Shaped Defects in CVD grown 4H-SiC Homoepitaxial Layers

10.1 Outline

Synchrotron white beam x-ray topography images show that faint needle-like surface morphological features observed on the Si-face of 4H-SiC homoepitaxial layers using Nomarski optical microscopy are associated with V shaped stacking faults in the epilayer. KOH etching of the V shaped defect reveals small oval pits connected by a shallow trench which correspond to the surface intersections of two partial dislocations and the stacking fault connecting them. Transmission electron microscopy (TEM) specimens from regions containing the V shaped defects prepared using focused ion beam milling show stacking sequences of (85), (50) and (63) at the faulted region using high resolution TEM. In order to study the formation mechanism of V shaped defect, low dislocation density 4H-SiC substrates were chosen for epitaxial growth, and the corresponding regions before and after epitaxy growth are compared in SWBXT images. It is found that no defects in the substrate are directly associated with the formation of the V shaped defect. Simulation results of the contrast from the two partial dislocations associated with V shaped defect in synchrotron monochromatic beam x-ray topography reveals the opposite sign nature of their Burgers vectors. Therefore, a mechanism of 2D nucleation during epitaxy growth is postulated for the formation of the V shaped defect, which requires elimination of non-sequential ***c***/4[0001] bilayers from the original structure to create the observed faulted stacking sequence.

10.2 Introduction

The quality of the epitaxial layers has greatly improved for the past decade due to several factors. First, for those defects inherited from the substrate, such as threading screw dislocations (TSDs) and micropipes (MPs), production of low defect density substrate wafers [98] correspondingly results in low defect densities in the epitaxial layers. Second, engineering of the epitaxial growth process enables the conversion of defects from a harmful category to a less harmful one. For example, basal plane dislocations (BPDs) can cause the degradation of device performance by generating Shockley stacking faults [58]. Therefore, BPDs are engineered to convert to threading edge dislocations (TEDs), which are electrically benign, by pre-growth etching [48] and interrupted growth [50, 51]. Third, optimized growth conditions can eliminate defects generated in the epilayer or at the substrate/epilayer interface, such as triangular defects [68, 103-105] and carrot defects [52, 65, 106]. Such progress in achieving higher quality epilayers relies on a complete understanding of different kinds of defects, which involves locating the defects, characterization of their nature, and determining their origins. In this part of the work, characterization of V shaped defects, which are occasionally observed in studies of 4H-SiC epilayers, is presented and their possible formation mechanism via 2D nucleation is discussed.

10.3 Experiment

Defects in four inch PVT-grown 4H-SiC substrate wafers are mapped and studied before epitaxial growth using synchrotron white beam x-ray topography (SWBXT), in both transmission and grazing geometries. Then, 4H-SiC homoepitaxial layers with an n-buffer plus n-type drift structure are grown on the Si-Face of the substrate by CVD. The epilayer surface is

first examined with Nomarski optical microscopy to check for the presence of V shaped defects. Then, defects are imaged and studied using SWBXT, using the same imaging geometries used for the substrate. Finally, the epitaxial wafers are etched using molten KOH to decorate the V defects. 11-20 cross-sectional TEM specimens are prepared from the V shaped defects using the focused ion beam (FIB) technique and studied with high resolution TEM (HRTEM).

10.4 Results and Discussion

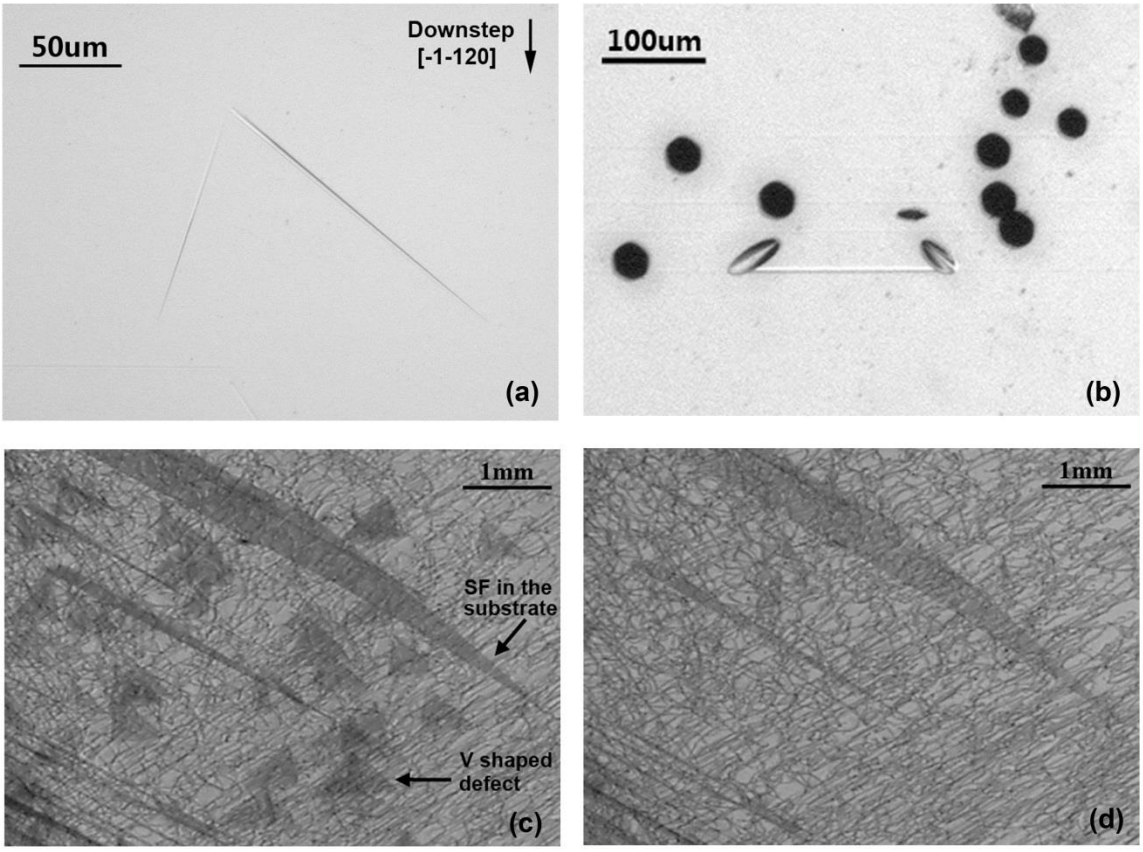

Figure 10.1 (a) Optical micrograph shows the faint needle-like surface morphological features associated with the V shaped defect.; (b) Etch pit pattern of V shaped defect is composed of two small oval pits connected by a shallow trench; (c) SWBXT –101-1 transmission images recorded from a region near the wafer edge containing V shaped defects; (d) SWBXT 10-10 transmission images recorded from the same region as Fig. 10.1(c)

V shaped defects can be recognized using Nomarski optical microscope as faint needle-like surface morphological features, as shown in Fig. 10.1 (a). These are different from triangular defects which show area contrast [68, 104, 105]. After KOH etching, an etch pattern consisting of two oval pits connected by a shallow trench is observed to be associated with the V shaped defect, as shown in Fig. 10.1(b). SWBXT studies reveal that these V shaped defects are actually stacking faults in the epilayer. The -101-1 transmission image (Fig. 10.1(c)) recorded from a region near the wafer edge shows a dark contrast feature of triangular shape associated with the V shaped defects. All such defects open towards the downstep direction and the height of the triangles corresponds to their projected length in the epilayer thickness, indicating that they are

completely contained within the epilayer. In comparison, the two much larger stacking faults with dark contrast visible on the image are contained within the substrate [82-84]. The V shaped defects are out of contrast in the 10-10 transmission image (Fig. 10.1(d)) and are determined to be Frank faults with a fault vector, R = n × ¼***c*** [0001] (n = 1, 2, or 3), which satisfies contrast extinction criteria of g.R = integer, where g corresponds to the reflection vector and R corresponds to the fault vector. Therefore, the two oval pits in Fig. 10.1(b) correspond to the partial dislocations and the shallow trench corresponds to the intersection of stacking faults with the sample surface.

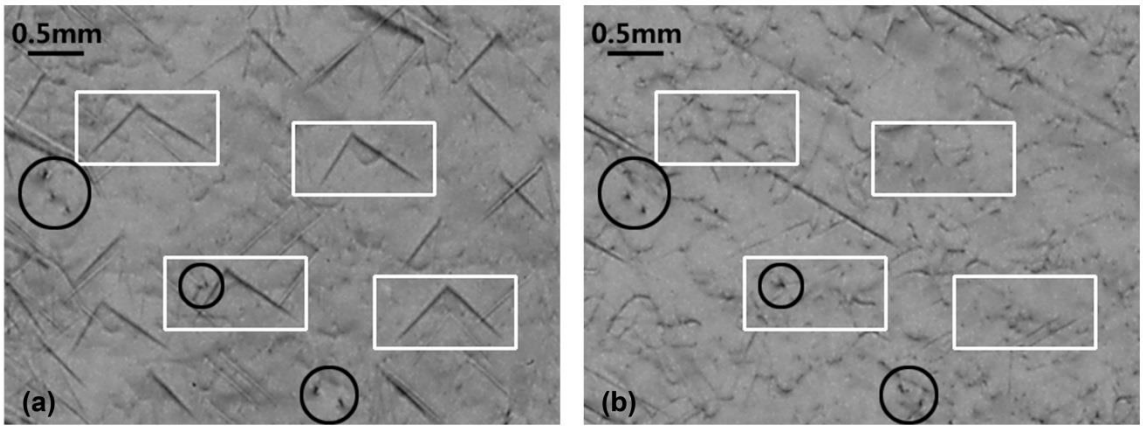

Figure 10.2 (a) SWBXT image recorded in grazing incidence (g=11-28) on the epilayer surface (Si-face) near the wafer edge containing V shaped defects. White boxes highlight four V shaped defects and black circles mark several TSDs; (b) 11-28 reflection recorded from the same region on Si face of the substrate before epitaxial growth

In order to investigate the origin of V shaped defect, 4H-SiC wafers before and after epitaxy growth were examined using SWBXT and images recorded from regions where V shaped defects form are carefully compared. Fig. 10.2(a) is a SWBXT 11-28 grazing image recorded from a region on the silicon face of the epitaxial wafer containing several V shaped defects. The stacking fault is out of contrast and the partial dislocations associated the stacking fault show linear contrast. Fig. 10.2(b) shows an 11-28 grazing image recorded from the same region before epitaxial growth. Several TSDs are marked with black circles and they are observed to appear at about the same locations before and after epitaxial growth, which suggests TSDs propagate along the threading direction from the substrate into the epilayer. By comparison, four V shaped defects are marked with white boxes and no defects are observed at the locations corresponding to the apexes of the V shaped defects which are expected to be their nucleation sites.

Therefore, it is reasonable to infer that these V defects are newly generated in the epilayer instead of being directly inherited from defects in the substrate. If so, according to the law of Burgers vector conservation, the partial dislocations associated with the V defects should have Burgers vectors of opposite signs, and their net Burgers vectors should be equal to zero. This has been confirmed by comparing the contrasts from the partial dislocations on synchrotron monochromatic beam x-ray topography (SMBXT) images, as shown in Fig. 10.3. Ray tracing simulations of the contrast from dislocations with c-component of Burgers vectors on the basal plane indicate that such dislocations show black & white line contrast and when the sign of the c-

component changes the black and white contrast is interchanged. This can be observed in Fig.10.3 for two V shaped defects where the partial dislocation on the left (L) side shows black-white contrast and the one on the right (R) side shows white-black contrast, which suggests they have opposite sign c-component of Burgers vector.

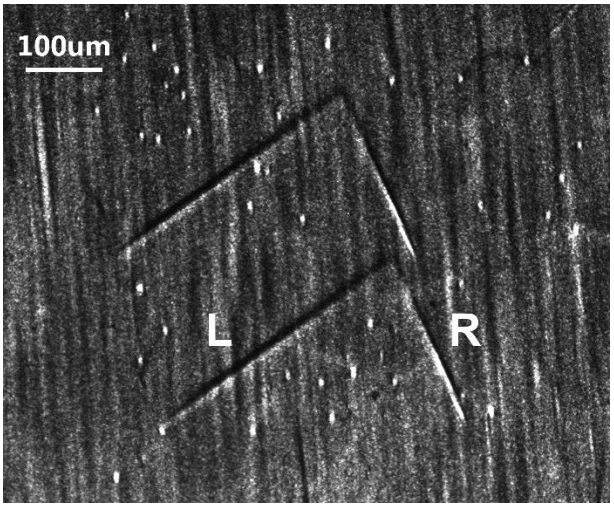

Figure 10.3 SMBXT image of 11-28 reflection showing contrast from two V shaped defects. Reverse in black/white contrast from the two partial dislocations associated with V shaped defects reveals the opposite sign nature of their Burgers vectors

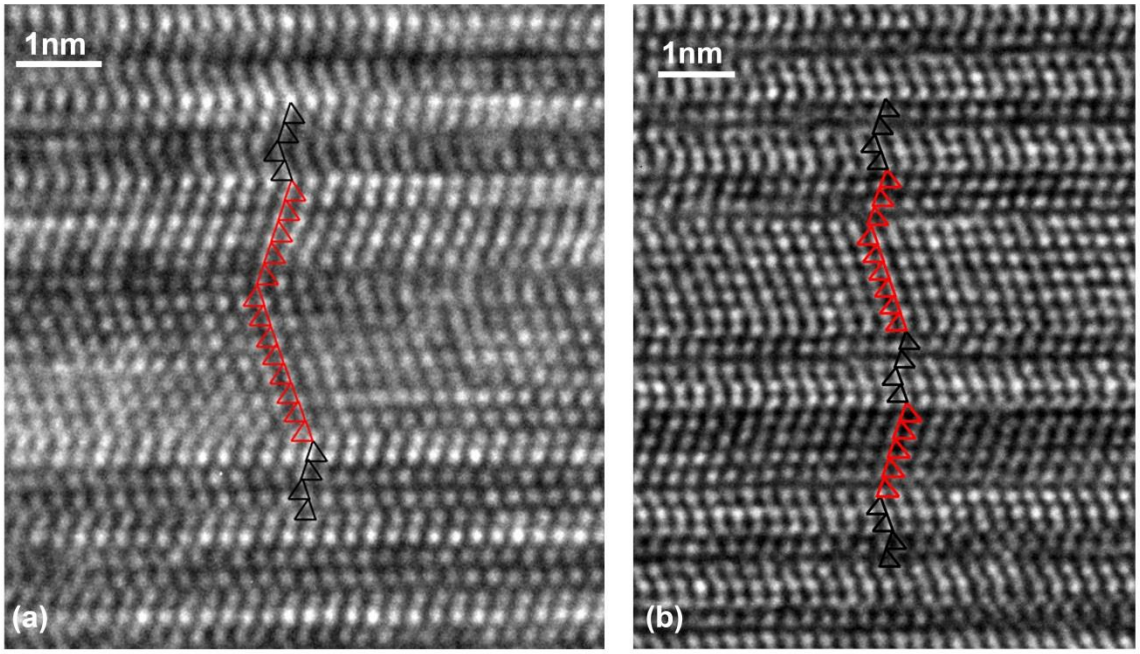

Figure 10.4 HRTEM images of V shaped defects showing: (a) (85) stacking sequence; (b) (50) and (63) stacking sequences

HRTEM studies have been carried out on V shaped defects using 11-20 cross-sectional TEM specimens prepared with the FIB technique. According to the Zhadnov notation, the lattice of perfect 4H-SiC should have a (22) stacking sequence. One TEM specimen prepared from a V shaped defect shows a (85) stacking sequence at the faulted region, as shown in Fig. 10.4(a) while another specimen from a different V shaped defect shows two faulted stacking sequences, (50) and (63), separated by 4 bilayers of perfect 4H-SiC (22) stacking sequence.

Fig. 10.5 demonstrates the transformation of the perfect (22) stacking sequence to an (85) faulted stacking sequence. Column I is the perfect (22) stacking sequence. Layer 7 is eliminated from column II and the new stacking sequence is formed in column III; as a result, a (50) faulted stacking sequence is generated. Next, elimination of layer 11 generates a (80) faulted stacking sequence as shown in column IV and V. Finally, elimination of layer 17 results in an (85) stacking sequence as shown in column VI and VII. Each time a bilayer is eliminated, a distortion of ¼***c***[0001] is introduced into the lattice, so the total distortion is ¾***c***[0001] in this case. During the transformation process no shift of the lattice on the (0001) plane is induced, which means no Shockley fault is generated. In a similar way, faulted stacking sequences observed in Fig. 10.4(b) can be generated by eliminating layer 7 to form a (50) stacking sequence and eliminating layers 17, 21 and 23 to form a (63) stacking sequence, as shown in Fig. 10.6. Therefore, a distortion of ¼***c***[0001] is associated with a (50) stacking sequence and a distortion of ¾***c***[0001] is associated with a (63) stacking sequence. These results are consistent with the fault vectors determined by the x-ray topography studies.

The above transformations from the perfect stacking sequence to the faulted ones can be achieved during actual crystal growth through 2D nucleation. Fig. 10.7 schematically shows the formation mechanism of a (50) stacking fault through 2D nucleation. 4H-SiC epitaxial growth is conducted on the vicinal (0001) plane and the step flow on the growth surface is sketched in Fig. 10.7(a). In Fig. 10.7(b), one SiC bilayer of wrong stacking sequence is nucleated on the growth surface (at layer 7) before the step flow arrives. As step flow growth continues, layer 8 at stacking position C merges into the 2D crystal on layer 7 which is also at stacking position C, because the same stacking sequences on each other is not allowed. Overall, it looks like that the original A step at layer 7 is overgrown by C step at layer 8, as shown in Fig. 10.7(c). Subsequently, the oncoming steps pile up on this distorted layer 8 and a (50) stacking fault is formed as shown in Fig 10.7(d). Thus, elimination of layer 7 can take place through 2D nucleation of a single SiC bilayer on the growth surface and result in the generation of a (50) fault. A similar process of 2D nucleation on layers 11 and 17 results in the generation of an (85) stacking sequence. Likewise, if 2D nucleation of one SiC bilayer happens on layers 7, 17, 21, 23, (50) stacking fault and (63) stacking faults separated by four bilayers of 4H-SiC can be generated.

10.5 Conclusion

X-ray topography and HRTEM studies reveal that V shaped defects are comprised of one or more overlapping Frank faults and can be generated by repetitive 2D nucleation of a single SiC bilayer at different atomic layers during epitaxial growth. So far, three faulted stacking sequences, namely (85), (50) and (63), are observed to be associated with V shaped defects. For the (50) stacking fault, an operation to eliminate one SiC bilayer is required to transform the lattice from the perfect stacking sequence to the faulted one, which introduces a distortion of

¼***c***[0001] to the lattice. For both (85) and (63) stacking faults, this operation is repeated three times and a distortion of ¾***c***[0001] is induced in the lattice.

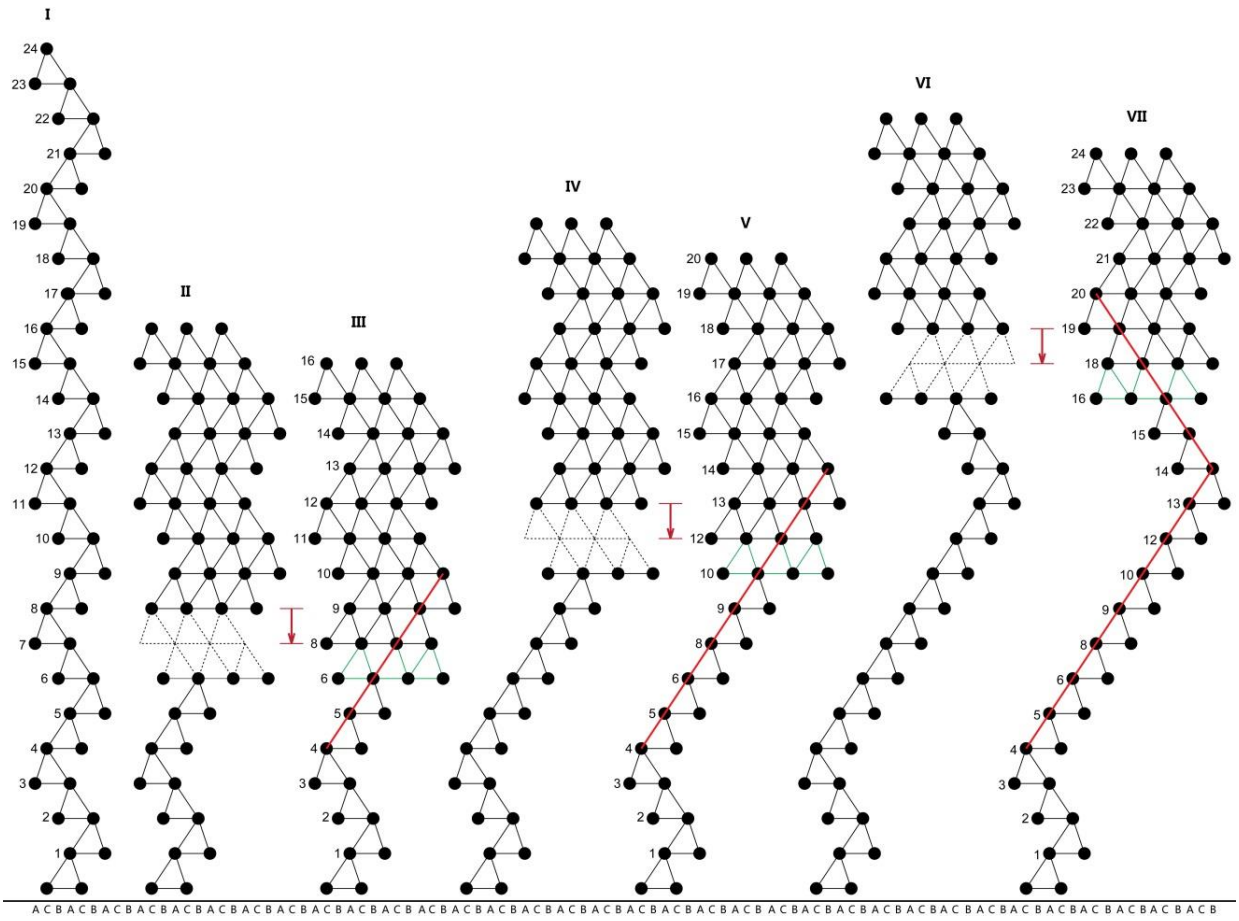

Figure 10.5 Transformation of 4H-SiC stacking from perfect (22) stacking sequence to (85) faulted stacking sequence. Refer to text for details on transformation steps.

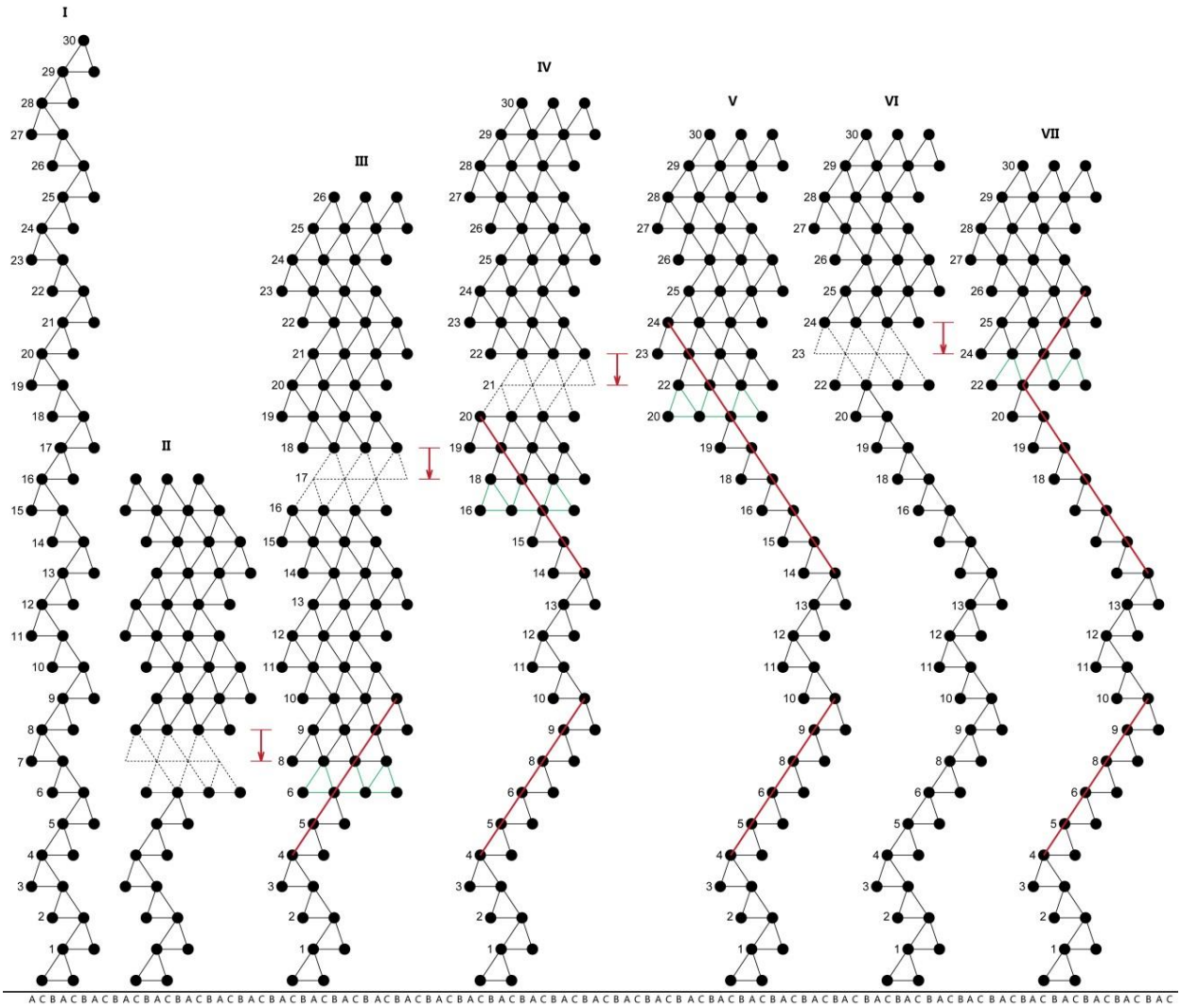

Figure 10.6 Transformation of the 4H-SiC stacking from perfect (22) stacking sequence to (50) and (63) faulted stacking sequences. Refer to text for details on transformation steps.

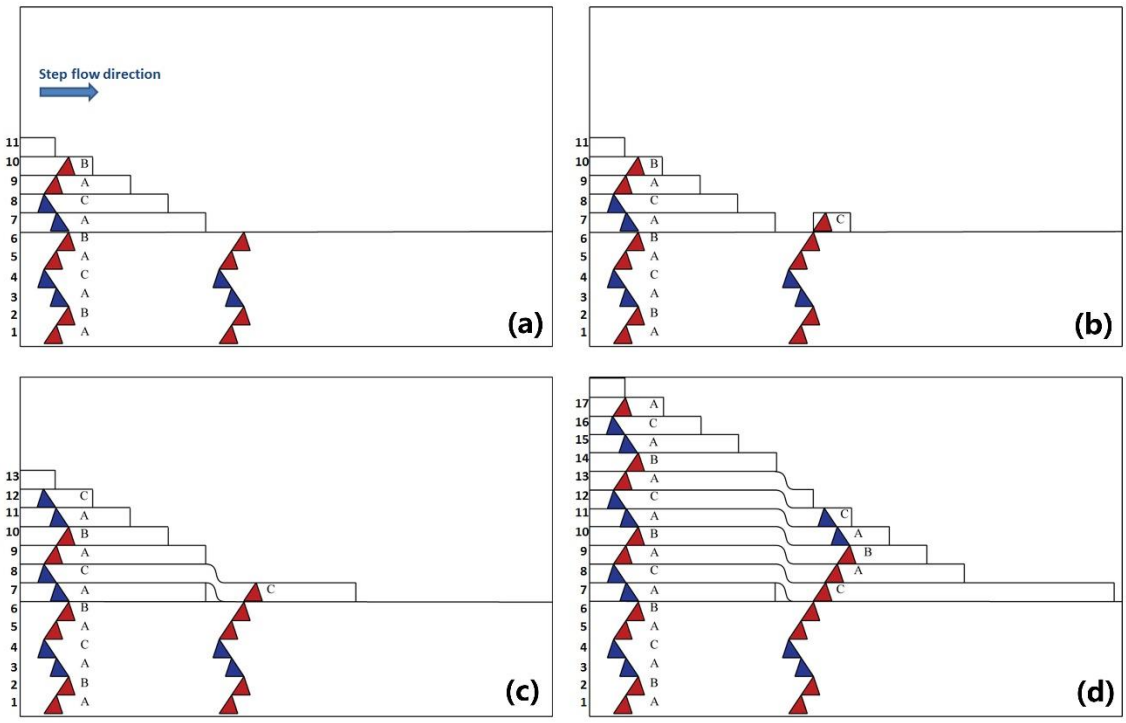

Figure 10.7 2D nucleation and step-flow process to form (50) stacking fault: (a) Step-flow condition at the growth front; (b) 2D nucleation of one SiC bilayer of the wrong stacking sequence; (c) Layer 8 merging into the 2D crystal; (d) generation of (50) stacking sequence

11. A Method to Determine Fault Vectors from Stacking Sequences

11.1 Outline

A new method has been developed to determine the fault vectors associated with stacking faults in 4H-SiC from their stacking sequences observed on High Resolution TEM images. This method, analogous to the Burgers circuit technique for determination of dislocation Burgers vector, involves determination of the vectors required in the projection of the perfect lattice to correct the deviated path constructed in the faulted material. Results for several different stacking faults were compared with fault vectors determined from X-ray topographic contrast analysis and were found to be consistent. This technique is expected to be applicable to all structures comprising corner shared tetrahedra.

11.2 Introduction

In 4H-SiC, like other polytypes of this material, low stacking fault (SF) energies can lead to a tendency to form SFs on the basal plane. In fact, this tendency can be thought of as contributing to SiC's inherent property of polytypism. The relative complexity of the 4H-SiC structure means that SF configurations can be correspondingly more complex than the Shockley, and intrinsic and extrinsic Frank type faults encountered in simpler close-packed structures [46]. In 4H-SiC, which in perfect single crystal form has a stacking sequence of (22) (according to the Zhadnov notation), the stacking sequences associated with the various SFs can be readily studied using HRTEM of {11-20} cross sectional samples. Observations of the (31) stacking sequence for Shockley faults and the (50) stacking sequence for intrinsic Frank faults have been reported. The former was created by glide of partial dislocations in response to the applied stresses in the crystal below the brittle to ductile transition temperature (BDT) [39] or through recombination-enhanced motion during device operation [44] and the latter is formed by misalignment of stacking sequences when step spirals associated with threading screw dislocations meet vicinal steps during homo-epitaxial growth [64]. The corresponding fault vectors are $\boldsymbol{s}$ and $\boldsymbol{c}/4$ respectively. Here, $\boldsymbol{s}$ corresponds to 1/3<-1100> and $\boldsymbol{c}$ corresponds to <0001>. In addition, it has been predicted that c/2 intrinsic Frank fault should have a (11) stacking sequence and -c/4 extrinsic Frank fault should have a (41) or (14) stacking sequence [22], although they have not been observed yet. In addition, many other faulted stacking sequences have been observed in 4H-SiC using HRTEM, such as the (60) double Shockley fault [58], the (44) 8H fault [61], and the (30) faults associated with carrot defects [52]. The fault vector associated with carrot defects has been reported to be $\boldsymbol{s}+\boldsymbol{c}/4$ [65].

Fault vectors associated with SFs can also be studied using X-ray topography contrast analysis. For example, our recent studies have revealed that double and single Shockley faults exhibit the same contrast behavior on SWBXT images [107], which suggests that, in general, the fault vector could be n$\boldsymbol{s}$, where n is any integer but not zero. In addition, our recent SWBXT studies of SFs have revealed several SFs with fault vectors comprising mixtures of $\boldsymbol{s}$ and $\boldsymbol{c}/4$ (or $\boldsymbol{c}/2$) [82-84].

In this part of the work, HRTEM observations of the novel stacking sequences associated with these latter faults will be reported. Since a lot of information regarding the stacking sequences and fault vectors of these various SFs has been compiled, consideration has been

made of how to build the connection between the stacking sequences observed on {11-20} cross sectional HRTEM samples and the contrast behavior of the corresponding faults on synchrotron x-ray topographs. In order to achieve this, it becomes necessary to be able to determine the fault vector based on the two dimensional projection of the stacking sequence as portrayed on the HRTEM images recorded with <11-20> zone axes.

One way to obtain the fault vector based on the observed stacking sequence is to construct a Burgers circuit [46] encircling the leading partial dislocation associated with the fault. However, two problems may impede the implementation of this plan. First, a good image of the stacking sequence around a partial dislocation might not be always easy to obtain; second, which is more related to the current topic, constructing Burgers circuits in a complicated structure like 4H-SiC is not as straightforward as in cubic structures. In this part of the work, the report is made for a technique that can directly deduce fault vector based on stacking sequences observed on {11-20} cross sectional HRTEM images.

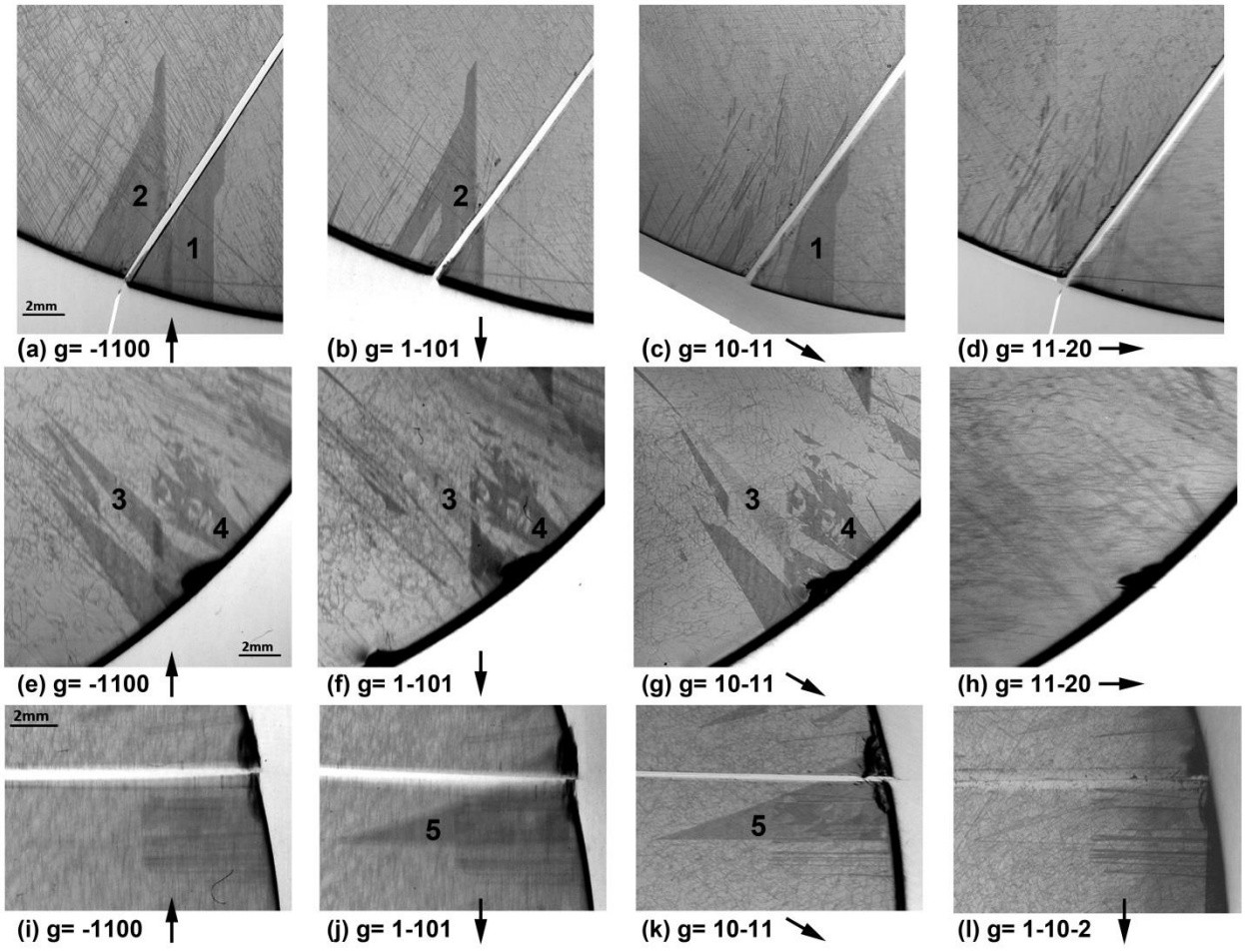

Figure 11.1 SWBXT images recorded from a PVT-grown 4H-SiC basal wafer (with 4° offcut): (a)-(d) contrast behavior of SF #1 and #2, where SF #1 is invisible in 1-101, 11-20 reflections and SF #2 is invisible in 10-11, 11-20 reflection; (e)-(h) contrast behavior of SF #3 and #4, where SF #3 shows weak contrast in 1-101, 10-11 reflections and no contrast in 11-20 reflection and SF #4 shows no contrast in 11-20 reflection; (i)-(l) contrast behavior of SF #5, where SF #5 is invisible in -1100 and 1-10-2 reflections

11.3 Characterization

PVT-grown, offcut (0001) 4H-SiC wafers were initially studied using SWBXT. Using g.R analysis, five types of SF were observed, having fault vectors of ***s***, ***c***/2, ***s***+***c***/2, ***s***+***c***/4 and -***s***+***c***/4. Their contrast behavior is shown in Fig. 11.1 and their g.R calculations are summarized in Table 8.

Table 8 g·R calculation for Fault 1 to 5

g.R (g \ R)	-1100	1-101	10-11	11-20	1-10-2
Fault 1, -***s***+***c***/4 (or 1/12<4-403>)	-2/3	11/12	7/12	0	/
Fault 2, ***s***+***c***/4 (or 1/12<-4403>)	2/3	-5/12	-1/12	0	/
Fault 3, ***s***+***c***/2 (or 1/6<-2203>)	2/3	-1/6	1/6	0	/
Fault 4, ***s*** (or 1/3<-1100>)	2/3	-2/3	-1/3	0	/
Fault 5, ***c***/2 (or 1/2<0001>)	0	1/2	1/2	/	-1

The fault vector is the displacement vector associated with the SF. The dot product between the reflection vector and the fault vector, **g**.**R**, is utilized in the X-ray topographic contrast analysis or low magnification TEM images of SFs and constitutes the phase shift experienced by the X-ray wavefields [92] or electron Bloch waves as they cross the fault plane [77]. Contrast from SFs is expected to disappear when g ⋅R is equal to an integer (including zero) and is expected to be very weak (almost invisible) when g ⋅R equals to ±1/12 or ±11/12. Contrast should be weak but visible when g ⋅R equals to ±1/6 or ±5/6 and well-marked when g ⋅R equals to ±1/2, ±1/3, or ±2/3. These criteria enable fault vectors to be determined, but solutions obtained may not be unique. For example, for the case of fault #2 above, -***s***-***c***/4, ***s***-3***c***/4, -***s***+3***c***/4, 2***s***-***c***/4, -2***s***+***c***/4, 2***s***+3***c***/4 and -2***s***-3***c***/4 are all possible solutions for the fault vector in addition to ***s***+***c***/4. Each of these corresponds to the Burgers vector of a possible partial dislocations associated with the SF. Therefore, ***s***+***c***/4, which has the smallest vector magnitude, actually represents a group of equivalent fault vectors (***s***+***c***/4+n***a***+m**c**) in terms of contrast behavior. Here ***a*** corresponds to 1/3<11-20>, and n, m could be any integer. The specific Burgers vector of the partial dislocation associated with SF can be determined by applying the **g**.**b**=0 and **g**.**b**x**l**=0 criteria for contrast extinction [76], which generates a unique solution (provided all necessary reflections are accessible based on the sample geometry).

{11-20} cross sectional HRTEM studies have been carried out on faults #1, #2, #3 and #5. Their stacking sequences are observed to be (333), (33333), (32223) and (33) respectively, as shown in Fig. 11.2. Based on these observed stacking sequences, it can be speculated that very thin layers of 6H polytype have been nucleated during crystal growth. However, since the thicknesses of these layers are limited to several atomic layers they merely constitute faulted regions in the 4H lattice.

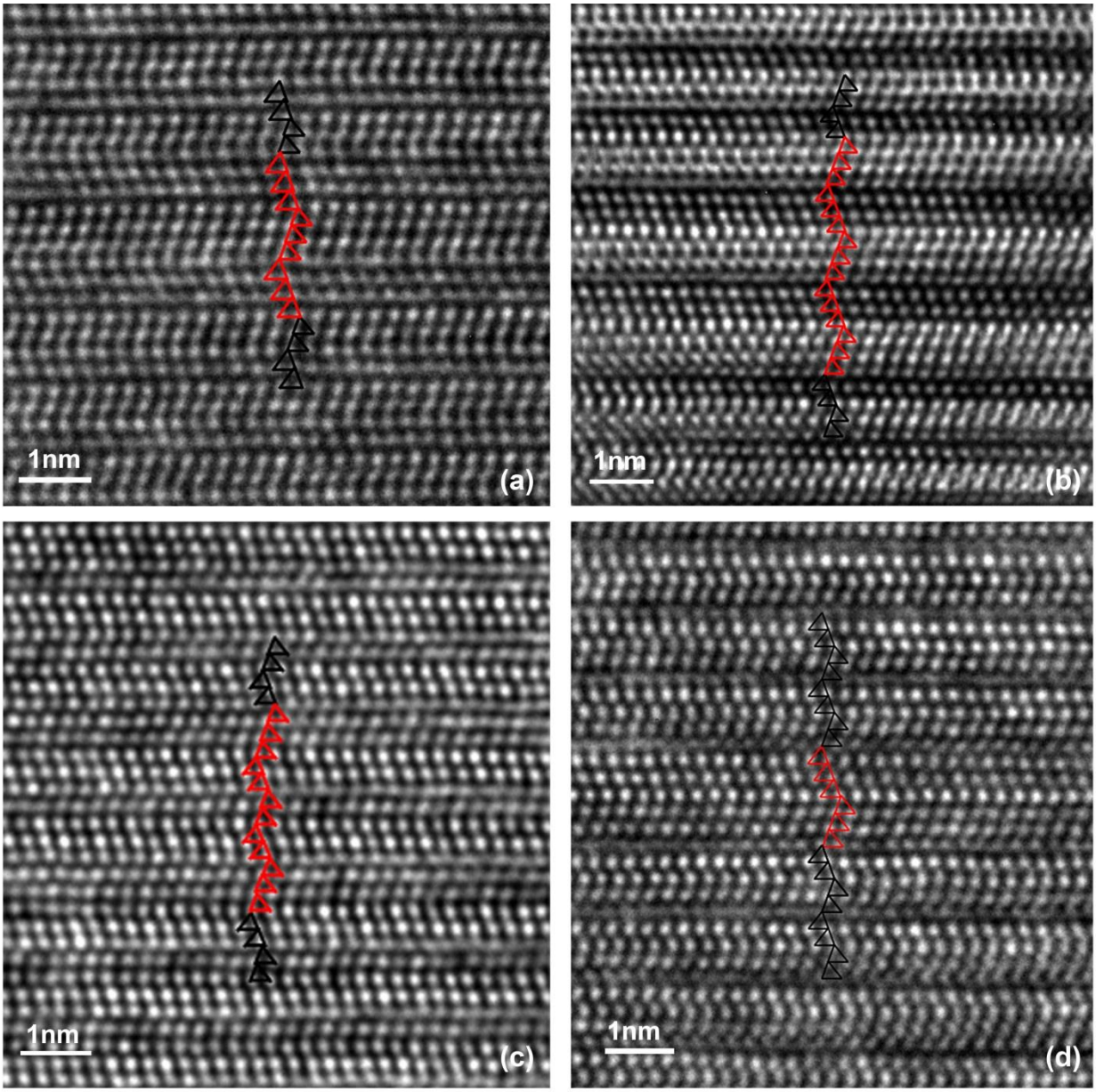

Figure 11.2 HRTEM images recorded from {11-20} cross sectional samples: (a) (333) stacking sequence of fault #1; (b) (33333) stacking sequence of fault #2; (c) (32223) stacking sequence of fault #3; (d) (33) stacking sequence of fault #5

11.4 Technique

It would be natural at this point to consider the potential connections between stacking sequences observed on {11-20} cross section HRTEM images and fault vectors as determined by X-ray topographic contrast analysis. It particularly is interesting to explore whether there is a way to directly determine the fault vector based on the stacking sequence observed on the HRTEM images. One idea is inspired by the Burgers Circuit method to determine the Burgers vector of a dislocation [46]. To determine Burgers vector, a circuit is drawn in the distorted

material lattice around a dislocation line, and then the same point to point movements are repeated in the perfect lattice. The vector required to close the circuit in the perfect lattice is the Burgers vector. In our case, some adjustments are made in order to determine fault vectors. First, instead of drawing a closed loop around the defect, a one-way path across the faulted region is drawn in the distorted material lattice, starting from a good region and ending in a good region. Then, one attempts to repeat the point to point movements of the same path in the perfect lattice. Evidently, the path will deviate from the perfect lattice at some point. Every time the path deviates from the perfect lattice and cannot continue, we use a vector (as small as possible) to correct the path, in other words, to connect the path to next point of movement. For the overall operation, we use a minimum of vectors to correct the path. After completing the path, we simply sum all the vectors used to correct the path to get the fault vector of the SF.

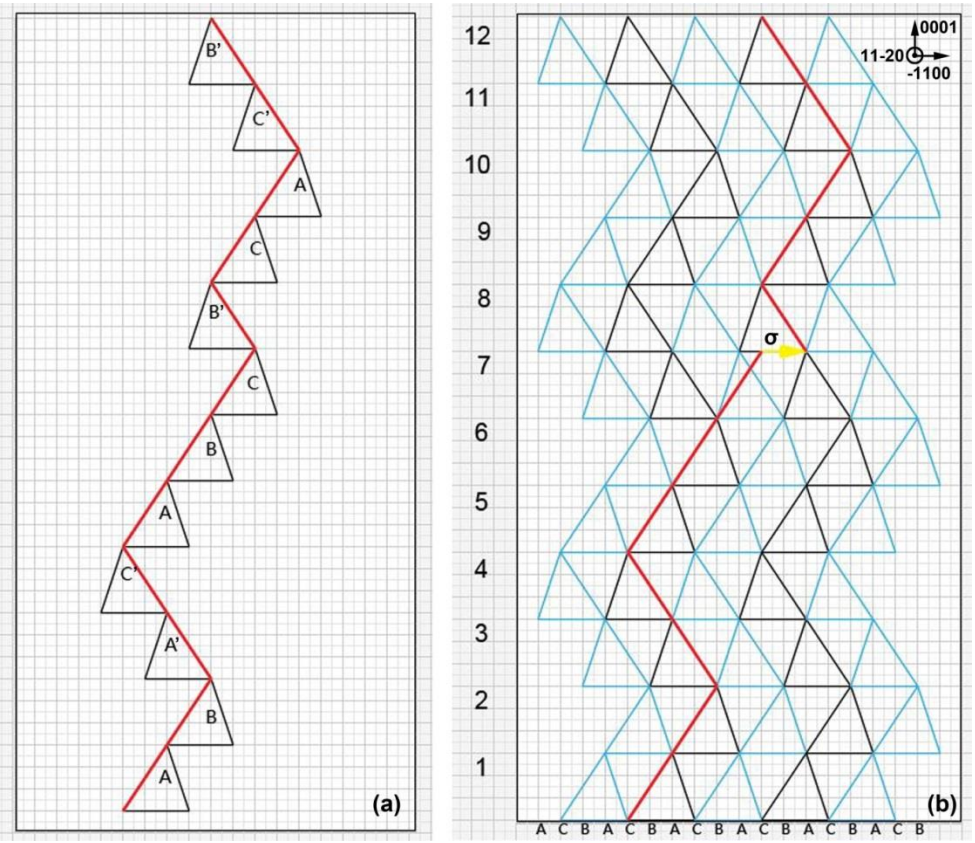

Figure 11.3 (a) (31) stacking sequence of Shockley fault in 4H-SiC lattice; (b) deviated lattice path of (31) Shockley fault

A Shockley fault has a (31) stacking sequence, as schematically shown in Fig 11.3(a). To get the fault vector based on (31) stacking sequence using our proposed technique, first, a {11-20} projection of the corner shared tetrahedra that comprise the perfect 4H-SiC lattice is drawn like the one shown in the background of Fig 11.3(b). Possible stacking positions of the projected tetrahedra are represented as the letters A, B, and C at the bottom of the figure. Layer numbers for the sheets of tetrahedra are represented by the numbers on the left of the diagram. In 4H-SiC the tetrahedra have a stacking sequence of ABA'C' (where a prime sign denotes a twinned tetrahedron) [93], or (22) in Zhadnov notation. The black triangular projections of the tetrahedra

shown on Fig. 11.3(b) have their long edges in the plane of the figure, while the long edges of the blue ones are on adjacent {11-20} planes above or below the plane of the diagram. Two thirds of the length of the base of each triangle is equal to the magnitude of the vector ***s***, which is explained in Fig 11.4 which shows an 0001 projection of the stacking positions. The height of each triangle is equal to the magnitude of the vector 1/4***c***.

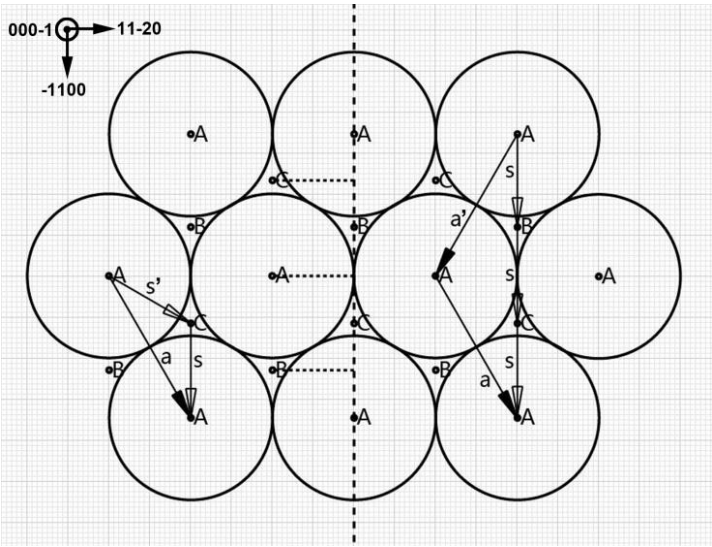

Figure 11.4 0001 projection of stacking positions

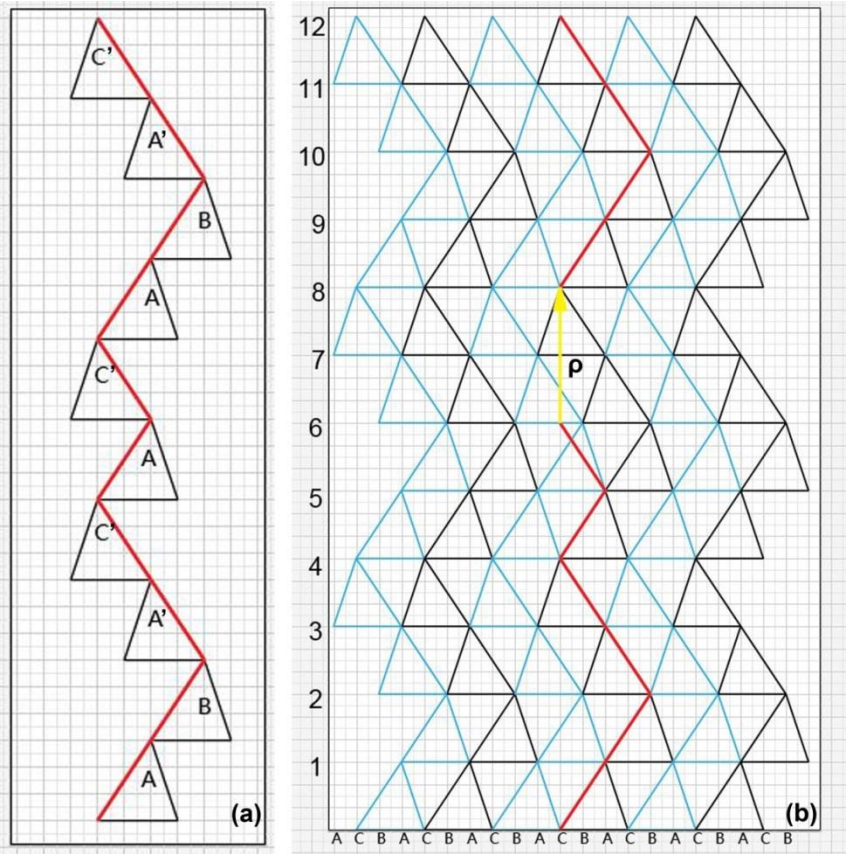

Figure 11.5 (a) (11) stacking sequence of c/2 intrinsic Frank fault in 4H-SiC lattice; (b) deviated lattice path of (11) c/2 Frank fault

Next, the path comprising long edges of the connected tetrahedra across the SF may be drawn like the one in red shown in Fig. 11.3(a). Then, one attempts to superimpose the exact same path on the perfect lattice as shown in Fig. 11.3(b), in which the movements are drawn from bottom to top and marked in red. At layer 7, the path deviates from the perfect lattice. In order to continue the deviated path of the SF on the same {11-20} plane (i.e. along the long edges of the same-color triangular projections), a vector $\boldsymbol{\sigma}$, marked in yellow, is needed to correct the path. $\boldsymbol{\sigma}$ is equal to the vector $\boldsymbol{s}$ demonstrating that this is a Shockley fault.

To determine the fault vector of an intrinsic Frank fault with (11) stacking sequence (Fig. 11.5(a)), a deviated path through the faulted stacking sequence is drawn in Fig. 11.5(b). At layer 6, the path is deviated from the perfect lattice. In order to continue the path in the same {11-20} plane, a vector $\boldsymbol{\rho}$ is needed to connect the path to the next point on the deviated path. Here, $\boldsymbol{\rho}$ is equal to the vector $\boldsymbol{c}/2$. In a similar way one can use the same technique to determine the vector required to correct the deviated path of the (50) stacking sequence which Fig. 11.6 shows is equal to $\boldsymbol{c}/4$. In summary, it has been shown that the technique of plotting and correcting the deviated path through the faulted stacking sequence works for the Shockley fault, the c/2 intrinsic Frank fault, and the c/4 intrinsic Frank fault.

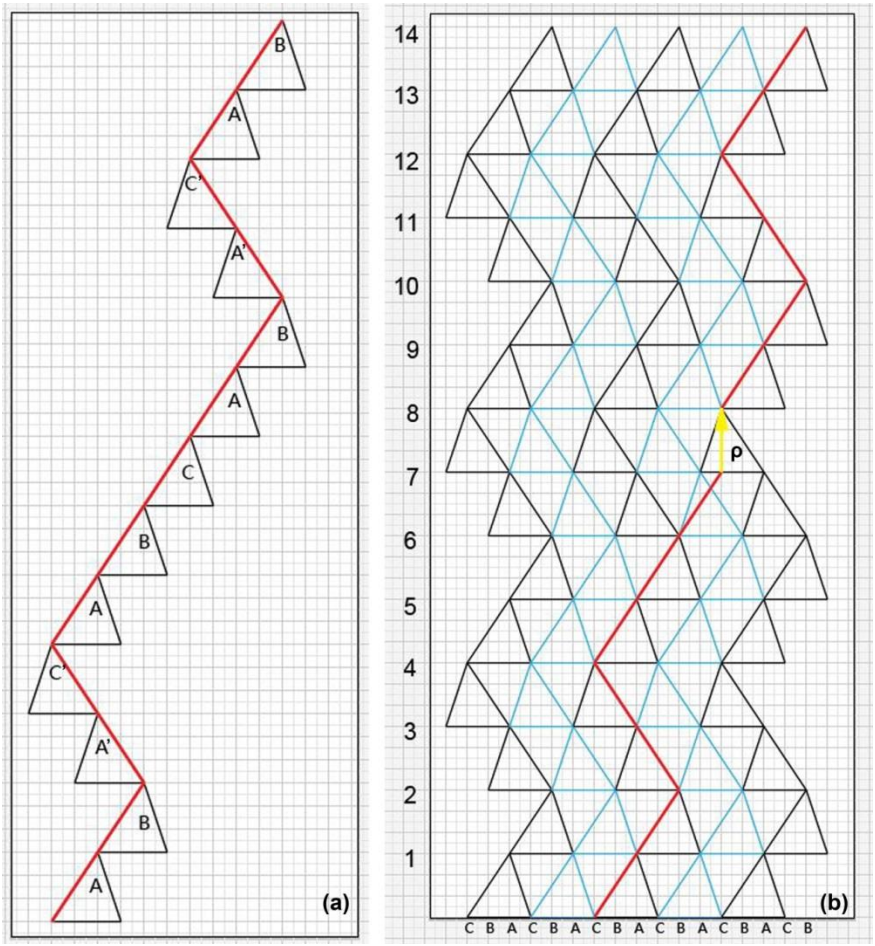

Figure 11.6 (a) (50) stacking sequence of c/4 intrinsic Frank fault in 4H-SiC lattice; (b) deviated lattice path of (50) c/4 Frank fault

Now, we can apply the same technique to the stacking sequences observed in Fig. 11.2. The faulted path of (333) stacking sequence are shown in Fig. 11.2(a). In Fig. 11.7, three vectors are required to fix the drawing of deviated lattice path of stacking sequence. $\boldsymbol{\sigma}1$ at layer 7 and $\boldsymbol{\sigma}2$ at layer 12 are equal to $\boldsymbol{s}$; $\boldsymbol{\rho}$ at layer 9 is equal to $1/4\boldsymbol{c}$. The sum of the used vectors is $2\boldsymbol{s}+\boldsymbol{c}/4$, which is equivalent to a fault vector of $-\boldsymbol{s}+\boldsymbol{c}/4$, since $3\boldsymbol{s}=\boldsymbol{a}+\boldsymbol{a}'$ (explained in Fig. 11.4). This result is consistent with the results of our SWBXT contrast analysis discussed above.

The faulted path of (33333) stacking sequence is shown in Fig. 11.2(b) and the vectors used to fix the drawing of deviated path on the perfect lattice in Fig. 11.8 are $\boldsymbol{\sigma}1=\boldsymbol{\sigma}2=\boldsymbol{\sigma}4=\boldsymbol{s}$, $\boldsymbol{\sigma}3=-\boldsymbol{s}$, and $\boldsymbol{\rho}1=\boldsymbol{\rho}2=\boldsymbol{\rho}3=1/4\boldsymbol{c}$. The sum of the vectors used is 2s+3c/4, which is equivalent to a fault vector of $\boldsymbol{s}+\boldsymbol{c}/4$. One might notice that at level 22, vector $\boldsymbol{\sigma}5$, smaller than $\boldsymbol{\sigma}4+\boldsymbol{\rho}3$, could be used to connect the deviated path to the next movement. However, if choosing to do that, one would end up using more vectors to finish the remaining (22) stacking sequence. Similarly, the vectors used in fixing the deviated lattice path for (32223) stacking sequence (Fig. 11.2(c)) are summed up to be $\boldsymbol{s}+\boldsymbol{c}/2$, as shown in Fig. 11.9. Sum of the vectors used in fixing the deviated lattice path for (33) stacking sequence (Fig. 11.2(d)) is equal to $\boldsymbol{c}/2$, as shown in Fig 11.10. Again, all these results agree with our results of our SWBXT studies discussed above.

For some research purposes, it could be interesting to know how to artificially transform the original stacking sequence of a material to the faulted stacking sequence by operations like eliminating one or several bilayers or shifting layers of tetrahedra from untwinned to twinned [93]. From another point of view, it could be interesting to speculate how the SF adjusts itself and merges into the perfect stacking sequence. One possible solution is provided by the technique above, using the vectors that were used to fix the deviated lattice path. The operations are opposite to the directions of the vectors used to fix the path, which means if vector $\boldsymbol{c}/4$ is used to fix the path, then one deletes a bilayer, or if a vector $\boldsymbol{s}$ is used to fix the path, then use the opposite vector $-\boldsymbol{s}$ to make atoms glide from stacking position C to B, B to A, A to C (if vector $-\boldsymbol{s}$ is used to fix the path, then use the opposite vector $\boldsymbol{s}$ to make atoms glide from stacking position C to A, B to C, A to B). Take (333) stacking sequence (Fig. 11.2(a) & Fig. 11.7) for example, as shown in Fig. 11.11. The perfect 4H-SiC has a stacking sequence of ABA'C' (Fig. 11.11, Column I). At layer 7, the transformation of vector $-\boldsymbol{s}$ make the atoms glide from stacking position A to C, while the tetrahedron changes from the twinned to the untwinned, as shown in Fig. 11.11, Colum II. Then, eliminate layer 9, as shown in Fig. 11.11, Colum III-V. At layer 12, another transformation of vector $-\boldsymbol{s}$ make the atoms glide from stacking position B to A, as shown in Fig. 11.11, Colum VI and eventually, we obtain (333) stacking sequence. It is necessary to point out that the same structure will be obtained no matter which operation goes first. That's to say, the same (333) stacking sequence will be created if we would like to delete layer 9 first and then apply the transformation of vector $-\boldsymbol{s}$ at layers 12 and 7.

Finally, there might be more than one way to do the transformation for a faulted stacking sequence and the suggested operations by the technique above may or may not be the most efficient ones. For example, our deviated lattice path technique suggests the (33) stacking sequence (in Fig 11.10) could be transformed from the perfect (22) stacking sequence with four operations: transformation of $-\boldsymbol{s}$ at layer 7, transformation of $\boldsymbol{s}$ at layer 13, and elimination of layers 9 and 12. On the other hand, the (33) stacking sequence could also be obtained by just two operations: deleting layers 7 and 9, as shown in Fig. 11.12. The possibility that a faulted stacking sequence could be obtained through different ways of lattice transformation indicates that more

than one kind of partial dislocation could be associated with the same faulted stacking sequence. The actual SF formation mechanism is determined by growth conditions of the crystal or whatever external stimulus the crystal may have been subjected to.

11.5 Conclusion

The technique of correcting the deviated path through the stacking sequence can be used in 4H-SiC to determine the fault vectors of SFs (or equivalent fault vectors). This technique is also expected to work in other closed packed structures, such as 2H, 3C, 6H, and 15R. It also provides a possible solution to transform the perfect stacking sequence to the faulted one.

For a faulted stacking sequence, the fault vector may not be unique since there could be different approaches to transform the original stacking sequence to the faulted one and more than one kind of partial dislocation could be possibly associated with the SF. Our SWBXT study results, TEM study results, and the technique of deviated lattice path indicate that multiple vector operations on the stacking sequence can used to decide the fault vector, and even the Burgers vectors of the possible partials. In addition to the operations suggested by the technique, one could use the combination of vectors $\boldsymbol{s}$ and $\boldsymbol{c}/4$ to make the transformation in other possible ways and simply sum the vectors to obtain the fault vector, which should be equivalent to the fault vector determined by the technique.

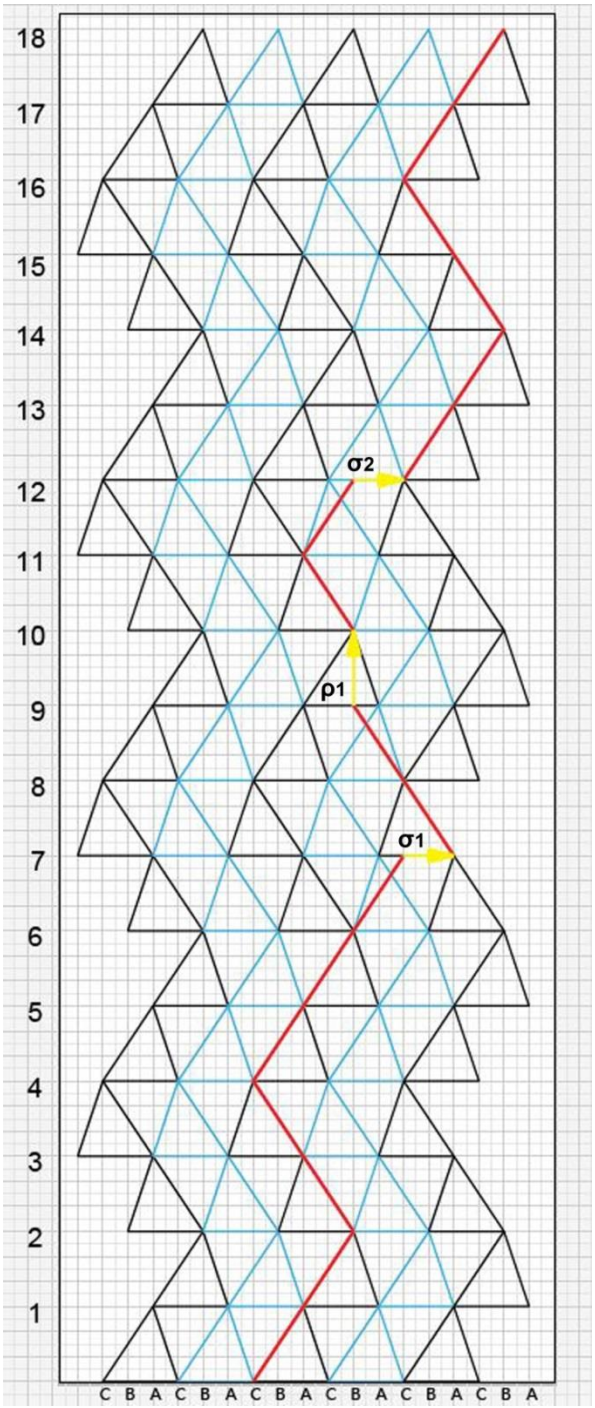

Figure 11.7. Deviated lattice path of (333) fault

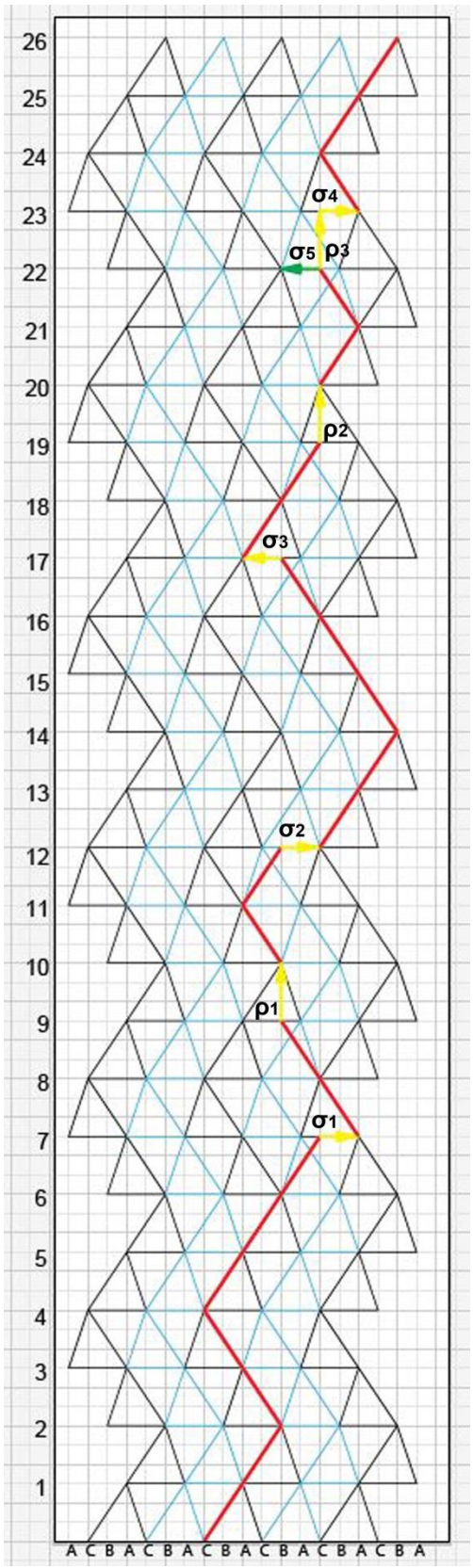

Figure 11.8. Deviated lattice path of (33333) fault

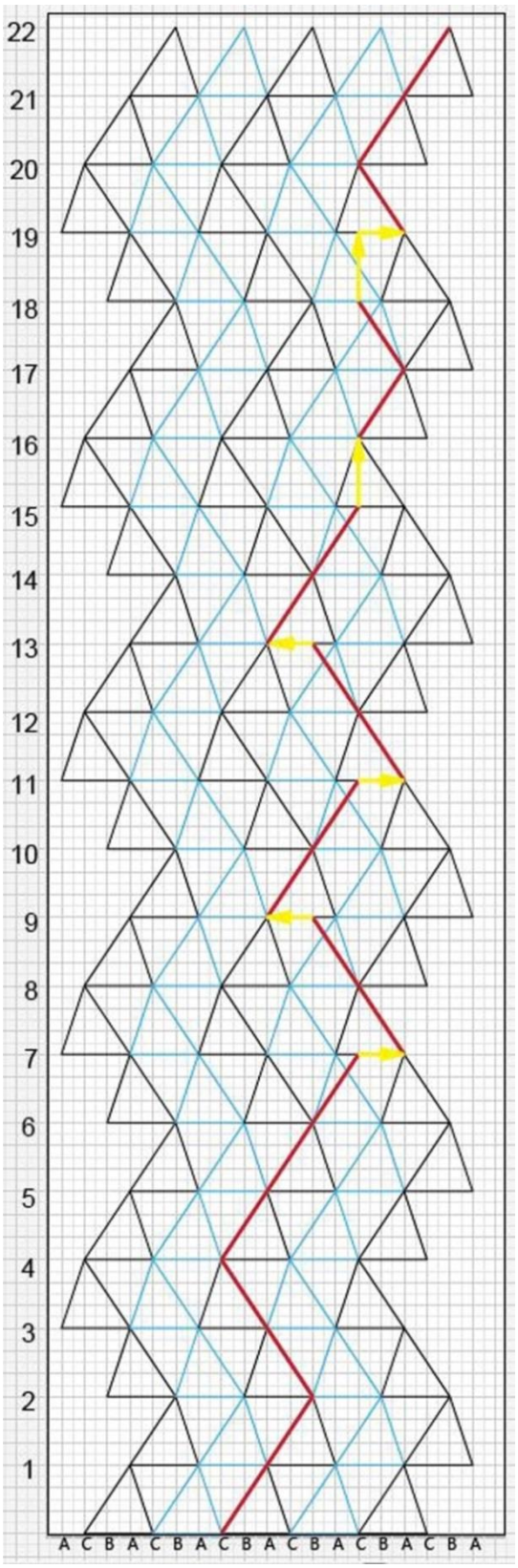

Figure 11.9. Deviated lattice path of (32223) fault

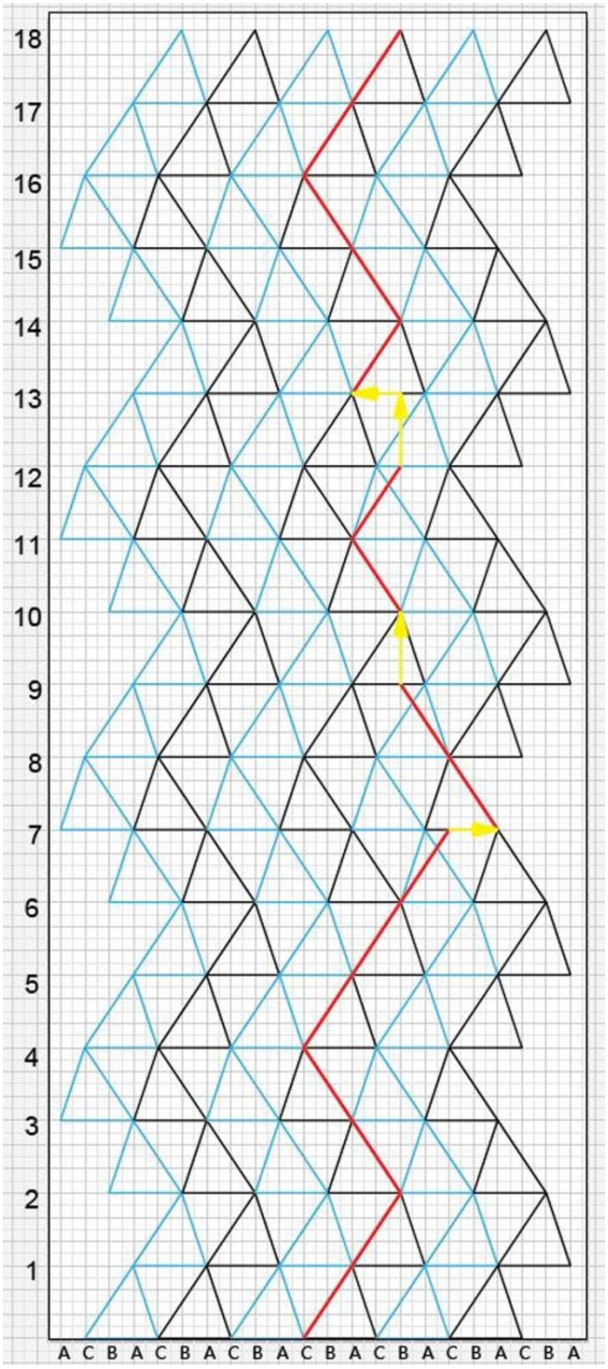

Figure 11.10 Deviated lattice path of (33) fault

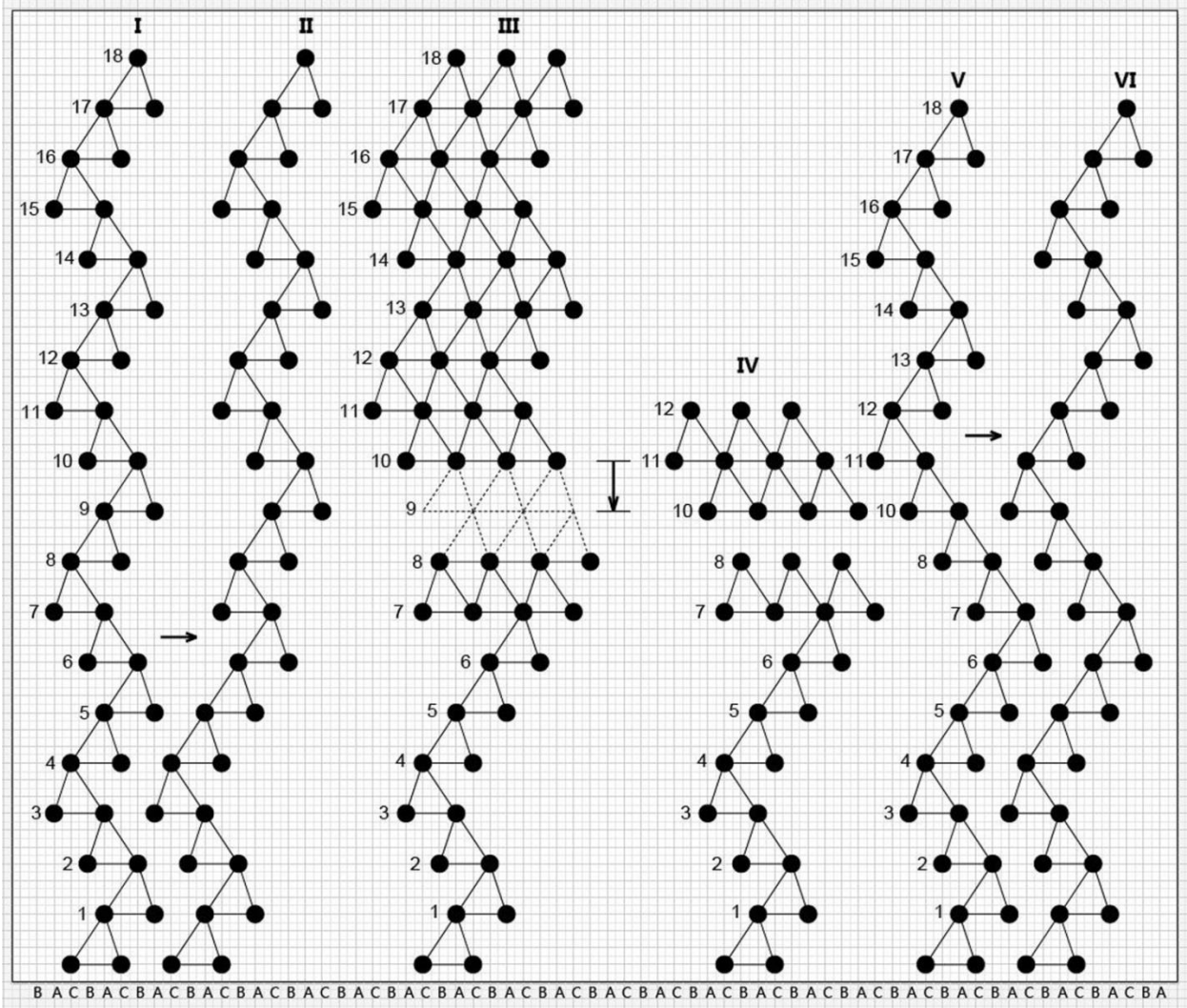

Figure 11.11 Transformation from (22) perfect stacking sequence to (333) faulted stacking sequence

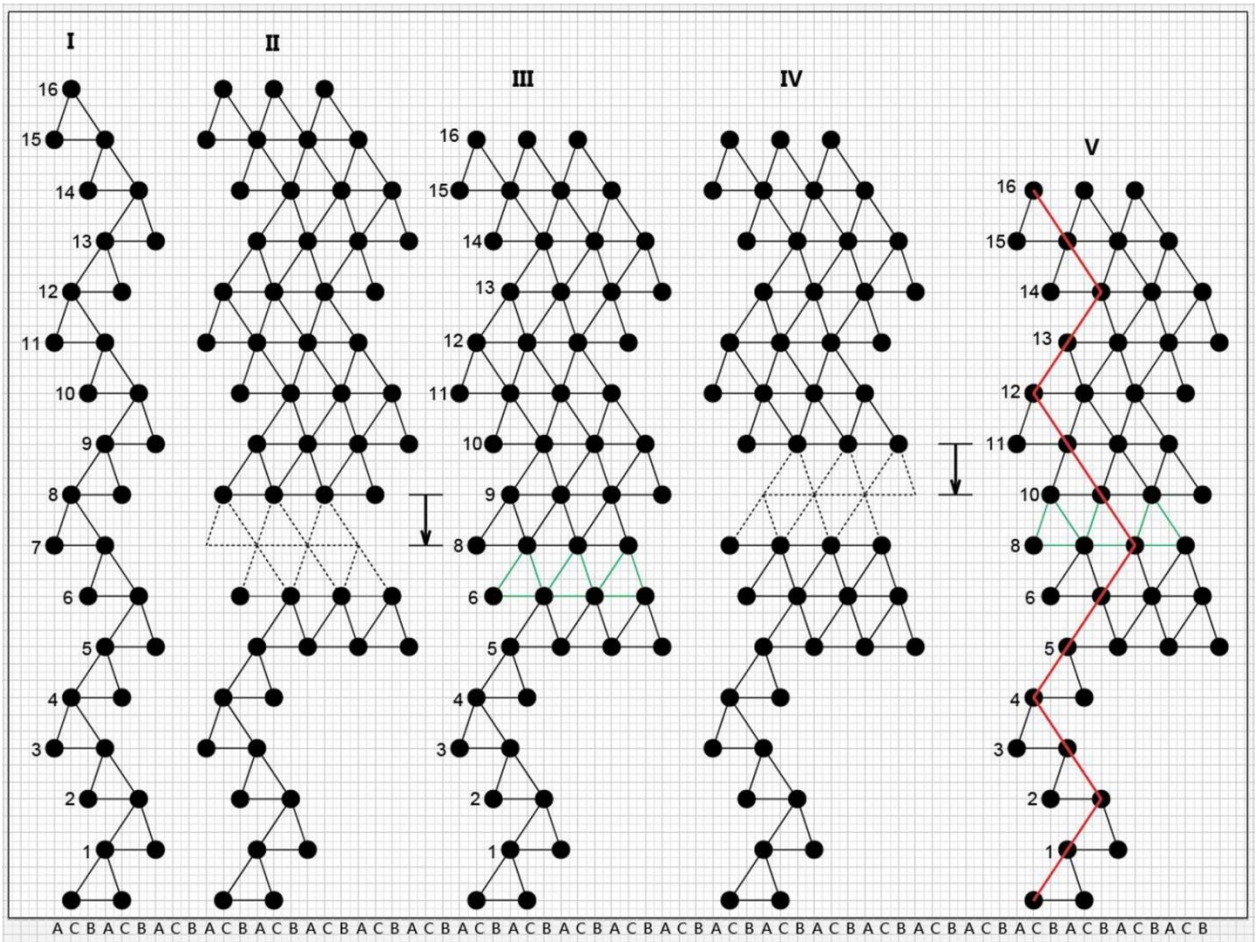

Figure 11.12 Transformation from (22) perfect stacking sequence to (33) faulted stacking sequence

12. Transformation of Stacking Sequence and Formation of stacking faults in 4H-SiC

12.1 Outline

A method has been developed to find the most efficient way to transform the original stacking sequence of 4H-SiC to that of a stacking fault, using operations such as eliminating one or several SiC bilayers or shifting layers of tetrahedra from untwinned to twinned configuration. The (33) fault, the double Shockley fault and the so-called V-shaped defect are used as examples to perform the transformation. This technique is expected to be applicable to all structures comprising corner shared tetrahedra.

12.2 Introduction

An interesting aspect to the study of stacking faults (SFs) is to consider how the perfect lattice can be distorted to form the SFs or how the SFs are accommodated into the perfect structure. In 4H-SiC, whose perfect lattice has (22) stacking sequence (in Zhdanov notation), the glide of a Shockley partial dislocation through the perfect lattice causes a shift in stacking position with vector 1/3<-1100> on the (0001) plane and thus shifts a layer of tetrahedra from untwinned to twinned configuration, leading to the formation of a (31) Shockley fault [93]. Elimination of one SiC bilayer creates the (50) intrinsic Frank fault [64] and induces a distortion of ¼[0001] to the lattice. It is believed that multiple glide of Shockley partial dislocations on neighboring SiC bilayers can create even more complex SF structures. For example, the (60) double Shockley fault can be generated if Shockley partial dislocations glide on two adjacent SiC bilayers [58]. Moreover, glide of Shockley partial dislocations on three neighboring SiC bilayers can create (53) triple Shockley fault and such movement on four neighboring SiC bilayers can create the (44) or 8H fault [62].

In Chapter 11, a technique is introduced to determine the fault vectors associated with SFs in 4H-SiC from their stacking sequences observed on high resolution transmission electron microscopy (HRTEM) images (which is also expected to work in all structures comprising corner shared tetrahedra). Additionally, the technique also provides a solution for how to artificially transform the original stacking sequence of 4H-SiC to the faulted stacking sequence, using operations such as eliminating one or several SiC bilayers or shifting layers of tetrahedra from untwinned to twinned configuration. However, it is also illustrated in Chapter 11 that there could be more than just one way to make the transformation and the suggested operations by the technique may or may not be the most efficient ones. In this part of the work, discussions are brought up for an amended technique that can help to find the most efficient way to make the transformation and examples are used to show how this technique can help to understand SF formation mechanism.

12.3 Technique

The HRTEM image from a {11-20} cross sectional TEM sample of 4H-SiC, Fig. 12.1(a), shows a SF with (33) stacking sequence. A one-way path comprising the long edges of the connected triangular projections of tetrahedra across the SF may be drawn like the one in red shown in Fig. 12.1(b), starting from a perfect region and ending in a perfect region. Then, one can apply the technique introduced in Chapter 11 to repeat the point to point movement of the

same path in the perfect 4H-SiC lattice and the drawing of a deviated path will be like the one shown in Fig. 12.2(a). The vectors used in fixing the deviated lattice path are ***s***, -***s*** and two ***c***/4. Here, ***s*** corresponds to 1/3<-1100> and ***c*** corresponds to <0001>. Therefore, the fault vector is determined to be ***c***/2 and four operations are suggested in order to transform the original (22) stacking sequence to the (33) faulted stacking sequence: shift in stacking position with vector -***s*** at layer 7 and ***s*** at layer 13 and elimination of layers 9 and 12.

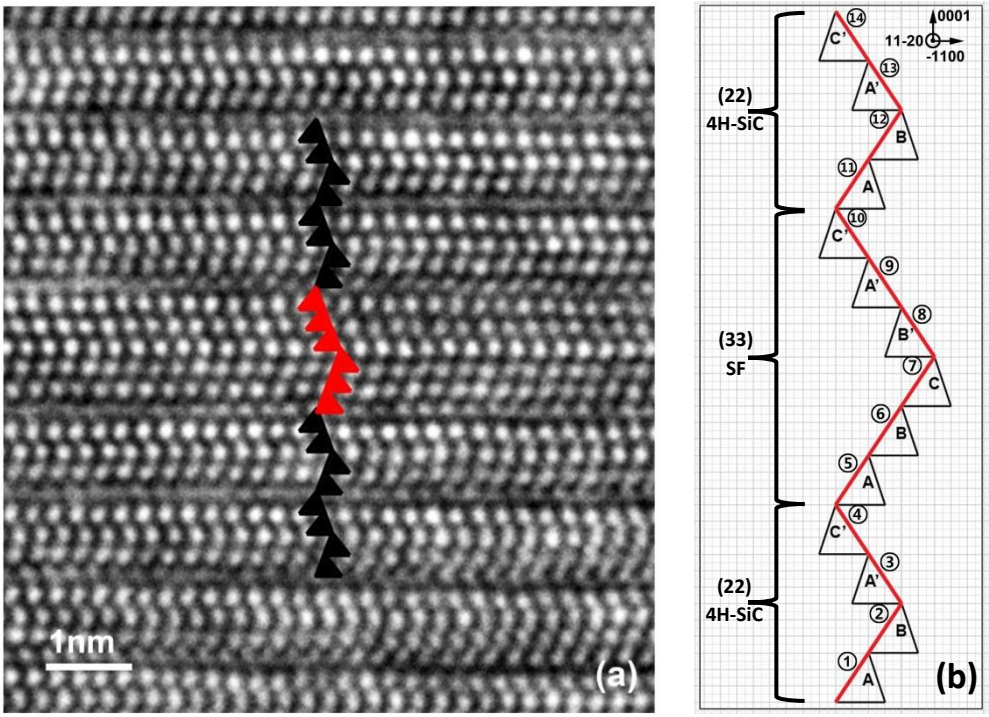

Figure 12.1 (a) HRTEM image of (33) fault recorded from a {11-20} cross sectional TEM sample of 4H-SiC. The red triangles mark the faulted stacking sequence and the black triangles mark the perfect stacking sequence; (b) Schematic diagram of the point to point movement of a path across (33) fault. Fourteen movements are labeled with numbers in circle

However, as suggested in Chapter 11, the (33) stacking sequence could also be obtained by just two operations: deleting layers 7 and 9. The question now is whether the original technique of drawing the deviated path of SF can be amended to provide insight into more efficient operations to transform the stacking sequence. In order to accomplish this purpose, the expression for using the original technique to determine the fault vector must be reorganized and divided into three parts: first, draw a one-way path across stacking fault in the distorted material lattice on 11-20 projection, starting from a perfect region and ending in a perfect region (like Fig. 12.1(b)); second, generate 11-20 projection of the perfect lattice (4H-SiC in our case, like the background in Fig. 12.2 (a)) wherein the point to point movement of the SF path (movement 1 (in circle) to 14 (in circle) in Fig. 12.1(b)) is repeated (like Fig. 12.2(a)). Every time the path deviates from the perfect lattice, use vector ***s*** and/or m***c*** (0<m<1) to connect the deviated path to a nearby lattice point on the same 11-20 plane (i.e. any lattice points at the long edges of the same-color triangular projections in Fig. 12.2(a)) and then continue the path; third, for making

the choice, choose to connect to such a lattice point that the next movement of the path (for example, Movement 8, 10 and 13 in Fig. 12.2(a)) can be along the long edge of the same-color triangular projections.

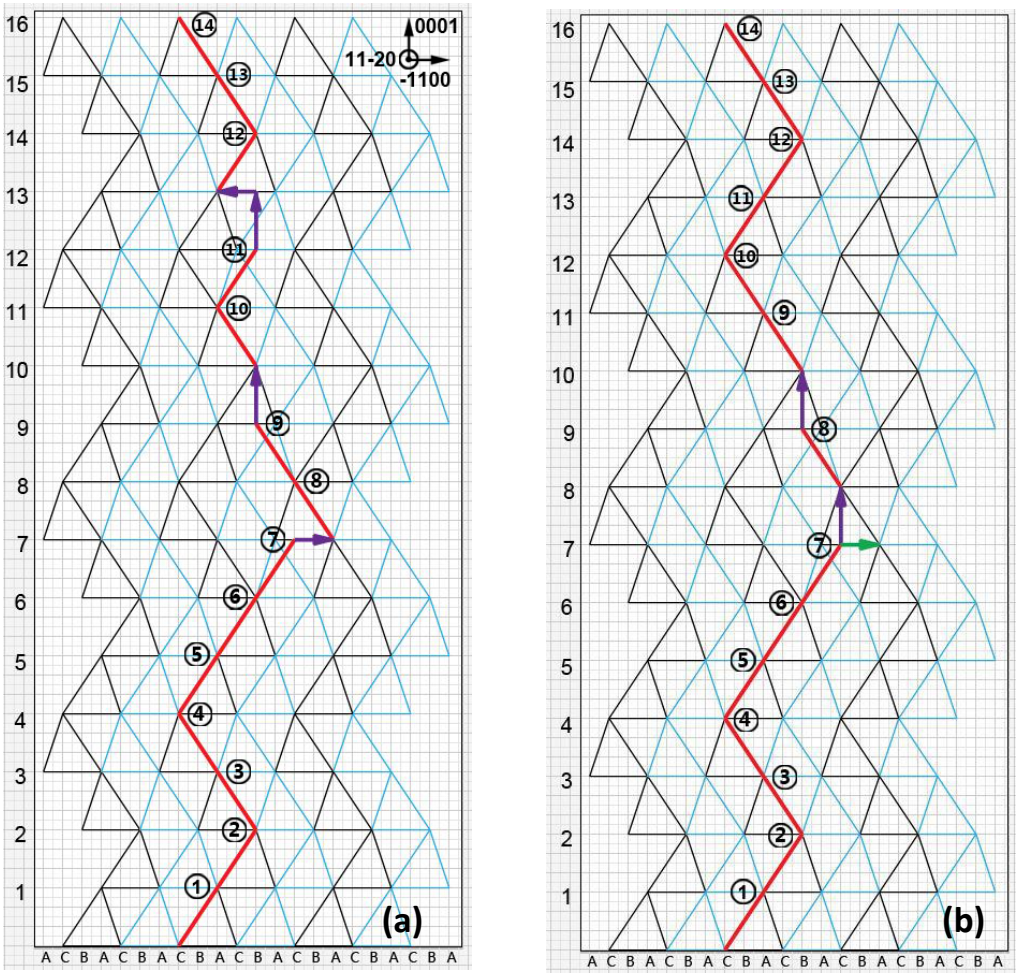

Figure 12.2 Deviated lattice path of (33) fault: (a) vector ***s*** is used at layer 7 to correct the path; (b) vector ***c***/4 is used at layer 7 to correct the path. Possible stacking positions are represented as the letters A, B, and C at the bottom of the figures. Layer numbers for the perfect lattice are represented by the numbers on the left of the diagram.

If only the first two procedures of the technique are applied, there will not be a unique way to repeat the SF path. For example, in Fig. 12.2(b), the path of (33) SF deviates from the perfect lattice at layer 7 and either vector ***s*** (in green) or vector ***c***/4 (in purple) can be used to connect the deviated path to a lattice point nearby on the same 11-20 plane. If vector ***s*** is chosen, the complete deviated path would be drawn like the one shown in Fig. 12.2(a). If vector ***c***/4 is chosen, the complete deviated path would be drawn like the one shown in Fig. 12.2(b). Actually, every time when the SF path is deviated from the perfect lattice, there will be two or more choices that can be made to correct the path. Permutations of these choices lead to all the possible ways to do the drawing of the deviated lattice path, which consequently provide all the possible solutions to transform the original stacking sequence to the faulted one by operations

like eliminating one or several bilayers or shifting stacking positions. For a faulted stacking sequence, there could be many ways to do the transformation and each way to do the transformation leads to a different core structure of the partial dislocation associated with the SF. Which way the SF prefers to accommodate in reality depends on the energy associated with the partial dislocations and also growth conditions of the crystal or whatever external stimulus the crystal may have been subjected to.

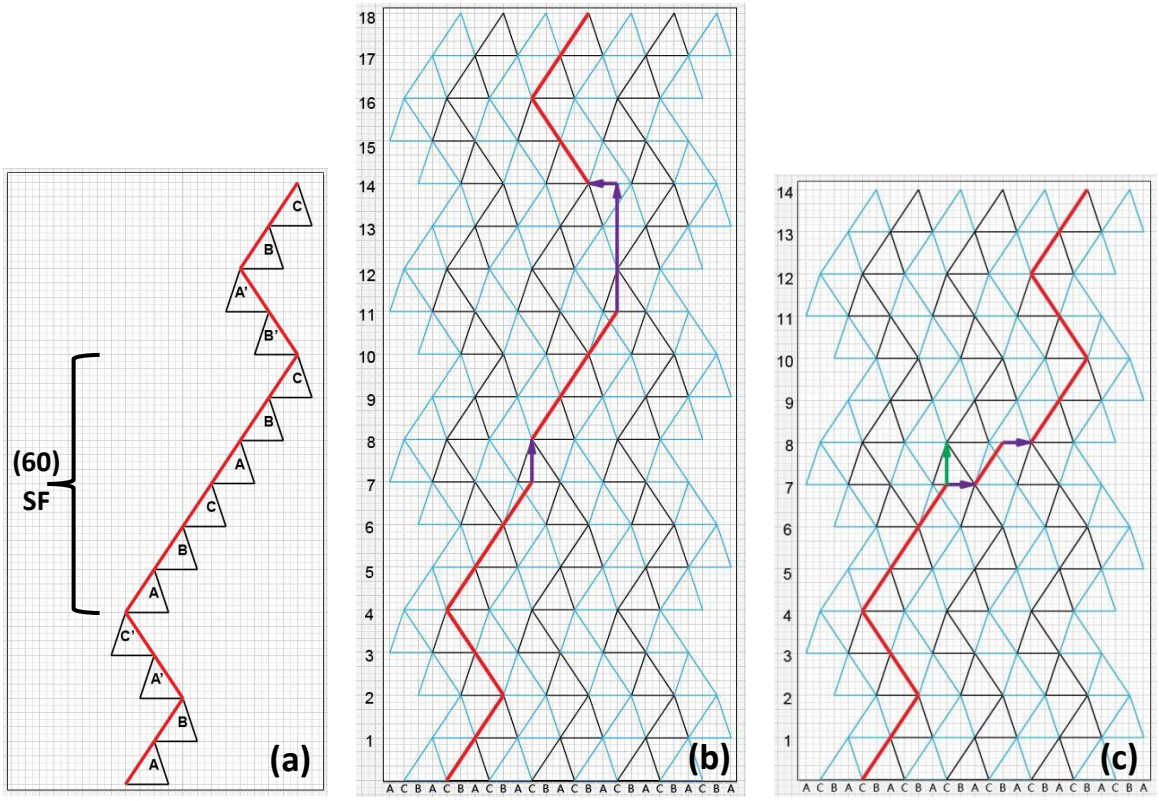

Figure 12.3 (a) Schematic diagram of a path across (60) double Shockley fault; (b) Deviated lattice path of (60) fault. Vector ***c***/4 is used at layer 7 to correct the path; (c) Deviated lattice path of (60) fault. Vector ***s*** is used at layer 7 to correct the path

The third part of the technique makes the drawing of the deviated lattice path unique and can be replaced with different rules to find the most efficient way to do the transformation. For example, the (33) fault has been determined to have a fault vector of c/2 using the original technique and hence an assumption can be made that transformation of vector ***s*** (or -***s***) may not be required to generate the faulted stacking sequence. Therefore, the third part of the technique can be replaced with a new rule that one should only use vectors m***c*** to connect the deviated path to the nearby lattice point. Consequently, the deviated lattice path will be drawn like the one in Fig. 12.2(b). At layer 7 the path deviates from the perfect lattice and a vector ***c***/4 is used to connect the path to the nearby lattice point. Immediately after one more movement (8 in circle), the path deviates from the perfect lattice again at layer 9, and anther vector c/4 is used to correct the path afterwards. Overall, two vectors of ***c***/4 have been used and the new drawing of deviated lattice path suggests that the perfect lattice can be transformed to (33) fault by just eliminating

layers 7 and 9, as the process shown in Fig. 11.12 in Chapter 11. It is necessary to point out that inappropriate rule changes for the third part of the technique can make the drawing of deviated lattice path not performable, which may behave in a way that the drawing can never end without unlimited vectors to correct the deviated path.

The (60) double Shockley fault can be another example to show how to find the most efficient way to do the transformation using the technique. The stacking sequence of the (60) fault is schematically shown in Fig. 12.3(a) and the one-way path across the SF is marked in red. Using the original technique to determine its fault vector, the deviated lattice path will be drawn like the one in Fig. 12.3(b) and the sum of all the vectors used to fix the path is $-\boldsymbol{s}+\boldsymbol{c}$. Recent studies have revealed that double and single Shockley faults exhibit the same contrast behavior on synchrotron white beam x-ray topography (SWBXT) images [107, 108] and $-\boldsymbol{s}+\boldsymbol{c}$ is equivalent to $-\boldsymbol{s}$ in terms of contrast behavior in x-ray topography (as discussed in Chapter 11). Therefore, an assumption can be made that m$\boldsymbol{c}$ may not be necessary in the drawing of deviated lattice path for (60) fault. The third part of the expression can be replaced with a new rule that one should use only vectors $\boldsymbol{s}$ or $-\boldsymbol{s}$ to connect the path to the nearby lattice point. As a result, the deviated lattice path will be drawn like the one shown in Fig. 12.3(c) and thus the suggested operations to transform the perfect stacking sequence to the fault one require shift in stacking position with vector $\boldsymbol{s}$ at two adjacent layers 7 and 8. This result agrees with many discussions in literature about the formation of (60) fault [58, 62].

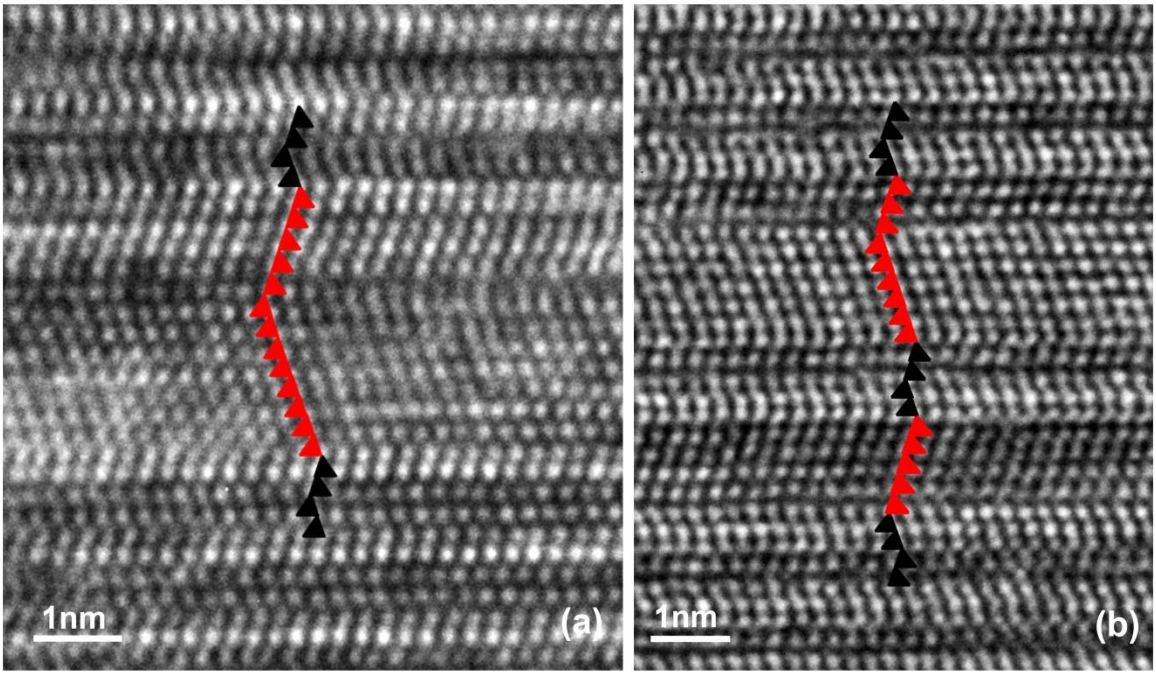

Figure 12.4 HRTEM images of V shaped defects recorded from {11-20} cross sectional 4H-SiC samples: (a) (85) stacking sequence; (b) (50) and (63) stacking sequences

Finding the effective way to transform the perfect stacking sequence to the faulted stacking sequence can help one to explore the SF formation mechanism. In Chapter 10, characterization of a new defect type, called V shaped defects, is presented. SWBXT studies reveal that these defects are actually stacking faults in the 4H-SiC epilayer. HRTEM studies

show that these defects can have (85), (50), and (63) stacking sequences, as shown in Fig. 12.4. Just comparing these three stacking sequences, it is not easy to find their interior correlations, because they are not all similar to any common SiC polytype structures, such as 3C, 6H or 15R. Using the original technique, the fault vectors for (85), (50), (63) stacking sequence are determined to be 3c/4, c/4 and 3c/4 respectively, as shown in Fig. 12.5, 12.6 and 12.7(a). These results are consistent with the fault vectors determined by the SWBXT studies of V shaped defects (see Chapter 10). Since the fault vector of (63) fault doesn't contain an ***s*** component, the third part of the technique can be replaced with a new rule to find the most efficient way to do the transformation for (63) fault that only vectors of type m***c*** can be used to correct the deviated path. As a result, the deviated lattice path for (63) fault will be drawn like the one in Fig. 12.7(b). Fig. 12.5, 12.6 and 12.7(b) reveal the similarity between (85), (50), (63) structures that they can all be transformed from the perfect stacking sequence by one or multiple times elimination of a single SiC bilayer. Following this clue, their formation mechanism was hence proposed in Chapter 10 which suggest that the operation of eliminating one SiC bilayer can be achieved during actual epitaxial growth through 2D nucleation of a single SiC bilayer of wrong stacking position and repetitive 2D nucleation of a single SiC bilayer at different atomic layers leads to the formation of V shaped defects.

12.4 Conclusion

An amended technique of correcting the deviated path through the stacking sequence can be used in 4H-SiC to find the most efficient way to transform the original stacking sequence to the faulted stacking sequence, as well as all the other possible solutions to perform the transformation, using operations like eliminating one or several bilayers or shifting stacking positions with vectors ***s*** (or –***s***). The solutions can be more diverse if it is agreed that eliminating several bilayers within a unit cell height are equivalent to inserting the remaining bilayers. To apply this technique to other structures comprising corner shared tetrahedra, such as 2H, 3C, 6H, and 15R, the 11-20 projection of these structures should be generated and then the drawing of deviated lattice path can be performed.

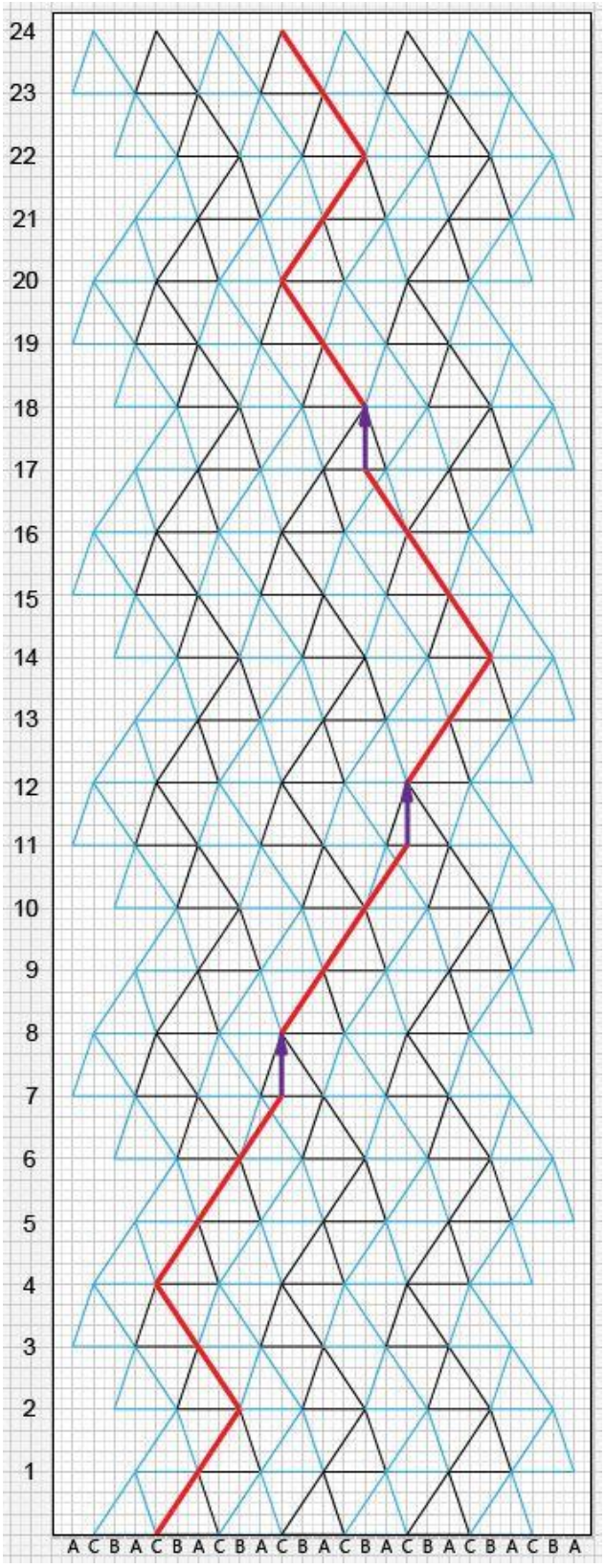

Figure 12.5 Deviated lattice path of (85) fault

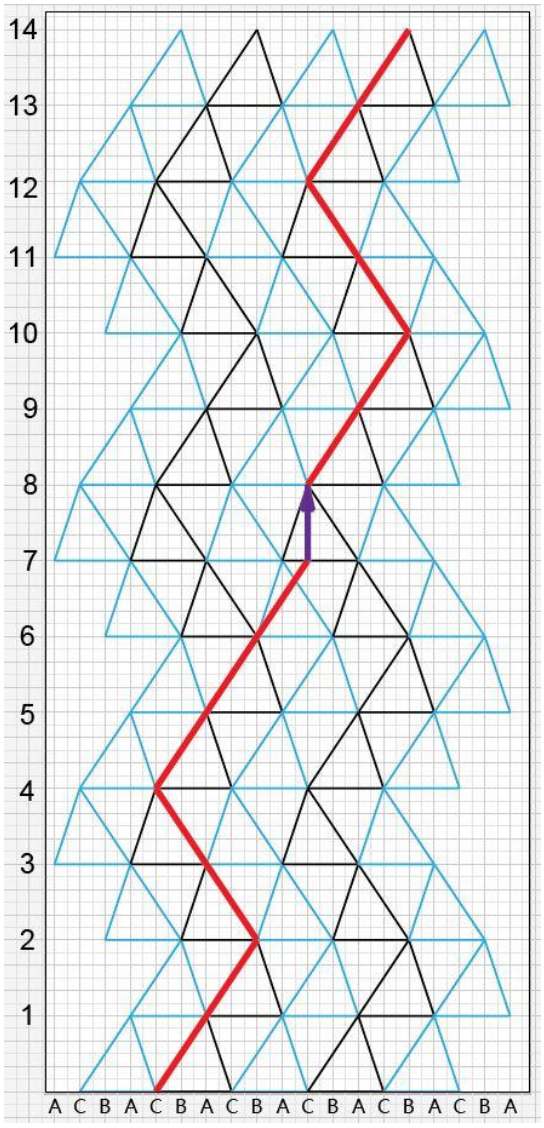

Figure 12.6 Deviated lattice path of (50) fault

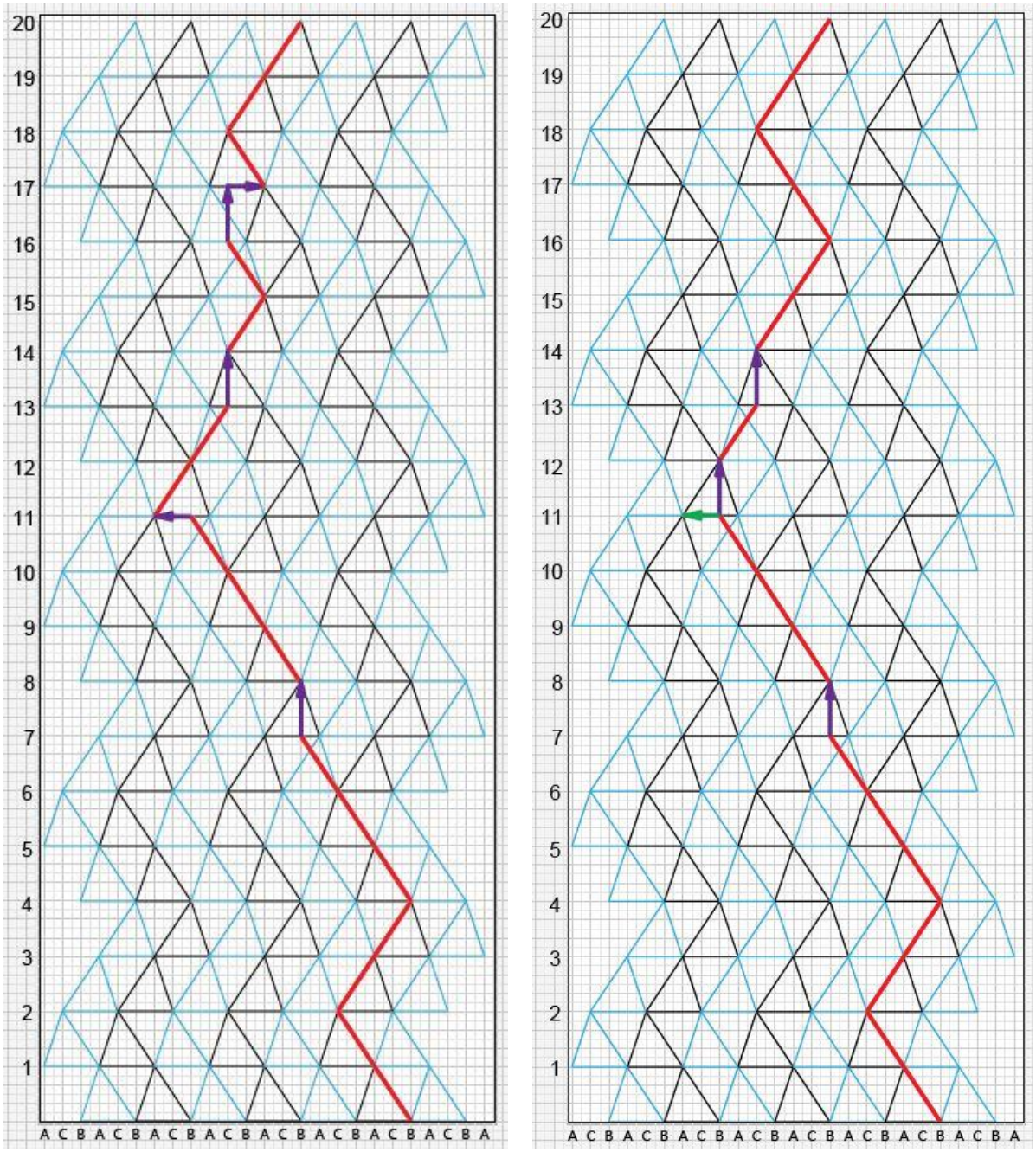

Figure 12.7 Deviated lattice path of (63) fault: (a) vector $-\boldsymbol{s}$ is used at layer 11 to correct the path; (b) vector $\boldsymbol{c}/4$ is used at layer 11 to correct the path

13. Conclusions

Defect structures in 4H silicon carbide (SiC) bulk crystals grown by physical vapor transport (PVT) technique and homoepitaxial layers grown by chemical vapor deposition (CVD) technique been studied using synchrotron x-ray topography, high resolution transmission electron microscopy (HRTEM), chemical etching as well as other characterization techniques.

(1) The existence of threading c+a dislocations in 4H-SiC has been directly revealed using synchrotron white beam x-ray topography (SWBXT). Mutual interactions between threading dislocations with *c*-component of Burgers vector have been observed. Interaction of a non-equilibrium concentration of vacancies with the *c*-component of Burgers vector enable the dislocations to respond to the attractive forces they experience and come together to react. Such interactions can lead to complete or partial Burgers vector annihilation. Among the reactions observed are: (a) the reaction between opposite-sign threading screw dislocations with Burgers vectors **c** and –**c** wherein some segments annihilate leaving others in the form of trails of stranded loops comprising closed dislocation dipoles; (b) the reaction between threading dislocations with Burgers vectors of **-c**+**a** and **c**+**a** wherein the opposite **c**-components annihilate leaving behind the two **a**-components; (c) the similar reaction between threading dislocations with Burgers vectors of **-c** and **c**+**a** leaving behind the **a**-component.

(2) The nucleation and propagation of pairs of opposite sign threading c+a dislocations has been studied. Opposite sign pairs of dislocations with Burgers vector c+a can be generated to accommodate lattice distortion which is induced by the closure failure when growth-steps overgrow inclusions. Once these dislocations are nucleated they propagate along the c-axis growth direction, or can be deflected onto the basal plane by overgrowth of macrosteps. For the c+a dislocations, partial deflection can occasionally occur, e.g. the a-component deflects onto basal plane while the c-component continuously propagates along the growth direction. One factor controlling the details of these deflection processes is suggested to be related to the ratio between the height of the overgrowing macrostep and that of the surface spiral hillock associated with the threading dislocations with c-component of Burgers vector.

(3) Ray tracing simulation has been implemented to simulate the contrast from fourteen different threading dislocations with c-component of Burgers vector in grazing incidence reflections of three different 11-28 types. The contrast from some of the threading c+a dislocations have similar shapes, which makes it difficult to distinguish them from one another. After careful comparison of contrast in all three reflections of 11-28 types, it is possible to unambiguously match the simulated images and the real x-ray topographs for at least two kinds of threading c+a dislocations, e.g. c+180°a, -c+60°a, which in turn can help to interpret the information gathered from X-ray topography.

(4) Observations have been made using SWBXT of stacking faults in PVT-grown 4H-SiC with fault vectors of kind $1/6\langle 20\bar{2}3\rangle$. A mechanism has been postulated for their formation which involves overgrowth by a macrostep of the surface outcrop of a *c*-axis TSD, with two *c*/2-height surface spiral steps, which has several threading CPADs with *c*-height spiral steps which protrude onto the terrace in between the *c*/2 risers. During overgrowth, the *c*/2 step risers give rise to a *c*/2 Frank fault, while the two Shockley partials which result from the overgrowth of the threading CPADs can become separated onto different slip planes such that one becomes mobile

and the other sessile. Should the crystal, while still in the growth chamber, subsequently experience shear stress on the basal plane, the mobile partial will move leading to Shockley fault expansion resulting in a local net fault vector of *c*/2 plus a Shockley, i.e. $1/6<20\bar{2}3>$. Such overgrowth processes deflect the threading dislocations onto the basal plane, enabling them to exit the crystal, effectively reducing the threading dislocation density in the crystal.

(5) Direct observation is obtained of Shockley plus c/4 Frank stacking faults nucleating from a deflected threading c+a dislocation on the basal plane. The x-ray topography contrast from stacking faults on the basal plane in the axial slice is enhanced by recording images after rotating the crystal about the active -1010 reflection vector enabling a broader projection of the basal plane. Ray tracing simulation results of the contrast from deflected TMDs in synchrontron monochromatic beam x-ray topography (SMBXT) images of 11-28 grazing incidence reflection reveal that the two partial dislocations associated with stacking faults have Burgers vectors which exhibit the same sign in their c-components.

(6) Stacking faults in a configuration shaped like a six-pointed star comprise faults have been studied. The star is determined to be composed of Shockley faults with three different fault vectors of 1/3<-1100> type. The outline of the star is confined by 30° Shockley partial dislocations lying along <11-20 > directions and a micropipe is located in the center of the star stacking fault. It is postulated that the micropipe can be the source of 60° dislocations of 1/3<-2110> Burgers vector on basal plane and pure screw dislocations of 1/3<11-20 > Burgers vector on prismatic plane. The screw dislocations can cross slip from prismatic plane to basal plane. Then, two partials of a screw dislocation start to separate under stress because one partial is sessile and the other one glissile due to mutual influence of force from dislocations generated in two different slip systems. Shockley faults form and expand as a result of glide of the glissile partials. The six-point star stacking faults appear when the glide of Shockley partials occurs in all six slip directions that are perpendicular to the dislocation line direction.

(7) Stacking faults possessing limited numbers of bilayers of 6H polytype structure have been studied. Ray tracing simulation results of the contrast from the two partial dislocations associated with the stacking faults in SMBXT images reveal the opposite sign nature of their Burgers vectors. A mechanism for stacking fault formation via 2D nucleation is postulated, in which macrosteps that directly cause the deflection of threading dislocations with c-component of Burgers vector play a key role as on the one hand their slow speed of advance provides a time interval for the 2D nucleation and on the other hand their tendency to maintain the integrity of the stacking sequence impedes the stacking faults from developing into full blown polytype inclusions of greater thickness.

(8) V shaped defects in the homoepitaxial layers have been studies. These faint needle-like surface morphological defects are comprised of one or more overlapping Frank faults which can be generated by repetitive 2D nucleation of a single SiC bilayer of wrong stacking sequence at different atomic layers during epitaxial growth. So far, three faulted stacking sequences, namely (85), (50) and (63), are observed to be associated with V shaped defects. An operation to eliminate one SiC bilayer can transform the lattice from the perfect stacking sequence to the (50) stacking sequence, which introduces a distortion of ¼c[0001] to the lattice. Such operation repeats three times at different atomic layers can transform the lattice from the perfect stacking

sequence to the (85) or (63) stacking sequence, which introduces a distortion of ¾c[0001] to the lattice.

(9) A new method has been developed to determine the fault vectors associated with stacking faults from their stacking sequences observed on HRTEM images. This method, analogous to the Burgers circuit technique for determination of dislocation Burgers vector, involves determination of the vectors required in the projection of the perfect lattice to correct the deviated path constructed in the faulted material. This technique is expected to be applicable to all structures comprising corner shared tetrahedra, such as 2H, 3C, 4H, 6H, and 15R.

(10) An amended technique of correcting the deviated path for a stacking fault has been developed to find the most efficient way to transform the perfect stacking sequence to the faulted stacking sequence. It also can be utilized to find all the other possible solutions to do the transformation using operation like eliminating one or several bilayers or shifting stacking positions on the (0001) basal plane. This technique is also expected to be applicable to all structures comprising corner shared tetrahedra.

References

1. Kimoto, T. and J.A. Cooper, *Fundamentals of silicon carbide technology : growth, characterization, devices and applications*. pages cm.
2. Trew, R.J., *Wide Bandgap Semiconductor Transistors for Microwave Power Amplifiers.* Ieee Microwave Magazine, 2000. **1**(1): p. 46-54.
3. Neudeck, P.G., R.S. Okojie, and L.Y. Chen, *High-temperature electronics - A role for wide bandgap semiconductors?* Proceedings of the Ieee, 2002. **90**(6): p. 1065-1076.
4. Schaffer, W.J., et al., *Conductivity Anisotropy in Epitaxial 6h and 4h Sic.* Diamond, Sic and Nitride Wide Bandgap Semiconductors, 1994. **339**: p. 595-600.
5. Nelson, W.E., F.A. Halden, and Rosengre.A, *Growth and Properties of Beta-Sic Single Crystals.* Journal of Applied Physics, 1966. **37**(1): p. 333-&.
6. *Electrical properties of silicon, http://www.ioffe.rssi.ru/SVA/NSM/Semicond/Si/electric.html.*
7. Bhatnagar, M. and B.J. Baliga, *Comparison of 6h-Sic, 3c-Sic, and Si for Power Devices.* Ieee Transactions on Electron Devices, 1993. **40**(3): p. 645-655.
8. *Saturation velocity, http://en.wikipedia.org/wiki/Saturation_velocity.*
9. *Silicon carbide, http://en.wikipedia.org/wiki/Silicon_carbide.*
10. *Silicon, http://en.wikipedia.org/wiki/Silicon.*
11. *Gallium arsenide, http://en.wikipedia.org/wiki/Gallium_arsenide.*
12. Casady, J.B. and R.W. Johnson, *Status of silicon carbide (SiC) as a wide-bandgap semiconductor for high-temperature applications: A review.* Solid-State Electronics, 1996. **39**(10): p. 1409-1422.
13. Tairov, Y.M. and V.F. Tsvetkov, *General-Principles of Growing Large-Size Single-Crystals of Various Silicon-Carbide Polytypes.* Journal of Crystal Growth, 1981. **52**(Apr): p. 146-150.
14. Leonard, R.T., et al., *100 mm 4HN-SiC Wafers with Zero Micropipe Density.* Silicon Carbide and Related Materials 2007, Pts 1 and 2, 2009. **600-603**: p. 7-10.
15. Muller, G.S., et al., *Volume production of high quality SiC substrates and epitaxial layers: Defect trends and device applications.* Journal of Crystal Growth, 2012. **352**(1): p. 39-42.
16. Zorman, C.A., et al., *Epitaxial-Growth of 3c-Sic Films on 4 Inch Diam (100)Silicon-Wafers by Atmospheric-Pressure Chemical-Vapor-Deposition.* Journal of Applied Physics, 1995. **78**(8): p. 5136-5138.
17. Kimoto, T., et al., *Growth-Mechanism of 6h-Sic in Step-Controlled Epitaxy.* Journal of Applied Physics, 1993. **73**(2): p. 726-732.
18. Davis, R.F., et al., *Epitaxial-Growth, Doping and Analytical Characterization of Monocrystalline Beta-Sic Semiconductor Thin-Films.* Journal of Electronic Materials, 1987. **16**(4): p. A23-A23.
19. *Cree MATCATALOG_SiC Data Sheets, 2013.*
20. Neudeck, P.G. and J.A. Powell, *Performance Limiting Micropipe Defects in Silicon-Carbide Wafers.* Ieee Electron Device Letters, 1994. **15**(2): p. 63-65.
21. Neudeck, P.G., W. Huang, and M. Dudley, *Breakdown degradation associated with elementary screw dislocations in 4H-SiC p(+)n junction rectifiers.* Solid-State Electronics, 1998. **42**(12): p. 2157-2164.
22. Skowronski, M. and S. Ha, *Degradation of hexagonal silicon-carbide-based bipolar devices.* Journal of Applied Physics, 2006. **99**(1).
23. Pirouz, P., et al., *Nitrogen doping and multiplicity of stacking faults in SiC.* Philosophical Magazine, 2006. **86**(29-31): p. 4685-4697.
24. Okojie, R.S., et al., *Observation of 4H-SiC to 3C-SiC polytypic transformation during oxidation.* Applied Physics Letters, 2001. **79**(19): p. 3056-3058.
25. Okojie, R.S., et al., *4H-to 3C-SiC polytypic transformation during oxidation.* Silicon Carbide and Related Materials 2001, Pts 1 and 2, Proceedings, 2002. **389-3**: p. 451-454.

26. Fujiwara, H., et al., *Characterization of in-grown stacking faults in 4H-SiC (0001) epitaxial layers and its impacts on high-voltage Schottky barrier diodes.* Applied Physics Letters, 2005. **87**(5).
27. Lee, K.Y. and M.A. Capan, *The correlation of surface defects and reverse breakdown of 4H-SiC Schottky barrier diodes.* Journal of Electronic Materials, 2007. **36**(4): p. 272-276.
28. Kimoto, T., N. Miyamoto, and H. Matsunami, *Performance limiting surface defects in SiC epitaxial p-n junction diodes.* Ieee Transactions on Electron Devices, 1999. **46**(3): p. 471-477.
29. Si, W.M., et al., *Hollow-core screw dislocations in 6H-SiC single crystals: A test of Frank's theory.* Journal of Electronic Materials, 1997. **26**(3): p. 128-133.
30. Giocondi, J., et al., *An atomic force microscopy study of super-dislocation/micropipe complexes on the 6H-SiC(0001) growth surface.* Journal of Crystal Growth, 1997. **181**(4): p. 351-362.
31. Dudley, M., et al., *White-Beam Synchrotron Topographic Studies of Defects in 6h-Sic Single-Crystals.* Journal of Physics D-Applied Physics, 1995. **28**(4A): p. A63-A68.
32. Huang, X.R., et al., *Direct evidence of micropipe-related pure superscrew dislocations in SiC.* Applied Physics Letters, 1999. **74**(3): p. 353-355.
33. Si, W., et al., *Experimental studies of hollow-core screw dislocations in 6H-SiC and 4H-SiC single crystals.* Silicon Carbide, Iii-Nitrides and Related Materials, Pts 1 and 2, 1998. **264-2**: p. 429-432.
34. Frank, F.C., *Capillary Equilibria of Dislocated Crystals.* Acta Crystallographica, 1951. **4**(6): p. 497-501.
35. Dudley, M., et al., *The mechanism of micropipe nucleation at inclusions in silicon carbide.* Applied Physics Letters, 1999. **75**(6): p. 784-786.
36. Wu, F.Z., et al., *Synchrotron X-ray Topography Studies of the Propagation and Post-Growth Mutual Interaction of Threading Growth Dislocations with c-component of Burgers Vector in PVT-Grown 4H-SiC.* Silicon Carbide and Related Materials 2011, Pts 1 and 2, 2012. **717-720**: p. 343-346.
37. Ha, S., et al., *Plastic deformation and residual stresses in SiC boules grown by PVT.* Silicon Carbide and Related Materials - 1999 Pts, 1 & 2, 2000. **338-3**: p. 67-70.
38. Hong, M.H., A.V. Samant, and P. Pirouz, *Stacking fault energy of 6H-SiC and 4H-SiC single crystals.* Philosophical Magazine a-Physics of Condensed Matter Structure Defects and Mechanical Properties, 2000. **80**(4): p. 919-935.
39. Pirouz, P., J.L. Demenet, and M.H. Hong, *On transition temperatures in the plasticity and fracture of semiconductors.* Philosophical Magazine a-Physics of Condensed Matter Structure Defects and Mechanical Properties, 2001. **81**(5): p. 1207-1227.
40. Persson, P.O.A., et al., *Structural defects in electrically degraded 4H-SiC p(+)/n(-)/n(+) diodes.* Applied Physics Letters, 2002. **80**(25): p. 4852-4854.
41. Skowronski, M., et al., *Recombination-enhanced defect motion in forward-biased 4H-SiC p-n diodes.* Journal of Applied Physics, 2002. **92**(8): p. 4699-4704.
42. Galeckas, A., J. Linnros, and P. Pirouz, *Recombination-enhanced extension of stacking faults in 4H-SiC p-i-n diodes under forward bias.* Applied Physics Letters, 2002. **81**(5): p. 883-885.
43. Bergman, J.P., et al., *Crystal defects as source of anomalous forward voltage increase of 4H-SiC diodes.* Silicon Carbide and Related Materials, Ecscrm2000, 2001. **353-356**: p. 299-302.
44. Liu, J.Q., et al., *Structure of recombination-induced stacking faults in high-voltage SiC p-n junctions.* Applied Physics Letters, 2002. **80**(5): p. 749-751.
45. Ha, S., et al., *Dislocation conversion in 4H silicon carbide epitaxy.* Journal of Crystal Growth, 2002. **244**(3-4): p. 257-266.
46. Hull, D. and D.J. Bacon, *Introduction to dislocations*. 4th ed. 2001, Oxford Oxfordshire ; Boston: Butterworth-Heinemann. vii, 242 p.
47. Tsuchida, A., et al., *Investigation of basal plane dislocations in the 4H-SiC epilayers grown on {0001} substrates.* Silicon Carbide and Related Materials 2004, 2005. **483**: p. 97-100.

48. Zhang, Z. and T.S. Sudarshan, *Basal plane dislocation-free epitaxy of silicon carbide.* Applied Physics Letters, 2005. **87**(15).
49. Zhang, Z., E. Moulton, and T.S. Sudarshan, *Mechanism of eliminating basal plane dislocations in SiC thin films by epitaxy on an etched substrate.* Applied Physics Letters, 2006. **89**(8).
50. Stahlbush, R.E., et al., *Basal plane dislocation reduction in 4H-SiC epitaxy by growth interruptions.* Applied Physics Letters, 2009. **94**(4).
51. VanMil, B.L., et al., *Basal plane dislocation reduction for 8 degrees off-cut, 4H-SiC using in situ variable temperature growth interruptions.* Journal of Vacuum Science & Technology B, 2008. **26**(4): p. 1504-1507.
52. Tsuchida, H., et al., *Fast Epitaxial Growth of 4H-SiC and Analysis of Defect Transfer.* Silicon Carbide and Related Materials 2008, 2009. **615-617**: p. 67-72.
53. Zhang, X., et al., *Glide and multiplication of basal plane dislocations during 4H-SiC homoepitaxy.* Journal of Applied Physics, 2007. **102**(9).
54. Zhang, N., et al., *Nucleation mechanism of dislocation half-loop arrays in 4H-silicon carbide homoepitaxial layers.* Applied Physics Letters, 2009. **94**(12).
55. Jacobson, H., et al., *Doping-induced strain in N-doped 4H-SiC crystals.* Applied Physics Letters, 2003. **82**(21): p. 3689-3691.
56. Zhang, X., T. Miyazawa, and H. Tsuchida, *Critical Conditions of Misfit Dislocation Formation in 4H-SiC Epilayers.* Silicon Carbide and Related Materials 2011, Pts 1 and 2, 2012. **717-720**: p. 313-318.
57. Skromme, B.J., et al., *Oxidation-induced crystallographic transformation in heavily N-doped 4H-SiC wafers.* Silicon Carbide and Related Materials 2001, Pts 1 and 2, Proceedings, 2002. **389-3**: p. 455-458.
58. Liu, J.Q., et al., *Structural instability of 4H-SiC polytype induced by n-type doping.* Applied Physics Letters, 2002. **80**(12): p. 2111-2113.
59. Miao, M.S., S. Limpijumnong, and W.R.L. Lambrecht, *Stacking fault band structure in 4H-SiC and its impact on electronic devices.* Applied Physics Letters, 2001. **79**(26): p. 4360-4362.
60. Hirth, J.P. and J. Lothe, *Theory of dislocations*. 2nd ed. 1982, New York: Wiley. xii, 857 p.
61. Izumi, S., et al., *Structural analysis and reduction of in-grown stacking faults in 4H-SiC epilayers.* Applied Physics Letters, 2005. **86**(20).
62. Feng, G., J. Suda, and T. Kimoto, *Triple Shockley type stacking faults in 4H-SiC epilayers.* Applied Physics Letters, 2009. **94**(9).
63. Abadier, M., et al., *Nucleation of in-grown stacking faults and dislocation half-loops in 4H-SiC epitaxy.* Journal of Applied Physics, 2013. **114**(12).
64. Tsuchida, H., I. Kamata, and M. Nagano, *Formation of basal plane Frank-type faults in 4H-SiC epitaxial growth.* Journal of Crystal Growth, 2008. **310**(4): p. 757-765.
65. Benamara, M., et al., *Structure of the carrot defect in 4H-SiC epitaxial layers.* Applied Physics Letters, 2005. **86**(2).
66. Zhang, X., et al., *Cross-sectional structure of carrot defects in 4H-SiC epilayers.* Applied Physics Letters, 2004. **85**(22): p. 5209-5211.
67. Powell, J.A. and D.J. Larkin, *Process-induced morphological defects in epitaxial CVD silicon carbide.* Physica Status Solidi B-Basic Research, 1997. **202**(1): p. 529-548.
68. Si, W.M., et al., *Investigations of 3C-SiC inclusions in 4H-SiC epilayers on 4H-SiC single crystal substrates.* Journal of Electronic Materials, 1997. **26**(3): p. 151-159.
69. Kimoto, T., A. Itoh, and H. Matsunami, *Step-controlled epitaxial growth of high-quality SiC layers.* Physica Status Solidi B-Basic Solid State Physics, 1997. **202**(1): p. 247-262.
70. Knippenberg, W.F., *Growth Phenomena in Silicon Carbide.* Philips research reports, 1963. **18**: p. 161.

71. Heine, V., C. Cheng, and R.J. Needs, *The Preference of Silicon-Carbide for Growth in the Metastable Cubic Form.* Journal of the American Ceramic Society, 1991. **74**(10): p. 2630-2633.
72. Kotamraju, S., et al., *Low-temperature homoepitaxial growth of 4H-SiC with CH3Cl and SiCl4 precursors.* Journal of Crystal Growth, 2010. **312**(5): p. 645-650.
73. Beaumont, J.H. and M. Hart, *Multiple Bragg Reflection Monochromators for Synchrotron-X Radiation.* Journal of Physics E-Scientific Instruments, 1974. **7**(10): p. 823-829.
74. Cullity, B.D., *Elements of x-ray diffraction*. 2d ed. Addison-Wesley series in metallurgy and materials. 1978, Reading, Mass.: Addison-Wesley Pub. Co. xii, 555 p.
75. Dudley, M., J. Wu, and G.D. Yao, *Determination of Penetration Depths and Analysis of Strains in Single-Crystals by White Beam Synchrotron X-Ray Topography in Grazing Bragg-Laue Geometries.* Nuclear Instruments & Methods in Physics Research Section B-Beam Interactions with Materials and Atoms, 1989. **40-1**: p. 388-392.
76. Tanner, B.K., *X-ray diffraction topography*. 1st ed. International series in the science of the solid state v 10. 1976, New York: Pergamon Press. xiii, 174 p.
77. Williams, D.B. and C.B. Carter, *Transmission electron microscopy : a textbook for materials science*. 2nd ed. 2008, New York: Springer.
78. Zhuang, D. and J.H. Edgar, *Wet etching of GaN, AIN, and SiC: a review.* Materials Science & Engineering R-Reports, 2005. **48**(1): p. 1-46.
79. Vetter, W.M. and M. Dudley, *The character of micropipes in silicon carbide crystals.* Philosophical Magazine, 2006. **86**(9): p. 1209-1225.
80. Neudeck, P.G., *Electrical impact of SiC structural crystal defects on high electric field devices.* Silicon Carbide and Related Materials - 1999 Pts, 1 & 2, 2000. **338-3**: p. 1161-1166.
81. Lendenmann, H., et al., *Long term operation of 4.5kV PiN and 2.5kV JBS diodes.* Silicon Carbide and Related Materials, Ecscrm2000, 2001. **353-356**: p. 727-730.
82. Dudley, M., et al., *Stacking faults created by the combined deflection of threading dislocations of Burgers vector c and c plus a during the physical vapor transport growth of 4H-SiC.* Applied Physics Letters, 2011. **98**(23).
83. Dudley, M., et al., *Formation Mechanism of Stacking Faults in PVT 4H-SiC Created by Deflection of Threading Dislocations with Burgers Vector c plus a.* Silicon Carbide and Related Materials 2010, 2011. **679-680**: p. 269-272.
84. Dudley, M., et al., *Analysis of Dislocation Behavior in Low Dislocation Density, PVT-Grown, Four-Inch Silicon Carbide Single Crystals.* B - Silicon Carbide 2010-Materials, Processing and Devices, 2010. **1246**.
85. Chen, Y., et al., *Simulation of grazing-incidence synchrotron white beam X-ray topographic images of micropipes in 4H-SiC and determination of their dislocation senses.* Journal of Electronic Materials, 2008. **37**(5): p. 713-720.
86. Kamata, I., et al., *High-Resolution Topography Analysis on Threading Edge Dislocations in 4H-SiC Epilayers.* Silicon Carbide and Related Materials 2007, Pts 1 and 2, 2009. **600-603**: p. 305-308.
87. Huang, X.R., et al., *High-geometrical-resolution imaging of dislocations in SiC using monochromatic synchrotron topography.* Applied Physics Letters, 2007. **91**(23).
88. Dudley, M., X.R. Huang, and W. Huang, *Assessment of orientation and extinction contrast contributions to the direct dislocation image.* Journal of Physics D-Applied Physics, 1999. **32**(10A): p. A139-A144.
89. Bowen, D.K. and B.K. Tanner, *High resolution X-ray diffractometry and topography*. 1998, London ; Bristol, PA: Taylor & Francis. x, 252 p.
90. Eshelby, J.D. and A.N. Stroh, *Dislocations in Thin Plates.* Philosophical Magazine, 1951. **42**(335): p. 1401-1405.

91. Chen, H., et al., *The formation mechanism of carrot defects in SiC epifilms.* Silicon Carbide 2006 - Materials, Processing and Devices, 2006. **911**: p. 163-168.
92. Authier, A. and Y. Epelboin, *Variation of Stacking-Fault Contrast with Value of Phase-Shift in X-Ray Topography.* Physica Status Solidi a-Applied Research, 1977. **41**(1): p. K9-&.
93. Pirouz, P. and J.W. Yang, *Polytypic Transformations in Sic - the Role of Tem.* Ultramicroscopy, 1993. **51**(1-4): p. 189-214.
94. Dudley, M., X.R. Huang, and W.M. Vetter, *Contribution of x-ray topography and high-resolution diffraction to the study of defects in SiC.* Journal of Physics D-Applied Physics, 2003. **36**(10A): p. A30-A36.
95. Ha, S., et al., *Identification of prismatic slip bands in 4H SiC boules grown by physical vapor transport.* Journal of Electronic Materials, 2000. **29**(7): p. L5-L8.
96. Wang, H., et al., *Basal Plane Dislocation Multiplication via the Hopping Frank-Read Source Mechanism and Observations of Prismatic Glide in 4H-SiC.* Silicon Carbide and Related Materials 2011, Pts 1 and 2, 2012. **717-720**: p. 327-330.
97. Mussi, A., J.L. Demenet, and J. Rabier, *TEM study of defects generated in 4H-SiC by microindentations on the prismatic plane.* Philosophical Magazine Letters, 2006. **86**(9): p. 561-568.
98. Muller, S.G., et al., *The status of SiC bulk growth from an industrial point of view.* Journal of Crystal Growth, 2000. **211**(1-4): p. 325-332.
99. Kanaya, M., et al., *Controlled Sublimation Growth of Single Crystalline 4h-Sic and 6h-Sic and Identification of Polytypes by X-Ray-Diffraction.* Applied Physics Letters, 1991. **58**(1): p. 56-58.
100. Yakimova, R., et al., *Polytype stability in seeded sublimation growth of 4H-SiC boules.* Journal of Crystal Growth, 2000. **217**(3): p. 255-262.
101. Tupitsyn, E.Y., et al., *Controllable 6H-SiC to 4H-SiC polytype transformation during PVT growth.* Journal of Crystal Growth, 2007. **299**(1): p. 70-76.
102. Sugiyama, N., et al., *Step structures and dislocations of SiC single crystals grown by modified Lely method.* Journal of Crystal Growth, 1998. **191**(1-2): p. 84-91.
103. Leone, S., et al., *Improved morphology for epitaxial growth on 4 degrees off-axis 4H-SiC substrates.* Journal of Crystal Growth, 2009. **311**(12): p. 3265-3272.
104. Konstantinov, A.O., et al., *Fast generation recombination channels due to epitaxial defects in SiC metal-oxide-semiconductor devices.* Silicon Carbide, Iii-Nitrides and Related Materials, Pts 1 and 2, 1998. **264-2**: p. 1025-1028.
105. Syvajarvi, M., et al., *Polytype inclusions and triangular stacking faults in 4H-SiC layers grown by sublimation epitaxy.* Physica Scripta, 1999. **T79**: p. 64-66.
106. Yazdanfar, M., et al., *Carrot defect control in chloride-based CVD through optimized ramp up conditions.* Silicon Carbide and Related Materials 2011, Pts 1 and 2, 2012. **717-720**: p. 109-112.
107. Wang, H., et al., *Synchrotron topography studies of the operation of double-ended Frank-Read partial dislocation sources in 4H-SiC.* Journal of Crystal Growth, 2014. **401**: p. 423-430.
108. Wu, F.Z., et al., *Characterization and Formation Mechanism of Six Pointed Star-Type Stacking Faults in 4H-SiC.* Journal of Electronic Materials, 2013. **42**(5): p. 787-793.

Appendix I -- Mathematica® code of (2-1-18) simulation of threading c+60 °a dislocation

```
(*unit um*)
magnification = 10;
b = 0.001005;
t = 200;
d = 150000;
b1 = 0.000308;
v = 0.18;
α = 60 °;(*b1 to 11-20 angle*)
θ0 = 4 °;(*off-axis angle*)
(*incident beam*)
ρ = 2 ° + ArcTan[Tan[4 °] * Cos[60 °]];
rx = -Cos[ρ] * Cos[-60 °];
ry = -Cos[ρ] * Sin[-60 °];
rz = -Sin[ρ];
nx00 = Cos[50.79 °];
ny00 = 0;
nz00 = Sin[50.79 °];
nx0 = Cos[60 °] * nx00 + Sin[60 °] ny00;(*surface normal of reflective plane*)
ny0 = Cos[60 °] * ny00 - Sin[60 °] nx00;
nz0 = nz00;
rxC = (-nx0^2 rx + ny0^2 rx + nz0^2 rx - 2 nx0 ny0 ry - 2 nx0 nz0 rz) / (nx0^2 + ny0^2 + nz0^2);
(*reflective beam from perfect plane*)
ryC = (-2 nx0 ny0 rx + nx0^2 ry - ny0^2 ry + nz0^2 ry - 2 ny0 nz0 rz) / (nx0^2 + ny0^2 + nz0^2);
rzC = (-2 nx0 nz0 rx - 2 ny0 nz0 ry + nx0^2 rz + ny0^2 rz - nz0^2 rz) / (nx0^2 + ny0^2 + nz0^2);
x1C = (rzC * 0 - rxC * 0 + d rxC Cos[θ0] + d rzC Sin[θ0]) / (rzC Cos[θ0] - rxC Sin[θ0]);(*the film center*)
y1C = (d ryC + rzC * 0 * Cos[θ0] - ryC * 0 * Cos[θ0] + ryC * 0 * Sin[θ0] - rxC * 0 * Sin[θ0]) /
    (rzC Cos[θ0] - rxC Sin[θ0]);
uxTED = 1/(8 π (-1 + v) (x0^2 + y0^2)) b1
    (-2 x0 y0 Cos[α] + 4 (-1 + v) (x0^2 + y0^2) ArcTan[(y0 Cos[α] - x0 Sin[α])/(x0 Cos[α] + y0 Sin[α])] Cos[α] +
      (x0^2 - y0^2 + (-1 + 2 v) (x0^2 + y0^2) Log[x0^2 + y0^2]) Sin[α]);
uyTED = 1/(8 π (-1 + v) (x0^2 + y0^2)) b1 (Cos[α] (x0^2 - y0^2 - (-1 + 2 v) (x0^2 + y0^2) Log[x0^2 + y0^2]) +
      2 x0 y0 Sin[α] + 4 (-1 + v) (x0^2 + y0^2) ArcTan[(y0 Cos[α] - x0 Sin[α])/(x0 Cos[α] + y0 Sin[α])] Sin[α]);
uθ = (-b/(2 Pi)) * Sum[(-1)^n * ((Sqrt[x0^2 + y0^2] /
          ((2 n + 1) * t - (z0 + t)) + Sqrt[((2 n + 1) * t - (z0 + t))^2 + (x0^2 + y0^2)])) -
        (Sqrt[x0^2 + y0^2] / ((2 n + 1) * t + (z0 + t) +
            Sqrt[((2 n + 1) * t + (z0 + t))^2 + (x0^2 + y0^2)]))), {n, 0, 3}];
ux[x0_, y0_, z0_] = uθ * (-y0) / Sqrt[x0^2 + y0^2] + uxTED;
uy[x0_, y0_, z0_] = uθ * x0 / Sqrt[x0^2 + y0^2] + uyTED;
uxDX = D[ux[x0, y0, z0], x0];
uxDY = D[ux[x0, y0, z0], y0];
uxDZ = D[ux[x0, y0, z0], z0];
```

```
uyDX = D[uy[x0, y0, z0], x0];
uyDY = D[uy[x0, y0, z0], y0];
uyDZ = D[uy[x0, y0, z0], z0];
filmDensity = Table[0, {i, 1, 500}, {j, 1, 500}];
Do[
 If[x0 == 0 && y0 == 0, Continue[]];
 z0 = Tan[θ0] * x0;
 uzDx = -(b y0)/(2 π x0^2 + 2 π y0^2);
 uzDy = (b x0)/(2 π x0^2 + 2 π y0^2);
 uzDz = 0;
 uxDx = uxDX;
 uxDy = uxDY;
 uxDz = uxDZ;
 uyDx = uyDX;
 uyDy = uyDY;
 uyDz = uyDZ;
 nx = nx0 - nx0 * uxDx - ny0 * uyDx - nz0 * uzDx;
 ny = ny0 - nx0 * uxDy - ny0 * uyDy - nz0 * uzDy;
 nz = nz0 - nx0 * uxDz - ny0 * uyDz - nz0 * uzDz;
 rx1 = (-nx^2 rx + ny^2 rx + nz^2 rx - 2 nx ny ry - 2 nx nz rz)/(nx^2 + ny^2 + nz^2);
 ry1 = (-2 nx ny rx + nx^2 ry - ny^2 ry + nz^2 ry - 2 ny nz rz)/(nx^2 + ny^2 + nz^2);
 rz1 = (-2 nx nz rx - 2 ny nz ry + nx^2 rz + ny^2 rz - nz^2 rz)/(nx^2 + ny^2 + nz^2);
 x1 = ((rz1 x0 - rx1 z0 + d rx1 Cos[θ0] + d rz1 Sin[θ0])/(rz1 Cos[θ0] - rx1 Sin[θ0]) - x1C) * magnification;
 y1 = (((d ry1 + rz1 y0 Cos[θ0] - ry1 z0 Cos[θ0] + ry1 x0 Sin[θ0] - rx1 y0 Sin[θ0]) /
       (rz1 Cos[θ0] - rx1 Sin[θ0]) - y1C) * magnification;
 If[Floor[x1] ≥ -250 && Floor[x1] < 250 && Floor[y1] ≥ -250 && Floor[y1] < 250,
  filmDensity = ReplacePart[filmDensity, {Floor[x1] + 251, Floor[y1] + 251} →
      Extract[filmDensity, {Floor[x1] + 251, Floor[y1] + 251}] + 1]],
 {x0, -25, 25, 0.025}, {y0, -25, 25, 0.025}]
ColorNegate[ListDensityPlot[filmDensity, Mesh → None, ImageSize → Large]]
```

Appendix II -- Mathematica® code of (11-28) simulation of deflected c+60 °a dislocation

```
(*unit um*)
magnification = 10;
c = 0.001005;
b0 = 0.000308;
t = 200;
d = 150000;
v = 0.18;
α = 60 °;(*b0 to line angle*)
θ0 = 4 °;(*off-axis angle*)
θ = 9.58 ° - θ0;
rx = -Cos[(2 ° + θ0)];
ry = 0;
rz = -Sin[(2 ° + θ0)];
nx0 = Cos[50.79 °];
ny0 = 0;
nz0 = Sin[50.79 °];
rxC = (-nx0^2 rx + ny0^2 rx + nz0^2 rx - 2 nx0 ny0 ry - 2 nx0 nz0 rz)/(nx0^2 + ny0^2 + nz0^2);
(*reflective beam from perfect plane*)
ryC = (-2 nx0 ny0 rx + nx0^2 ry - ny0^2 ry + nz0^2 ry - 2 ny0 nz0 rz)/(nx0^2 + ny0^2 + nz0^2);
rzC = (-2 nx0 nz0 rx - 2 ny0 nz0 ry + nx0^2 rz + ny0^2 rz - nz0^2 rz)/(nx0^2 + ny0^2 + nz0^2);
x1C = (rzC * 0 - rxC * 0 + d rxC Cos[θ0] + d rzC Sin[θ0])/(rzC Cos[θ0] - rxC Sin[θ0]) (*the film center*)
y1C = (d ryC + rzC * 0 * Cos[θ0] - ryC * 0 * Cos[θ0] + ryC * 0 * Sin[θ0] - rxC * 0 * Sin[θ0])/(rzC Cos[θ0] - rxC Sin[θ0])
ux[x0_, y0_, z0_] = (b0 ArcTan[z0/y0] Cos[α])/(2 π);
uy[x0_, y0_, z0_] =
 (c ((-y0^2+z0^2)/(y0^2+z0^2) + (1 - 2 v) Log[y0^2 + z0^2]))/(8 π (1 - v)) + (b0 ((y0 z0)/(2 (1-v) (y0^2+z0^2)) + ArcTan[z0/y0]) Sin[α])/(2 π);
uz[x0_, y0_, z0_] = (c (-(y0 z0)/(2 (1-v) (y0^2+z0^2)) - ArcTan[y0/z0]))/(2 π) -
 (b0 ((y0^2-z0^2)/(y0^2+z0^2) + (1 - 2 v) Log[y0^2 + z0^2]) Sin[α])/(8 π (1 - v));
uxDX = D[ux[x0, y0, z0], x0] // Simplify
uxDY = D[ux[x0, y0, z0], y0] // Simplify
uxDZ = D[ux[x0, y0, z0], z0] // Simplify
uyDX = D[uy[x0, y0, z0], x0] // Simplify
uyDY = D[uy[x0, y0, z0], y0] // Simplify
uyDZ = D[uy[x0, y0, z0], z0] // Simplify
uzDX = D[uz[x0, y0, z0], x0] // Simplify
uzDY = D[uz[x0, y0, z0], y0] // Simplify
uzDZ = D[uz[x0, y0, z0], z0] // Simplify
```

```
filmDensity = Table[0, {i, 1, 500}, {j, 1, 500}];
Do[
 z0 = Tan[θ0] * x0 + Tan[θ0] * 25 - z;
 If[y0 == 0 && z0 == 0, Continue[]];
 uxDx = uxDX;
 uxDy = uxDY;
 uxDz = uxDZ;
 uyDx = uyDX;
 uyDy = uyDY;
 uyDz = uyDZ;
 uzDx = uzDX;
 uzDy = uzDY;
 uzDz = uzDZ;
 nx = nx0 - nx0 * uxDx - ny0 * uyDx - nz0 * uzDx;
 ny = ny0 - nx0 * uxDy - ny0 * uyDy - nz0 * uzDy;
 nz = nz0 - nx0 * uxDz - ny0 * uyDz - nz0 * uzDz;
 rx1 = (-nx^2 rx + ny^2 rx + nz^2 rx - 2 nx ny ry - 2 nx nz rz) / (nx^2 + ny^2 + nz^2);
 ry1 = (-2 nx ny rx + nx^2 ry - ny^2 ry + nz^2 ry - 2 ny nz rz) / (nx^2 + ny^2 + nz^2);
 rz1 = (-2 nx nz rx - 2 ny nz ry + nx^2 rz + ny^2 rz - nz^2 rz) / (nx^2 + ny^2 + nz^2);
 x1 = ((rz1 x0 - rx1 z0 + d rx1 Cos[θ0] + d rz1 Sin[θ0]) / (rz1 Cos[θ0] - rx1 Sin[θ0]) - x1C) * magnification;
 y1 = ((d ry1 + rz1 y0 Cos[θ0] - ry1 z0 Cos[θ0] + ry1 x0 Sin[θ0] - rx1 y0 Sin[θ0]) / (rz1 Cos[θ0] - rx1 Sin[θ0]) - y1C) *
   magnification;
 If[Floor[x1] ≥ -250 && Floor[x1] < 250 && Floor[y1] ≥ -250 && Floor[y1] < 250,
  filmDensity = ReplacePart[filmDensity, {Floor[x1] + 251, Floor[y1] + 251} →
     Extract[filmDensity, {Floor[x1] + 251, Floor[y1] + 251}] + 1]],
 {x0, -25, 25, 0.025}, {y0, -25, 25, 0.025}, {z, 0, 20, 0.05}]

ColorNegate[ListDensityPlot[filmDensity, Mesh → None, ImageSize → Large]]
```